CHALMERS UNIVERSITY OF TECHNOLOGY

TECHNISCHE UNIVERSITÄT BERLIN

Creating Active Boundary Conditions with Planar Loudspeaker Arrays to absorb and reflect sound

submitted by **ANTHEA MÜLLER**

Master's Thesis in the Programme „Physikalische Ingenieurwissenschaft M.Sc."

at TU Berlin as part of the Erasmus+ Programme

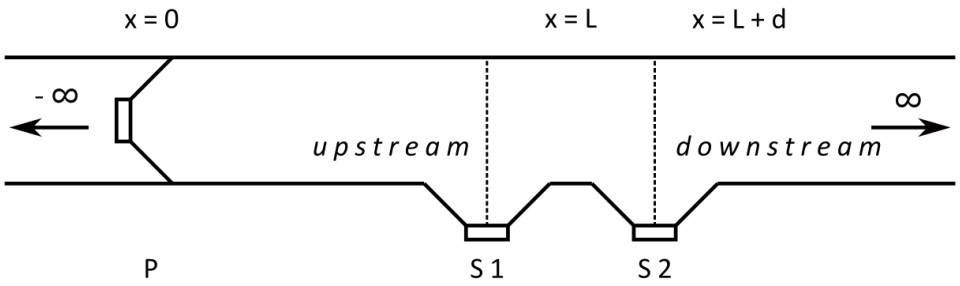

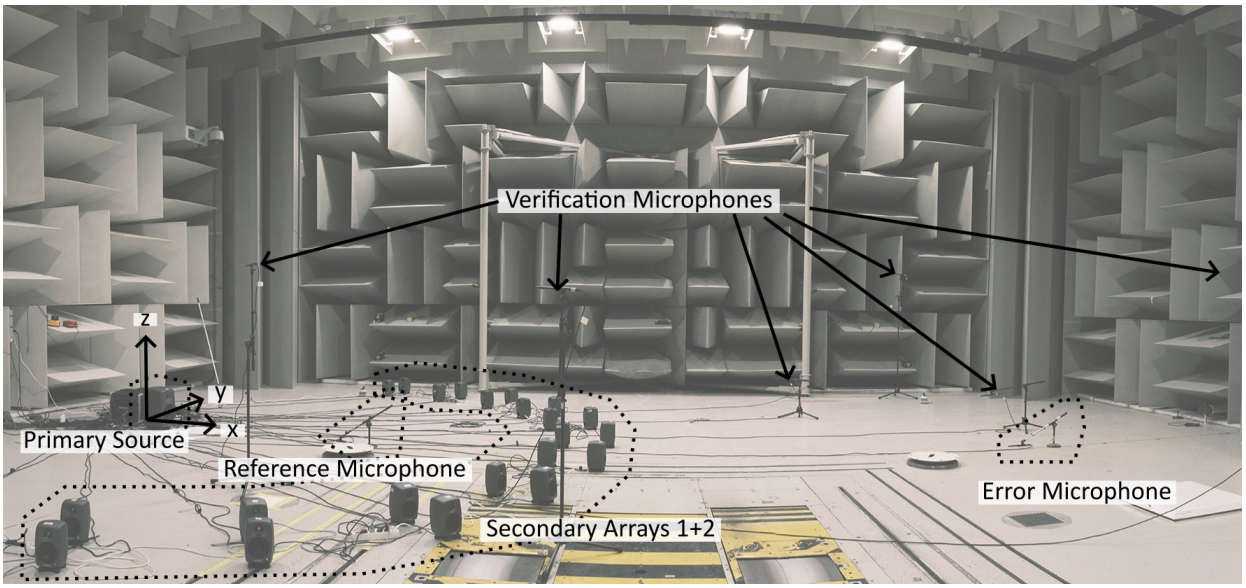

Supervisors: **Prof. Dr.-Ing. Jens Ahrens** and **Prof. Dr.-Ing. Ennes Sarradj**

Matriculation Number 394558 Berlin, October 2024

CHALMERS UNIVERSITY OF TECHNOLOGY

DIVISION OF APPLIED ACOUSTICS

Department of Architecture and Civil Engineering

TECHNISCHE UNIVERSITÄT BERLIN

FACHGEBIET TECHNISCHE AKUSTIK

Institut für Strömungsmechanik und Technische Akustik

Fakultät V—Verkehrs– und Maschinensysteme

Affidavit / Eidesstattliche Erklärung

I hereby confirm that I prepared this thesis independently and by exclusive reliance on literature and tools indicated herein. No AI programs (such as Large Language Models or Generative text-to-image Tools) have been used to write or rewrite sentences or passages of text, neither were graphs, figures, schemes or photographs created or edited with such tools.

Anthea Müller

Berlin, 29.10.2024

Date

Hiermit erkläre ich an Eides statt, dass die vorliegende Arbeit selbstständig und eigenhändig sowie ausschließlich unter Verwendung der aufgeführten Quellen und Hilfsmittel angefertigt habe. Es wurden keine KI-Programme (wie z.B. Large Language Models oder generative Text-zu-Bild-Tools) verwendet, um Sätze oder Textpassagen zu schreiben oder umzuschreiben, noch wurden Grafiken, Abbildungen, Schemata oder Fotos mit solchen Tools erstellt oder bearbeitet.

Anthea Müller

Berlin, 29.10.2024

Datum

Abstract

It was shown in the 1970s that a combination of two secondary sources are able to absorb sound energy in one-dimensional sound propagation in a duct. The primary source can be interpreted as being surrounded by a double-layer of secondary sources. This is inconvenient in two- and three-dimensional scenarios as surfaces of secondary sources have to be used, which are difficult to implement in practice. This thesis demonstrates that the same type of active absorption is possible also in open space, i.e., when the secondary sources do not fully enclose the primary source.

In contrast to active noise canceling, the aim here is not to achieve active reduction in the downstream area by increasing the sound level in the upstream area, but rather to actively remove energy from the sound field. The focus here is particularly set on canceling out low frequencies to facilite practical measurements. For this, two boundary conditions are set, one in the upstream and one in the downstream area. To achieve the objective at the boundary conditions a set of FIR filters must be determined. This is done here with the help of the LMS method, which is extended to a MIMO (Multiple Input Multiple Output) system.

First the results of Swinbanks for the active reduction inside the one dimensional duct are recreated with simulations and confirmed with an experiment. Based on these findings the approach is first extended two dimensions to perform absorption of cylindrical waves with the help of two line sources and then further extended to three dimensions to perform the absorption of spherical waves by means of one-dimensional distributions of point sources. Two experiments are carried out to confirm or refute the concepts introduced. These are first planned in detail with the help of simulations. The first experiment (Setup 1) demonstrates the active absorption of cylindrical waves emitted by line arrays in an outdoor free field setting. The second experiment (Setup 2) demonstrates the active absorption of sound emitted by a point source that is actively absorbed by curved arrays within a semi-anechoic chamber. The simulation results were confirmed in both setups with the measurement results. They proof that the active control of the downstream area whilst not influencing the upstream area is possible with the proposed boundary conditions within the limitations of the method and their test environments. In both experiments active reduction is achieved throughout the downstream area, achieving an averaged active reduction of 11 dB (3 dB over background noise level) in Setup 1 and an active averaged reduction of -27 dB (1 dB over background noise level) in Setup 2 at the boundary condition. Throughout the upstream area the average deviation from the undisturbed sound-field for Setup 1 is 0.3 dB, for Setup 2 it is 0.08 dB.

Keywords: Active Noise Control, Active Sound Absorption, Free Field Absorption, LMS Method

Zusammenfassung

In den 1970er Jahren wurde gezeigt, dass eine Kombination aus zwei Sekundärquellen in der Lage ist, Schallenergie bei eindimensionaler Schallausbreitung in einem Rohr (Duct) zu absorbieren. Die Primärquelle kann so interpretiert werden, dass sie von einer Doppelschicht von Sekundärquellen umgeben ist. Dies ist in zwei- und dreidimensionalen Szenarien ungünstig, da Oberflächen von Sekundärquellen verwendet werden müssen, die in der Praxis schwer zu realisieren sind. In dieser Arbeit wird gezeigt, dass die gleiche Art der aktiven Absorption auch unter Freifeldbedingungen möglich ist, d. h. wenn die Sekundärquellen die Primärquelle nicht vollständig umschließen.

Im Gegensatz zum aktiven Noise Cancelling geht es hier nicht darum, eine aktive Reduktion im nachgelagerten Bereich durch Erhöhung des Schallpegels im vorgelagerten Bereich zu erreichen, sondern aktiv Energie aus dem Schallfeld zu entfernen. Der Fokus liegt dabei insbesondere auf der Auslöschung tiefer Frequenzen, um praktische Messungen zu ermöglichen. Dazu werden zwei Randbedingungen gesetzt, eine im stromaufwärtigen ("upstream") und eine im stromabwärtigen ("downstream") Bereich. Um das Ziel an den Randbedingungen zu erreichen, muss ein Satz von FIR-Filtern bestimmt werden. Dies geschieht hier mit Hilfe der LMS-Methode, die auf ein MIMO-System (Multiple Input Multiple Output) erweitert wird.

Zunächst werden die Ergebnisse von Swinbanks für die aktive Reduktion im eindimensionalen Kanal mit Simulationen nachgebildet und mit einem Experiment bestätigt. Auf der Grundlage dieser Ergebnisse wird der Ansatz zunächst zweidimensional erweitert, um die Absorption zylindrischer Wellen mit Hilfe von zwei Linienquellen durchzuführen, und dann weiter auf drei Dimensionen ausgedehnt, um die Absorption sphärischer Wellen mit Hilfe eindimensional verteilter Punktquellen durchzuführen. Um die vorgestellten Konzepte zu bestätigen oder zu widerlegen, werden zwei Experimente durchgeführt. Diese werden zunächst mit Hilfe von Simulationen im Detail geplant. Das erste Experiment (Setup 1) demonstriert die aktive Absorption von Zylinderwellen, die von Line-Arrays in einem Freifeld ausgesendet werden. Das zweite Experiment (Setup 2) demonstriert die aktive Absorption von Schall, der von einer Punktquelle ausgesendet wird, die von gekrümmten Arrays in einer halbschalltoten Kammer aktiv absorbiert wird. Die Simulationsergebnisse wurden in beiden Aufbauten mit den Messergebnissen bestätigt. Sie belegen, dass die aktive Steuerung des Downstream Bereichs ohne Beeinflussung des Upstream Bereichs mit den vorgeschlagenen Randbedingungen innerhalb der Grenzen des Verfahrens und der Testumgebung möglich ist. In beiden Experimenten wird im gesamten Downstream Bereich eine aktive Reduktion erreicht, wobei in Setup 1 eine gemittelte aktive Minderung von 11 dB (3 dB über dem Hintergrundgeräuschpegel) und in Setup 2 eine gemittelte aktive Minderung von -27 dB (1 dB über dem Hintergrundgeräuschpegel) an der Randbedingung erreicht wird. Im gesamten Upstream Bereich beträgt die mittlere Abweichung vom ungestörten Schallfeld für Setup 1 0,3 dB, für Setup 2 0,08 dB.

Stichworte: Active Noise Control, Active Sound Absorption, Free Field Absorption, LMS Method

Acknowledgement

First and foremost I want to thank my supervisor and examiner Prof. Dr. Jens Ahrens from Chalmers University of Technology, who has supported me with guidance, insight and encouragement. The expertise and constructive feedback I received were invaluable in shaping my research and pushing me to refine my ideas. I would also like to thank my supervisor and examiner Prof. Dr. Ennes Sarradj from TU Berlin, as without his support and trust it would not have been possible to write this thesis abroad. Additionally I would like to thank Prof. Dr. Wolfgang Kropp from Chalmers University of Technology, who provided me with a lot of expertise and was always willing to listen to my questions and problems.

I also wish to thank Jonatan Ewald, Audio Attribute Leader from Volvo Cars, who kindly made it possible to perform one of the experiments (Setup 2) in the semi-anechoic chamber at Volvo Cars. Volvo Cars has no other substantive or formal links to this thesis and has no influence on its content, which increases my gratitude that this was made possible.

To my fellow students, especially Alex, Chenya, Laura, Theresia and Vincent, thank you for your vigorous support in carrying out my experiments, I couldn't have done it alone. Also thank you for the stimulating discussions and moral support.

A special thanks goes to my parents and other family members for their love and emotional support. Thanks also to my partner in life, who supported my decision to stay away for longer.

Finally, I would like to thank the bodies responsible for the grant as part of the Erasmus+ Mobility Program.

Acronyms

AAD Average Absolute Deviation

ANC Active Noise Control

FIR Finite Impulse Response

IR impulse response

LMS Least Mean Squares

LTI Linear and Time-Invariant

MIMO Multiple Input Multiple Output

NLMS Normalised LMS

PSD Power Spectral Density

SIMO Single Input Multiple Output

SISO Single Input Single Output

Contents

1. Introduction

Acoustic absorption plays a pivotal role in the field of acoustics, influencing a wide array of applications and environments. For applications in diffuse fields such as indoor spaces, absorption solutions are often an integral part of the architecture and are usually passive. Environmental noise pollution, a form of air pollution, is a threat to health and well-being. The potential health effects of noise pollution are "numerous, pervasive, persistent, medically and socially significant" [1, 2]. But for applications in free field conditions, the integration of passive absorption elements is often only feasible with restrictions or not at all. Especially absorbing sound waves with low frequencies at large events such as open-air concerts or festivals is an unsolved problem. Sound waves with very low frequencies can often propagate hundreds or even thousands of meters before they are attenuated enough by the air and environment. Passive absorbers several metres high, fencing off large parts of the site, would be necessary to shield residents and the environment from these sound waves. This is not feasible in practice.

An alternative solution to attenuate the sound field with passive absorbers would be to introduce a second sound field which interferes with the primary sound destructively. This second sound field would need to change according to the primary sound field, therefore making active control necessary. Before exploring further what a possible active reduction system should incorporate, a brief overview of the field of active noise control is given.

The invention of Active Noise Control (ANC) is often attributed to Paul Lueg, who first submitted his patent in Germany in 1933 [3], where it was first classified by the Nazi administration, which considered the invention to be of military relevance. After losing his position at the University of Bonn at the end of 1933 because of this patent litigation of "political nature" he endeavoured to free the patent from confidentiality. Authorities finally released the patent from classification in 1934, after which he filed patent forms in the US, France, Italy and Austria. The patent filed in the US in 1934 and approved in 1936 is usually the one which is being referred to nowadays [4]. However, applying for foreign patents was considered treason and Mr Lueg felt threatened by the Gestapo until the end of the Nazi regime in 1945 (*information about his invention, his lacking ability to demonstrate its applications and the unexpected impact on his life can be found in [5]*).

It would still take a few more years until the principles introduced in his patent would become applicable, but by now we can look back on a history of more than nine decades of ANC. In this time "the concept has progressed from simple Single Input Single Output (SISO) feedback control systems through to complex Multiple Input Multiple Output (MIMO) approaches implementing a seemingly endless variety of control algorithms" [6]. By the 1990s a variety of applications had already been explored; ranging from active control in vehicle and aircraft interiors ([7, 8]) to multichannel absorption in enclosed spaces ([9, 10]) to active noise control at construction sites [11]. In that time a lot of general instructions about the principles and how to apply different algorithms were written (like [12] or [13]) which will be referred to again throughout this thesis. The concept of ANC has stayed relevant and peaked in the last decades due to advances in microprocessers and actuator technology, resulting in the commercial successes of ANC headsets in the consumer market in the last two decades [14].

Something that all applications of ANC have in common is that sound at a certain point or in a certain area should be canceled out by interference, while it does not matter that the sound pressure increases in parts of the uncontrolled area. Coming back to the introduced example of the open air concert in the beginning, it becomes clear why this is not acceptable; nearby areas should not be polluted with sound, but within a defined area the sound of the primary source should be undisturbed. This imposes two controlled regions with two boundary conditions, one of destructive interference and one of no interference, which must be fullfiled simultaneously. To do this, the sound not only has to be "canceled" with destructive interference, energy has to be *removed* from the sound field. This concept will be referred to as "active absorption" or "active

reduction", as the term of absorption is usually used to describe passive properties and processes. However, throughout this thesis the terms will be used somewhat interchangeably.

It was first recognised by Swinbanks [15] that two secondary sources placed in a circular duct could be used to produce only downstream radiation. This combined with a primary source in the area upstream of the secondary sources creates the possibilities for active sound absorption, where energy is removed from the sound field. The analytical work of Swinbanks was later extended by works like that of Nelson and Elliot [12] where it is shown how to conceptualise filters for this SISO system in frequency domain. Active absorption has been explored to some degree in recent years, like in Norambuena's work [16] in 2012, who created a new mathematical model for a multichannel active absorption system based on the wave separation method of Nishimura inside closed rooms. However, the field of active reduction in higher dimensional, free field scenarios has not really been scientifically explored, although the concept for one-dimensional active reduction has now been known for over five decades.

This thesis will try to extend the approach of active reduction first in the one dimensional duct to higher dimensions, also based on the extensive knowledge of the closely related field of ANC. One difference in this work in comparison to many presented works will be that the needed filters will be determined in time domain instead of in the frequency domain. This is possible due to the significantly improved processing powers since these methods were first described in the late 80s and 90s. In this thesis the very well explored iterative Least Mean Squares method will be used to determine the needed filters.

2. Theoretical Background

2.1. Fundamentals of Signal Processing

This chapter will quickly (re)introduce the most important concepts from acoustics and signal processing to refer to them throughout the thesis when necessary.

One of the most important tools for analyzing Linear and Time-Invariant (LTI) systems and predicting their behavior is the impulse response (IR). An impulse response is the output signal of a system which is excited with an impulse (a signal with an energy distribution in the complete frequency spectrum) usually described by the delta dirac distribution. Thus, the transmission behavior of a system can be completely described with an impulse response and output signals can be predicted for any input signals. In order to obtain such an output signal $Y(f)$ in frequency domain, the complex spectrum of the input signal $X(f)$ and the spectrum of the impulse response $H(f)$ are simply multiplied for each frequency:

$$Y(f) = H(f) \cdot X(f)\,. \tag{1}$$

However, in time domain this process becomes more complex. Here, to obtain the output signal $y(t)$, the input signal $x(t)$ must be convolved with the impulse response $h(t)$, described by the convolution integral

$$y(t) = \int_{-\infty}^{\infty} h(\tau)x(t-\tau)d\tau =: (h * x)(t)\,. \tag{2}$$

One important property of the convolution is that the signal order is interchangeable. The convolution integral can also be expressed as a finite convolution for the discrete time step n by

$$y(n) = \sum_{i=0}^{I-1} h(i)\, x(n-i)\,. \tag{3}$$

Here $h(i)$ denotes an impulse response with I coefficients, whose response is zero after some finite number of samples. This kind of impulse response is called an Finite Impulse Response (FIR) filter. As shown in [12], Eq. (3) can also be expressed in the form of vector inner/dot product such that

$$y(n) = \boldsymbol{h}^{\mathrm{T}}\, \boldsymbol{x}(n) = \boldsymbol{x}^{\mathrm{T}}(n)\, \boldsymbol{h}\,, \tag{4}$$

where T denotes the vector transpose and the vectors $\boldsymbol{h}$ and $\boldsymbol{x}(n)$ are defined by

$$\boldsymbol{h}^{\mathrm{T}} = [h(0), h(1), \dots, h(I-1)]\,, \tag{5}$$

$$\boldsymbol{x}^{\mathrm{T}}(n) = [x(n), x(n-1), \dots, x(n-I+1)]\,. \tag{6}$$

Note that the input signal $\boldsymbol{x}(n)$ is "inverted" in regard to the time samples.

To obtain such an impulse response in the first place, the system is stimulated with a suitable signal. In acoustics, white noise is usually best suited for this, as it has a uniform energy density in the frequency range. There are now several ways to deduce the impulse response using the input and output signal. Simply solving Eq. (1) for $H(f)$ makes the solution prone to noise during measurement. A way to estimate the IR whilst minimising effects by noise is the H_1 estimator, expressed as:

$$H_1(f) = \frac{G_{\mathrm{YX}}(f)}{G_{\mathrm{XX}}(f)} = \frac{Y(f)}{X(f)} \cdot \frac{\bar{X}(f)}{\bar{X}(f)}\,. \tag{7}$$

$\bar{X}(f)$ is the complex conjugate of $X(f)$, $G_{\mathrm{XX}}(f)$ is called the auto-spectrum of $X(f)$ and $G_{\mathrm{YX}}(f)$ is called the cross-spectrum between $Y(f)$ and $X(f)$. This estimation is especially reliable if there is only noise present at the measured output signal $Y(f)$. To further improve this estimation,

the input and output signals are spliced into blocks, the auto- and cross-spectra are calculated and then averaged over each iteration. The idea is that the deterministic part of the signal stays constant over the averaging process, whereas the contributing factor of the noise is decreased with every averaging step. To even further improve the results, the blocks can overlap each other, which effectively increases the number of averages without needing a longer signal. In this thesis the overlap will always be set to 1/4 of the block length.

With the averaged spectra at hand, the coherence function $\gamma^2(f)$ can be defined, a very useful tool when studying LTI systems

$$\gamma^2(f) = \frac{|\widetilde{G}_{\mathrm{XY}}(f)|^2}{\widetilde{G}_{\mathrm{XX}}(f)\widetilde{G}_{\mathrm{YY}}(f)}\,, \tag{8}$$

where the $\widetilde{\ }$ in the auto- and cross-spectra shows that they are averaged. Of course these averaged spectra will also be inserted in Eq. (7).

2.2. Active Absorption of plane waves inside a one dimensional duct

Before diving deep into the aspects of active sound absorption/active sound reduction in free field scenarios, the already well explored active absorption inside a one-dimensional duct will be revisited. A primary source only emitting plane waves is placed inside the duct. The aim is now to create two distinct areas, one where the sound field is cancelled (further away from the primary source) and one where the sound field is left undisturbed (closer to the primary source). To achieve this, a second, actively controlled sound field with the exactly right characteristics must be introduced inside the duct. The region between the origin of this secondary source field and the source emitting the primary sound field will be named the "Upstream" region and the region where both sound fields propagate in the same direction will be called the "Downstream" region. A scheme of a one dimensional duct where the described areas are indicated is shown in Fig. 1 below. However, it is quite self explanatory that a single secondary source can not cancel the downstream radiation of the primary source while also always ensuring zero upstream radiation. It was recognised by Swinbanks in 1973 [15] that this becomes possible once a *second* secondary

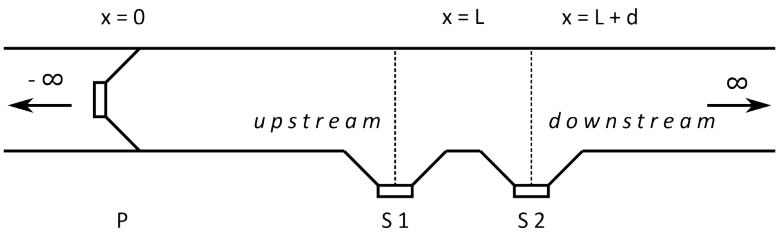

Figure 1: Scheme of the infinite duct.

source is introduced. The depiction in Fig. 1 marks the primary source with P, the first secondary source with S1 and the second secondary source with S2.

As demonstrated with detail in [12], if the first secondary source (S1) of source strength q_{S1} is placed with distance L, and further down a second secondary source (S2) is placed with distance $L + d$, zero *upstream* radiation can always be ensured if the source strength of S2 relates to S1 by

$$q_{\mathrm{S1}} = -q_{\mathrm{S2}}\, \mathrm{e}^{-jkd}\,, \tag{9}$$

or, equivalently, in the time domain by

$$q_{\mathrm{S1}} = -q_{\mathrm{S2}}\, (t - d/c_0)\,. \tag{10}$$

Interpreting this source strengths reveals that S1 has always the same strength as S2 but with flipped sign and delayed by the time the sound takes to travel the distance between them. S2 is *reflecting* the pressure field, S1 is *absorbing* it.

If the condition $p(x) = 0$ is applied for $x > L + d$ ("Downstream"), the source strength of S1 can be expressed in relation to the primary source strength q_p by [12]:

$$q_\mathrm{S1} = \frac{-q_\mathrm{P}\, \mathrm{e}^{-jkL}}{2j \sin kd}\,. \tag{11}$$

It becomes clear that the source strength must be infinite for frequencies where $\sin kd = 0$, or in other words where the distance d between the two secondary sources equals to an integer number of half wavelengths. This introduces the upper frequency limit of the bandwidth

$$f_\mathrm{up} = \frac{c}{2d}\,, \tag{12}$$

which will be of high importance for finding a solution with the Least Mean Squares (LMS) method. Now that the two secondary sources are adjusted to cancel downstream radiation without producing any upstream radiation, the net pressure field in the duct can be expressed as [12]:

$$p(x) = Z_0\, q_\mathrm{p} \mathrm{e}^{-jk|x|}\,, \qquad x \leq L\,, \tag{13a}$$

$$p(x) = Z_0\, \frac{q_\mathrm{p} \mathrm{e}^{-jkL}}{j2 \sin kd} \left[\mathrm{e}^{-jk(x-(L+d))} - \mathrm{e}^{jk(x-(L+d))}\right]\,, \qquad L \leq x \leq (L+d)\,, \tag{13b}$$

$$p(x) = 0\,, \qquad x \geq L + d\,, \tag{13c}$$

where $Z_0 = \rho_0 c_0 (2S)^{-1}$ is the real part of the transfer impedance and S being the area of the duct cross section. For $x \leq L$ the net pressure field equals the field of only the primary source and for $x \geq (L+d)$ there is no net pressure field. Between the two sources, however, a standing wave forms, whose amplitude goes to infinity as the distance d approaches $n\lambda/2$. For further illustration the superposition of the two secondary pressure fields and the resulting net pressure field for arbitrary values of L and d can be seen in Fig. 2 below.

Although the analytical consideration of the pressure is useful for the theoretical understanding of the phenomenon, the specification of the solution by the source strength is not trivial in the application. The time-dependent signals which are fed into the sources are better suited for this purpose. Therefore, the entire system will now be described by means of its impulse responses. The underlying assumption here is that the system is an LTI system. The biggest advantage of this approach is that all the properties of the hardware, such as the frequency response of the loudspeakers, the introduced delay by certain components, etc., become part of the analysis without having to be quantified.

Two microphones are added to the setup of Fig. 1, one in the Upstream and one in the Downstream area (see Fig. 3). Their labeling, "Reference Microphone" and "Error Microphone" are chosen in reference to the typical setup of a feedforward ANC system in a duct [12–14, 17]. The two output signals are the *reference signal* u_ref and the *error signal* u_err, although both signals will be used to determine how much the controller was "in error" since both areas are to be controlled. These signals will be used to impose boundary conditions. Note that the absolute positioning of S1 and S2 is no longer relevant as it becomes part of the system analysis, the same applies to the positioning of the microphones. Only the relative distance d needs to be taken into account since it determines the upper frequency limit (see Eq. (12)). The complete setup with further note on the signals can be seen below in Fig. 12 in Sec. 2.4.3.

Each microphone is reached by the emitted waves of every source, therefore a total of six transfer

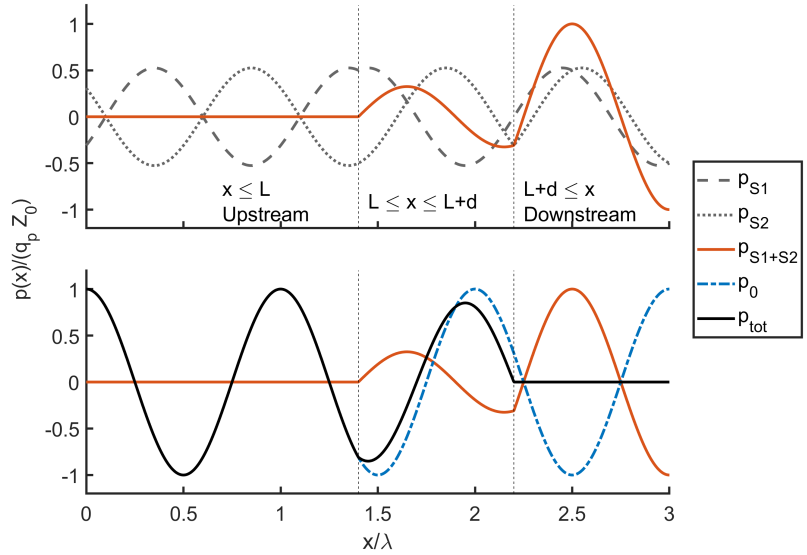

Figure 2: Visualisation of Eq. (13a) to Eq. (13c) with visual demarcation of the individual segments of x. The upper graph shows how the two emitted fields by the secondary sources (p_{S1} and p_{S2}) add up to the combined absorption field ($p_{\mathrm{S1+S2}}$). The bottom graph shows the primary pressure field of source P (p_0) which together with the absorption field $p_{\mathrm{S1+S2}}$ results in the net pressure field (p_{tot}).

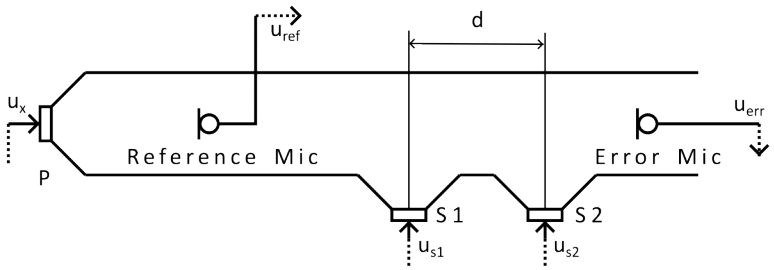

Figure 3: Scheme of the duct, including microphones.

paths are needed to describe the system[1]: two downstream (primary) paths of the primary source, one upstream (feedback) path and one downstream (error) path for the two secondary sources each. All six paths and their respective naming of the impulse responses are illustrated in Fig. 4. Note that only the transfer paths inside the duct are being displayed, however, the complete transfer paths also include the filters, cables, digital analog converter etc. (see, again, Fig. 12)

Now the measured signals at the microphones can be expressed by the convolution of the loudspeaker signals u_{x}, u_{s1} and u_{s2} and the respective impulse responses of the feedback and error paths:

$$u_{\mathrm{ref}} = u_{\mathrm{x}} * h_{\mathrm{p0}} + u_{\mathrm{s1}} * h_{\mathrm{f1}} + u_{\mathrm{s2}} * h_{\mathrm{f2}}\,, \tag{14a}$$

$$u_{\mathrm{err}} = u_{\mathrm{x}} * h_{\mathrm{p}} \; + u_{\mathrm{s1}} * h_{\mathrm{e1}} + u_{\mathrm{s2}} * h_{\mathrm{e2}}\,. \tag{14b}$$

[1]When applying the boundary conditions further down it becomes clear that only five out of the six transfer paths are needed to find the solution of the missing impulse responses. Nevertheless, all six are presented for the sake of completeness.

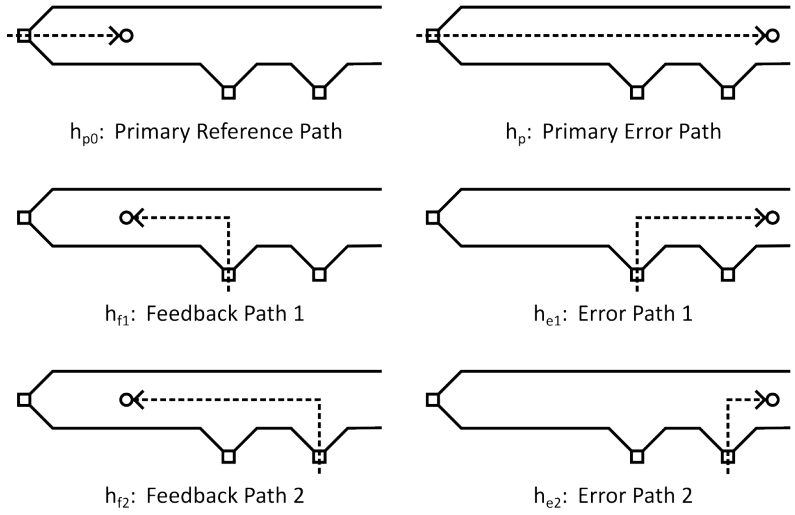

Figure 4: Transfer paths of the corresponding impulse responses inside the duct.

Now boundary conditions can be expressed with the two microphone signals:

$$u_{\mathrm{ref}} \overset{!}{=} u_{\mathrm{x}} * h_{\mathrm{p0}}\,, \tag{15a}$$

$$u_{\mathrm{err}} \overset{!}{=} 0\,. \tag{15b}$$

However, the composition of the loudspeaker signals u_{x} and especially u_{s1} and u_{s2} has not yet been analysed in detail. The signal u_{x} for the primary source is simply that: the signal transferred to the primary source. The signals u_{s1} and u_{s2} however must contain the filtered input signal u_{x}. The most obvious choice for this would be an FIR filter. The (still unknown) filter coefficients will be represented as IR, h_1 and h_2 for the first and second secondary source respectively. Now Eq. (14a) and Eq. (14b) can be redefined

$$u_{\mathrm{ref}} = u_{\mathrm{x}} * h_{\mathrm{p0}} + \underbrace{(h_1 * u_{\mathrm{x}})}_{:=u_{\mathrm{s1}}} * h_{\mathrm{f1}} + \underbrace{(h_2 * u_{\mathrm{x}})}_{:=u_{\mathrm{s2}}} * h_{\mathrm{f2}}\,, \tag{16a}$$

$$u_{\mathrm{err}} = u_{\mathrm{x}} * h_{\mathrm{p}} + \underbrace{(h_1 * u_{\mathrm{x}})}_{:=u_{\mathrm{s1}}} * h_{\mathrm{e1}} + \underbrace{(h_2 * u_{\mathrm{x}})}_{:=u_{\mathrm{s2}}} * h_{\mathrm{e2}}\,, \tag{16b}$$

and the boundary conditions from equations (15a) and (15b) can be applied[2]

$$\Rightarrow \qquad 0 \overset{!}{=} h_1 * u_{\mathrm{x}} * h_{\mathrm{f1}} + h_2 * u_{\mathrm{x}} * h_{\mathrm{f2}}\,, \tag{17a}$$

$$\Rightarrow \quad -u_{\mathrm{x}} * h_{\mathrm{p}} \overset{!}{=} h_1 * u_{\mathrm{x}} * h_{\mathrm{e1}} + h_2 * u_{\mathrm{x}} * h_{\mathrm{e2}}\,. \tag{17b}$$

Looking at these equations it becomes clear that the solution for h_1 and h_2 is independent of the input signal u_x. As such, this set of impulse responses can also be expressed as a matrix composed of vectors (see again Eq. (3) in Sec. 2.1 for the definition of the discrete convolution):

$$\begin{bmatrix} 0 \\ -\boldsymbol{h}_{\mathrm{p}} \end{bmatrix} = \begin{bmatrix} \boldsymbol{h}_{\mathrm{f1}} & \boldsymbol{h}_{\mathrm{f2}} \\ \boldsymbol{h}_{\mathrm{e1}} & \boldsymbol{h}_{\mathrm{e2}} \end{bmatrix} \cdot \begin{bmatrix} \boldsymbol{h}_1 \\ \boldsymbol{h}_2 \end{bmatrix}\,. \tag{18}$$

[2]Now it becomes clear why only five out of the six impulse responses are needed: h_{p0} is removed from the equations by applying the boundary condition.

It can be seen that this matrix equation corresponds to the simplest of all algebraic equations, $\boldsymbol{y} = \boldsymbol{A} \cdot \boldsymbol{x}$, where $\boldsymbol{x}$ is unknown. Countless methods have been developed over the course of time to solve equations of this form. The method used here (the LMS method) will be presented in the next section.

2.3. Solution method in time domain: The Least Mean Squares algorithm

This section gives an introduction to the least squares method and how the LMS algorithm derives from it, mostly based on the work presented by Nelson and Elliot in [12]. Further on the expression for a MIMO system that was introduced in the work of Kropp et. al. in [18] will be given and applied to the problem at hand.

The LMS algorithm invented by Widrow and Hoff in the 60s [19] became a standard tool in filter design. However, due to (the lack of) signal processing capabilities, historical usage of the design method usually focused on finding a solution in the frequency domain (as, for example, seen in great detail in [12]) to avoid the cost heavy convolution of the time domain signals. In recent years the LMS method gained a bigger popularity for filter designs in the time domain. This thesis will follow this and also propose to find solutions in the time domain. The original LMS method is described for a SISO system, which must be extended for use here. An approach to use the LMS for a Single Input Multiple Output (SIMO) system in time domain is explained in [20], later extended to a MIMO approach in [21] and applied in [22] and [18].

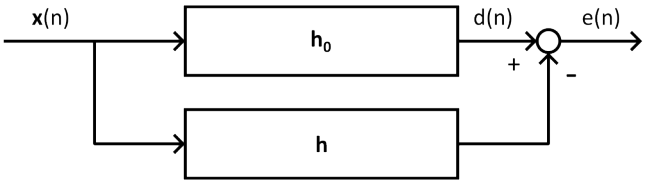

Figure 5: The general block diagram for an estimation problem of an FIR filter $\boldsymbol{h}$. $\boldsymbol{x}(n)$ is the input signal, $\boldsymbol{h}_0$ the desired/unknown impulse response function and $e(n)$ the error between the desired signal $d(n)$ and the signal created with the filter $\boldsymbol{h}$.

First the method of least squares is presented for a time domain estimation of a SISO system, illustrated in Fig. 5. The following presentation is based on the description given in [12]. A part of a digital signal $\boldsymbol{x}(n)$ is fed into an FIR digital filter $\boldsymbol{h}$ with I (unknown) coefficients. The desired (measured) signal $d(n)$ can now be compared with the filtered signal. The error $e(n)$ at each time step is given by

$$e(n) = d(n) - \boldsymbol{h}^{\mathrm{T}}\boldsymbol{x}(n)\,. \tag{19}$$

See Eq. (3)-(6) for the definition on the discrete convolution. The used criterion to adjust the coefficients in $\boldsymbol{h}$ is the expected value over the squared error sequence

$$E[e^2(n)] = E[(d(n) - \boldsymbol{h}^{\mathrm{T}}\boldsymbol{x}(n))^2]\,, \tag{20}$$

and using the two forms of Eq. (4) it can be expanded to

$$E[e^2(n)] = E[d^2(n)] - 2\boldsymbol{h}^{\mathrm{T}}E[\boldsymbol{x}(n)d(n)] + \boldsymbol{h}^{\mathrm{T}}E[\boldsymbol{x}(n)\boldsymbol{x}^{\mathrm{T}}(n)]\boldsymbol{h}\,. \tag{21a}$$

This equations shows that the mean square error is a quadratic function of each of the filter coefficients in $\boldsymbol{h}$. To make this even more clear, Eq. (21a) is rewritten as

$$E[e^2(n)] = E[d^2(n)] - 2\boldsymbol{h}^{\mathrm{T}}\boldsymbol{r} + \boldsymbol{h}^{\mathrm{T}}\boldsymbol{R}\boldsymbol{h}\,, \tag{21b}$$

with the introduced terms for the *cross-correlation* $\boldsymbol{r}$ between the input and the desired signal and the *auto-correlation* $\boldsymbol{R}$ of the input signal

$$\boldsymbol{r} = E[\boldsymbol{x}(n)d(n)] \quad \text{and} \quad \boldsymbol{R} = E[\boldsymbol{x}(n)\boldsymbol{x}^{\mathrm{T}}(n)]\,. \tag{22}$$

It can be noted that $\boldsymbol{R}$ is of *Toeplitz* form. For more details on the explicit matrix structure see [12], Ch. 4.

Theoretically, an optimal filter $\boldsymbol{h}_{\mathrm{opt}}$ can be found if Eq. (21a)/(21b) has a global minimum, which is provided if the third summand is always positive for all FIR filter $\boldsymbol{h} \neq \boldsymbol{0}$. This implies that the matrix $\boldsymbol{R}$ must be positive definite[3]. It is indeed insured that the matrix $\boldsymbol{R}$ is positive definite, if the signal $\boldsymbol{x}(n)$ is *persistently exciting*, which means that the two-sided spectrum of $\boldsymbol{x}(n)$ is nonzero at I or more points, where I is the number of coefficients in $\boldsymbol{h}$[4].

The minimum of a quadratic function is found by following its gradient, which is given by

$$\frac{\partial E[e^2(n)]}{\partial h_k} = 2E\left[e(n)\frac{\partial e(n)}{\partial h_k}\right] = -2E[e(n)x(n-k)]\,. \tag{23}$$

Using Eq. (19) to expand $e(n)$, Eq. (23) can be expressed with the known terms $\boldsymbol{r}$ and $\boldsymbol{R}$ from Eq. (22)

$$\frac{\partial E[e^2(n)]}{\partial h_k} = -2\left[\boldsymbol{r} - \boldsymbol{h}^{\mathrm{T}}\boldsymbol{R}\right]\,. \tag{24}$$

Setting the gradient to zero to find its minimum, a simple matrix equation is expressed

$$\boldsymbol{r} = \boldsymbol{R}\boldsymbol{h}_{\mathrm{opt}}\,. \tag{25}$$

Since it is assumed that $\boldsymbol{R}$ is not singular (as discussed above), this expression can be solved for the optimal filter

$$\boldsymbol{h}_{\mathrm{opt}} = \boldsymbol{R}^{-1}\boldsymbol{r}\,. \tag{26}$$

This filter is called the Wiener Filter. There are many reasons not to use the optimum solution.

The most obvious one is that an inversion of a matrix is always computationally expensive. Although the cost of calculating the inverse has fallen significantly since the development of the method in the 1960s thanks to special inversion methods for Toeplitz matrices (see e.g. [28, 29]) and the generally exponential increase in computing power, this time-consuming step should still be avoided today, especially if the method is to be used in a real time. Furthermore, the auto- and cross-correlations will in practice most likely be obtained by their power- and cross-spectral densities, which makes multiple Fourier transformations necessary, which are also computationally expensive. Furthermore this solution will be very susceptible to noise, which will quickly lead to an ill-conditioned $\boldsymbol{R}$.

An alternative method (which leads to the definition of the LMS algorithm) which is more robust will be used instead. An important property of the estimation problem discussed above is that its error surface is quadratic, therefore, a simple gradient descent method is guaranteed to converge towards the global optimum (provided it is stable). Based on the method of steepest descent, the algorithm to determine the ith coefficient of the FIR filter is given as

$$h_i(\mathrm{new}) = h_i(\mathrm{old}) - \mu\frac{\partial E[e^2(n)]}{\partial h_i}\bigg|_{h_i = h_i(\mathrm{old})}\,, \tag{27}$$

[3] A matrix $\boldsymbol{A}$ is positive definite if $\boldsymbol{x}\boldsymbol{A}\boldsymbol{x} > 0$ for all $\boldsymbol{x} \neq \boldsymbol{0}$ which is true if all eigenvalues λ_i of $\boldsymbol{A}$ are greater than 0. More notes on linear algebra and its implications on physical systems can be found in [12, 23, 24].

[4] Strictly speaking this is the definition of a *weakly persistently exciting* signal. As it is not relevant in the context of the LMS whether the signal is of *weak* or *strong* persistent excitation, it will not be discussed further. Lengthy discussion can be found in [25–27], with a proof provided in [25], Ch. 3.4.

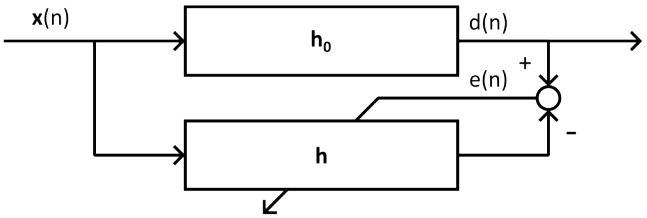

Figure 6: Block diagram of an estimation problem where the FIR filter $\boldsymbol{h}$ is adapted in regard to the instantaneous error $e(n)$.

where μ is a convergence coefficient and the gradient term is expressed as in Eq. (23) [12]. However, although this does avoid a matrix inversion, it would still include a lengthy averaging process for the expectation value of $E[e^2(n)]$. One crucial discovery by Widrow and Hoff in 1960 [19] was that the true gradient can be estimated by differentiating the *instantaneous* error instead and that it will converge to the true gradient over time. This leads to an **adaptive algorithm** which can be expressed in vector terms as

$$\boldsymbol{h}(n+1) = \boldsymbol{h}(n) + \alpha\, e(n)\boldsymbol{x}(n)\,, \tag{28}$$

where α is another conversion coefficient and

$$\boldsymbol{h}^{\mathrm{T}}(n) = [h_0(n), h_1(n), \ldots, h_{I-1}(n)]\,, \tag{29}$$

is the now *time varying* FIR filter, which coefficients will be optimised over time. The updated diagram of an adaptive digital filter is seen in Fig. 6.

The expression in Eq. (28) is widely known as the *LMS algorithm*. It becomes clear that the gradient is mostly determined by the strongest error, therefore the algorithm will always try to remove the part of the FIR filter which leads to the biggest error first. The convergence of the LMS algorithm has been discussed in great detail (e.g. [30–32]) and will not be analysed further here. A "rule of thumb" for the convergence was introduced by Widrow et. al in 1976 [33]. The algorithm will usually converge to the Wiener Filter solution if the convergence coefficient α satisfies

$$0 < \alpha \leq \frac{1}{IE[x^2(n)]}\,, \tag{30}$$

where $E[x^2(n)]$ is the mean square value of the input signal and I is the number of filter coefficients.

Although the introduction of the LMS algorithm was quite lengthy, the update rule itself in Eq. (28) is quite simple to implement. But in order to apply the LMS algorithm to the problem at hand, the approach must be extended to a MIMO system first. In [18], Kropp et. al. successfully demonstrated how the LMS algorithm can be extended to a MIMO system in order to restore input signals. Based on this formulation, an update rule for a MIMO system is expressed as

$$\boldsymbol{h}_i(n+1) = \boldsymbol{h}_i(n) + 2\frac{1}{R}\sum_{r=1}^{R}\alpha_r e_r(n)\boldsymbol{x}_{i,r}(n)\,, \tag{31}$$

where i now denotes the ith of total of I sources and r the rth receiving position of R total receiving positions. This gives an update rule for every single FIR filter, where the error term is defined as

$$e_r(n) = d_r(n) - \sum_{i=1}^{I}\boldsymbol{x}_{i,r}(n)\boldsymbol{h}_i\,. \tag{32}$$

It becomes clear that the error terms now are a superposition of the responses due to all sources. Therefore, in Eq. (31) the mean gradient is calculated and the strongest error in all of the error terms will determine the gradient. The resulting update rule in Eq. (31) will now be written out explicitly for the problem introduced in Sec. 2.2. This representation of the signals makes use of the fact that the order of convolution is interchangeable, as mentioned in Sec. 2.1.

$$\boldsymbol{h}_1(n+1) = \boldsymbol{h}_1(n) + \alpha_1 e_1(n)(\boldsymbol{u}_{\mathrm{f1}}(n) + \boldsymbol{u}_{\mathrm{e1}}(n))\,, \tag{33a}$$

$$\boldsymbol{h}_2(n+1) = \boldsymbol{h}_2(n) + \alpha_2 e_2(n)(\boldsymbol{u}_{\mathrm{f2}}(n) + \boldsymbol{u}_{\mathrm{e2}}(n))\,, \tag{33b}$$

with the error terms defined as seen in Fig. 7

$$e_1(n) = -\boldsymbol{u}_{\mathrm{f1}}(n)\,\boldsymbol{h}_1 - \boldsymbol{u}_{\mathrm{f2}}(n)\,\boldsymbol{h}_2\,, \tag{34a}$$

$$e_2(n) = -\boldsymbol{u}_{\mathrm{e1}}(n)\,\boldsymbol{h}_1 - \boldsymbol{u}_{\mathrm{e2}}(n)\,\boldsymbol{h}_2 - \boldsymbol{u}_{\mathrm{p}}(n)\,, \tag{34b}$$

where the signals $\boldsymbol{u}_{\mathrm{f1}}(n), \boldsymbol{u}_{\mathrm{f2}}(n), \boldsymbol{u}_{\mathrm{e1}}(n)$ and $\boldsymbol{u}_{\mathrm{e2}}(n)$ are cut from the entire convolution of the input signal $\boldsymbol{u}_x(n)$ with the respective duct transfer paths in a way that they are equal to the definition given in Eq. (6). Again, refer to Fig. 7 for more clarification.

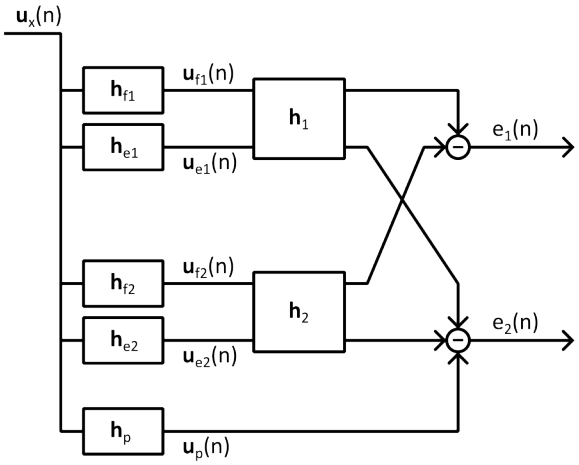

Figure 7: LMS MIMO Paths

Now a general description of what is needed for an implementation of the LMS algorithm is given. A validation of the method for the one dimensional active absorption is given in the following section.

2.4. Active Absorption inside the duct: Validation of the LMS method

To validate the proposed LMS algorithm for a MIMO system, it is tested for the well known case of the one dimensional duct, for which the analytical results were presented in Sec. 2.2. First the duct will be simulated as an infinite, one-dimensional tube with three sources of the same strength. In such a duct, only plane waves can travel, expressed as

$$p(x,k) = A\,\mathrm{e}^{j(-kx)}\,, \tag{35}$$

where A stands for the source strength and a possible unit-based conversion to pressure. Here, A

is simply set to equal 1 for all three sources, which will always leads to $|p| = 1$ [5]. The simulated distance L between P and S1 is set to 3 m, the distance d between S1 and S2 is set to 0.15 m. This results in an upper frequency limit of $f_{\mathrm{up}} \approx 1$ kHz. The reference and the error microphone are placed at 0.5 m and 3.5 m respectively. The impulse response functions can be seen in Fig. 8a.

One important aspect when designing any filter is the sampling frequency f_{s}. It has influence on the convergence speed, as the sampling frequency largely determines the shape of the error surface and the steepness of its gradients. A common recommendation is to set f_{s} to approx. ten times the frequency of interest [14]. The assumption is that this is a good compromise between fast convergence and stability. Here the frequencies of interest are mostly between 50 Hz up to a few hundred Hz, so the sampling frequency is set to 2.56 kHz. This also avoids spacial aliasing for the described setup of an upper frequency limit of $f_{\mathrm{up}} \approx 1$ kHz.

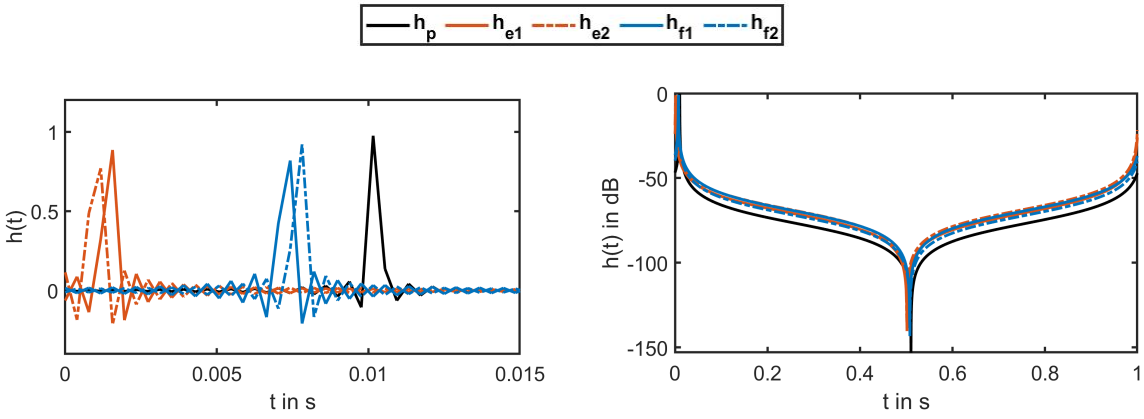

(a) (b)

Figure 8: Impulse responses of the duct sampled at $f_{\mathrm{s}} = 2.56$ kHz.

As expected, the impulse responses show a strong peak with an amplitude of ≈ 1 after a time delay corresponding to the distance between source and respective microphone. In Fig. 8b the entire impulse response is shown on a dB scale. It is interesting to note that this way of determining the impulse responses leads to a symmetric (and implausible) impulse response in time domain. After 0.11 s or 283 samples, all impulse responses have decayed by at least -60 dB, which indicates a reasonable minimal value to cut off the impulse response for further use. Here 450 samples (0.16 s) are chosen to cut off all impulse responses.

Now all that is needed to perform the LMS algorithm is to determine the convergence coefficients α_1 and α_2. However, this task is not trivial and is the focus of the next subsection.

2.4.1. Setting the convergence coefficients of the LMS Algorithm

The convergence factors are very important: they determine the quality of the solution and whether the algorithm converges to a solution at all. As mentioned previously, there is no formula on how to determine the convergence coefficient for a SISO system, only a rule of thumb (Eq. (30)), for a MIMO system there is even less. However, this rule of thumb will be used as a starting point to find usable convergence coefficients.

[5] The chosen notation for this thesis does not explicitly note when a quantity is complex, as it is usually obvious from context. This can be confusing in the context of acoustic pressure, but since both the simulation and the subsequent measurement results are not directly translated into pressure fluctuations, this confusion should be bearable.

Another level of complexity arrives from the fact that with the described system, although quite minimal, a lot of quantities might (and, as will shortly be shown, in fact do) have an influence on which coefficients lead to a convergence. Some obvious candidates are the energy of the input signal, the lower and upper end of the bandwidth, the number of coefficients of the filters and the magnitude of the coefficients $\alpha_{1,2}$. A completely new quantity introduced by the MIMO system is the *ratio* of the two coefficients α_1/α_2.

This section cannot replace a thorough analysis on how to relate $\alpha_{1,2}$ to each other and all the other quantities mentioned and not mentioned, but this analysis would go beyond the scope of this thesis. It only tries to give some insight on how they *might* relate to each other for the system at hand to be able to find values for $\alpha_{1,2}$ that lead to a ("good") convergence. Finally, it must be said that the approach presented here is very 'engineer-like' and can certainly be improved.

The LMS algorithm is implemented according to Eq. (33) and Eq. (34). As input sequence serves a bandpassed[6] white noise signal with 10^6 samples. For every iteration step a part of that random sequence is cut out and assigned as the current input signal $u_x(n)$ to perform the convolutions. $u_x(n)$ is iterated forward within the random sequence with each iteration step. Therefore $u_x(n)$ only starts to repeat after $\sim 10^6$ steps.

In order to assess the convergence the progression of the error over the iteration steps gets evaluated (again, see Eq. (34) for the definition of the error terms). The error convergence gives a first impression of the quality of the solution, which is supplemented here by analysing the frequency response of the "downstream" and the "upstream" path. The "downstream" path denotes the frequency response of Eq. (17b), where the *estimated* response stems from the filtered source signals and the *desired* response stems from the negative primary path[7]:

$$\mathrm{DFT}\{17b\} \Rightarrow \underbrace{-P(f)}_{\text{desired}} \overset{!}{=} \underbrace{H_1(f)\cdot E_1(f) + H_2(f)\cdot E_2(f)}_{\text{estimated downstream path}} . \tag{36}$$

The "upstream" path can be defined in the same way:

$$\mathrm{DFT}\{17a\} \Rightarrow \underbrace{0}_{\text{desired}} \overset{!}{=} \underbrace{H_1(f)\cdot F_1(f) + H_2(f)\cdot F_2(f)}_{\text{estimated upstream path}} . \tag{37}$$

In both equations f denotes a single frequency bin.

Simply setting the coefficients in accordance with Eq. (30) is clearly not enough. With some trial and error it was found that the solution converges with a good success rate if

$$\alpha_2 = 7 \cdot \alpha_1 . \tag{38}$$

There are probably better ratios to be found, but this one has proven to be quite good for all the scenarios discussed in this thesis. In the following, if only the value for α_1 is mentioned, it can be assumed that α_2 is set accordingly to this rule. Furthermore, the lower end of the frequency end has a huge impact on the quality of the found solution. A more in-depth discussion with examples on how different coefficients and frequency ranges affect the results is given in Appx. A.

2.4.2. Simulated Results

The solution for $\alpha_1 = 50 \cdot 10^{-5}$ and a frequency range between 80 Hz to 1 kHz is displayed in Fig. 9. The error progressions are shown in Fig. 9a. Both reach a stable level of very little progression

[6] Hamming window of 256-th order bandpass, stopband at -60 dB. The bandwidth of the bandpass filter is equal to that of the filter bandwidth. Created with the `Matlab` command `fir1`.

[7] Note that the input signal u_x was omitted from the DFT as it is not necessary for this analysis.

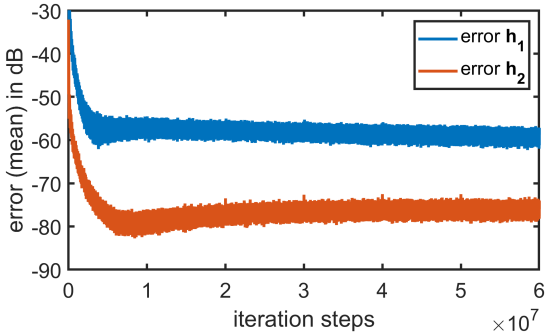

(a) Error progression over iteration steps, moving average applied.

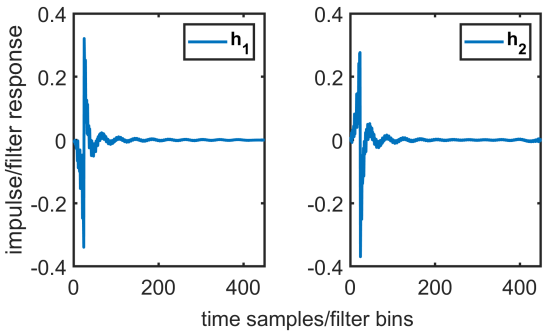

(b) Estimated FIR filters.

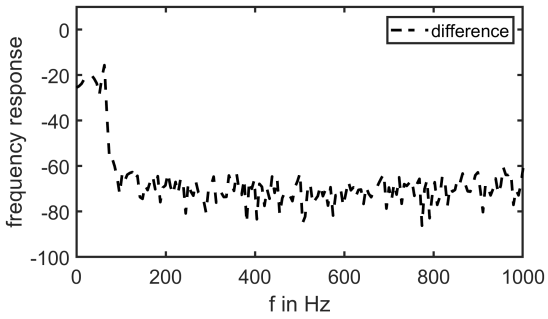

(c) Relative difference of the estimated frequency response of the upstream path.

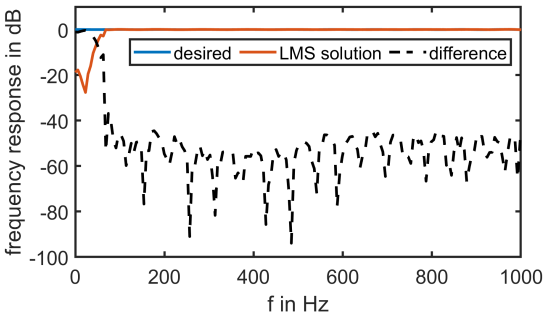

(d) Estimated frequency response of the downstream path and relative difference.

Figure 9: Analyitcal Duct Simulation: Different graphs of the solution of the LMS algorithm for $\alpha_1 = 50 \cdot 10^{-5}, \alpha_2 = 7 \cdot \alpha_1$, 80 Hz - 1 kHz after $6 \cdot 10^7$ iterations.

very quickly. The simulation was stopped after $6 \cdot 10^7$ iterations which leads to an error level of -58 dB and -75 dB for $\boldsymbol{h}_1$ and $\boldsymbol{h}_2$ respectively, but if it had been stopped only after $1 \cdot 10^7$ steps, those values would differ by less than 3 dB. With further iterations the solution is only improved marginally, but the distance between the two errors *decreases* slightly. It is possible that with even more iterations, the two errors slowly approach each other and converge toward the -66 dB line (the center between the two errors). This graph also gives another insight: this process might be improved drastically if an adaptive stepsize was implemented. However, this must remain a speculation at this point as it will not be investigated in this thesis.

The estimated FIR filters (Fig. 9b) both show two impulses (a positive and a negative one) followed by a quick decay of the response. They are almost perfect inversions of each other, as if the solution had been "flipped" along the abscissa. This was to be expected, as the analytical solution for the source strengths (compare Eq. (9)) implies exactly that behaviour.

The frequency response of the downstream path (Fig. 9d) shows a difference consistently below the -40 dB line with an average of -54 dB within the absorbing frequency range. Within this range, the upstream path (Fig. 9c) even consistently stays below -60 dB, with an average of -70 dB. As the desired signal for the upstream radiation lies at $-\infty$ dB, the upstream signal has a *literal* magnitude of less then -60 dB, whereas the signal downstream is reduced *relatively* by at least -40 dB, which of course in this case also corresponds to a literal reduction of at least -40 dB.

To show that these reductions actually translate into an absorption of energy at the boundary condition, the normalised Power Spectral Density (PSD) for both the upstream and downstream

position are plotted in Fig. 10 to compare the present energy with and without the active LMS. The mean added energy by the LMS to the signal of the primary path measured at the reference microphone position (Fig. 10a) is 0.38 $\cdot 10^{-3}$ dB with a standard deviation of 6.11 $\cdot 10^{-3}$ dB. This illustrates how barely any energy is emitted upstream by the two secondary sources. The PSD shows a great reduction of energy at the downstream position with a mean reduction of -97.83 dB and a standard deviation of 7 dB.

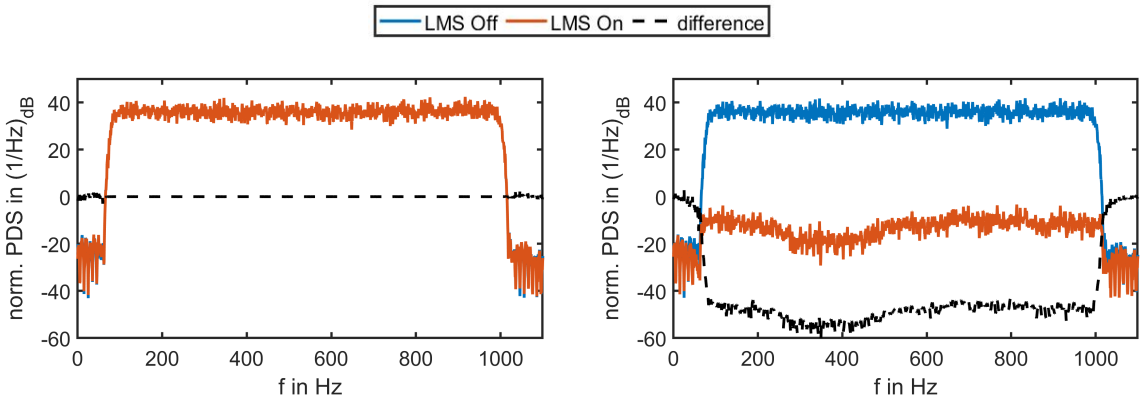

(a) Reference Microphone (Upstream).

(b) Error Microphone (Downstream).

Figure 10: Comparing PSDs with and without active absorption for both microphones.

When comparing the path estimations in Fig. 9c/Fig. 9d with the PSD ghraphs in Fig. 10a/Fig. 10b, it becomes clear that they represent the same information, but now the reference is in both cases the power density of the primary signal. It can even be noted that the course of the difference at the Error Microphone in Fig. 10b exactly represents the course of the difference in path estimation seen in Fig. 9d, but without the dips. Therefore, in the following only the PSD graphs will be evaluated instead of the path estimations used within the LMS algorithm.

Some characteristic values about the achieved differences are summarised below in Tab. 1. To express the deviation from the average achieved reduction, the Average Absolute Deviation (AAD) is used

$$\text{AAD:} \qquad \frac{1}{n}\sum_{i=1}^{n}|x_i - \tilde{x}|\,. \tag{39}$$

where n is the number of samples within the valid frequency range and $\tilde{x}$ is the average value, here the arithmetical mean is used as the average value.

	∅ reduction (dB)	max./min. reduction (dB)	max./min. reduction at $f_{\max}/f_{\min}$ (Hz)	AAD (dB)
Ref. Mic.	0.00	-0.01 / 0.01	987 / 256	0.00
Err. Mic.	-48.92	-63.35 / -40.61	348 / 80	3.68

Table 1: Simulation of the infinite duct. Average reduction in dB, maximal and minimal reduction in dB with corresponding frequency and AAD in dB. Corresponding graphs: Fig. 9 and Fig. 10.

For the sake of completeness, this achieved absorption will now also be evaluated for the reduction of the (pressure) amplitudes in time domain. Fig. 11a shows the achieved absorption for a 1 second

long band-passed[8] white noise signal and the recordings at the Error Microphone (Downstream) and the Reference Microphone (Upstream). Except for a short transient time in the beginning, the error signal continuously stays below -40 dB, with an average of -59 dB. The same applies for the reference signal, after a short transient time it continuously stays below -60 dB, with an average of -77 dB. The AAD for all three signals is ≈ 9 dB.

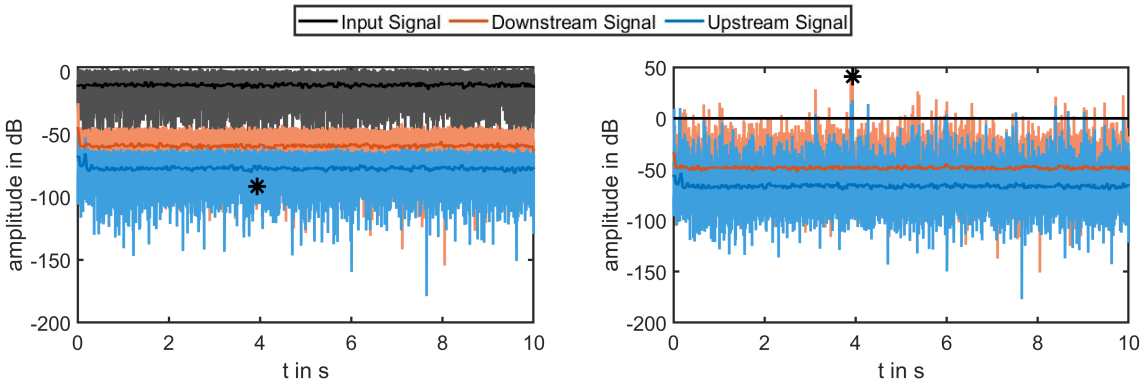

(a) Absolute absorption.

(b) Relative absorption.

Figure 11: Absorption of the signals inside the duct in time domain.

Fig. 11b shows the *relative* absorption of those three signals. Excluding the transient time, an averaged relative absorption of -48 dB downstream and an averaged relative absorption of -66 dB upstream are achieved. Those averages are very close to the predicted values from the path estimation and the PSD graphs. However, there are some outliers. One hefty outlier is marked with a star in both graphs. Here the relative absorption reaches +41 dB, amplifying the original signal by a factor of 100. At first this sounds alarming, but when looking again at Fig. 11a, it makes sense: at this specific data point the input signal has a magnitude of -90 dB, which lies below the achievable absorption. Therefore, the signal is amplified instead of absorbed.

2.4.3. Experimental Results

The simulation results presented in the previous section are very promising. In order to understand how the method performs in a real system and what possible limitations arise, the results of a physical set-up of the one-dimensional pipe are analysed below. The setup used is based on the existing setup used in a course at the Chalmers University of Technology in the Department of Technical Acoustics[9] which can be seen in Fig. 14. The design was only slightly modified and not fundamentally changed. The characteristics of the individual components remain unknown, however some examination reveal non-optimal behaviour, like heavy distortions present in the tube. It can be assumed that the three sources differ (greatly) in their frequency responses and their sensitivities, which makes it perfect for demonstrating the strengths of the LMS method, as parts of the setup essentially form a black-box. Fig. 12 show the used setup. The biggest difference between this schematic setup and the actual setup is that the duct describes two tight curves that deflect the signal (also compare to Fig. 58 in Appx. C for a better view). The physical distance between S1 and S2 is roughly 0.2 m, again putting the upper frequency close to 1 kHz. The sampling frequency is again set to 2.56 kHz. As the used interface[10] is not inherently able to sample at that

[8] Within the working range of the LMS to demonstrate the most effect.

[9] *Digital Signal Processing for Audio Engineering and Active Sound and Vibration Control.* More information on http://www.ta.chalmers.se/

[10] Antelope Orion 32 Gen 1 by Antelope Audio, also see Tab. 3 in Sec. 3.

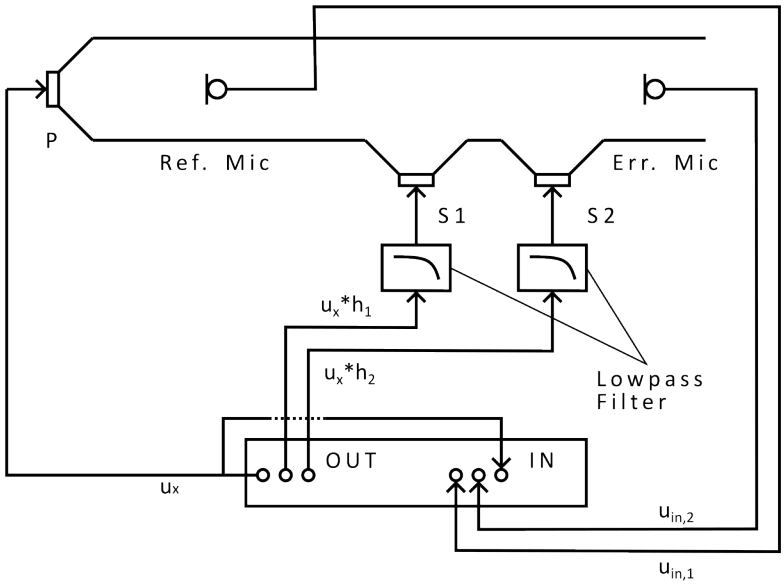

Figure 12: Setup of the Duct.

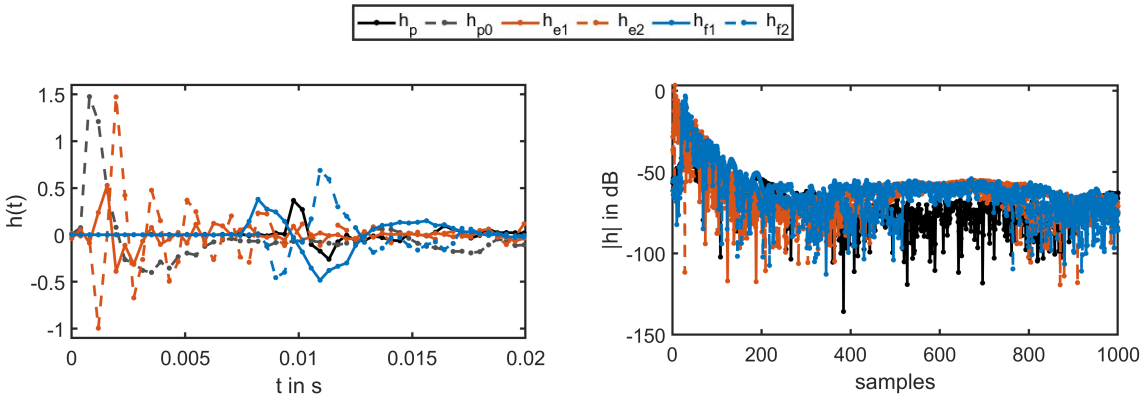

(a) (b)

Figure 13: Measured impulse responses of the duct, downsampled to $f_s = 2.56$ kHz.

rate, the signals were resampled with `Matlab's` command `resample`. Some additional digital low pass filtering was applied to reduce aliasing introduced by resampling the signal.

Fig. 15b shows the first 0.02 s of the measured impulse responses. When comparing $\boldsymbol{h}_{\mathrm{p0}}$ to $\boldsymbol{h}_{\mathrm{p1}}$ it becomes clear that energy is lost within the transmission process. The physical distance between the primary source and the reference microphone is roughly 0.1 m, whereas to the error microphone it roughly spans 3 m while also traversing two tight bends of the duct. Over this distance, the amplitude of the impulse response drops from 1.47 to merely 0.37, a reduction by 75%. This of course is a very different behaviour from the assumed plane waves for the analysis in the previous Sections. Fig. 13b shows the decay of the impulse responses. Again 450 samples are chosen as the cutoff length and the length for the filters $\boldsymbol{h}_1$ and $\boldsymbol{h}_2$. As already mentioned, the duct shows some non-optimal behaviour and the actual frequency range was set to 180 Hz - 480 Hz for the LMS method to be able to converge. The convergence factor α_1 was set to $5 \cdot 10^{-7}$ over $2 \cdot 10^8$ iteration steps. Fig. 15 shows the results. The mean error for $\boldsymbol{h}_1$ reaches -55 dB, the mean error

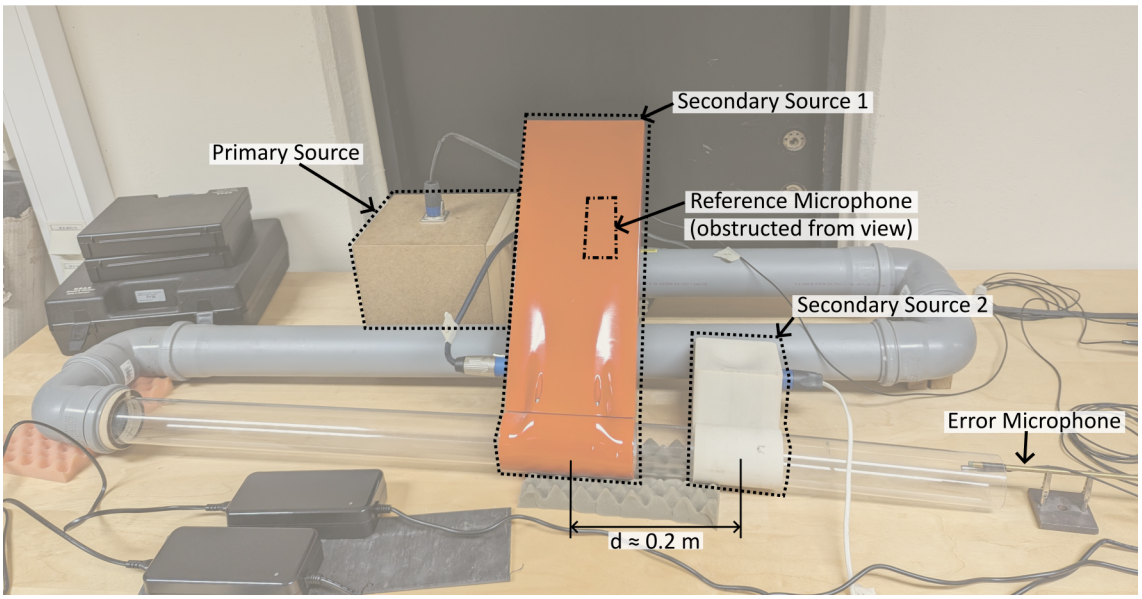

Figure 14: Setup for sound absorption inside of the one dimensional duct.

for $\boldsymbol{h}_2$ -65 dB (Fig. 15a). Due to the different characteristics of S1 and S2 the two filters $\boldsymbol{h}_1$ and $\boldsymbol{h}_2$ (Fig. 15b) are no longer almost perfect reflections of each other, but the main characteristic of being inverted remains. The estimated power densities at the Reference and Error Microphone also look very good, with a very minimal average deviation at the upstream position (Fig. 16c) and an average relative reduction of -36 dB at the downstream position (Fig. 16d), also summarised in Tab. 2.

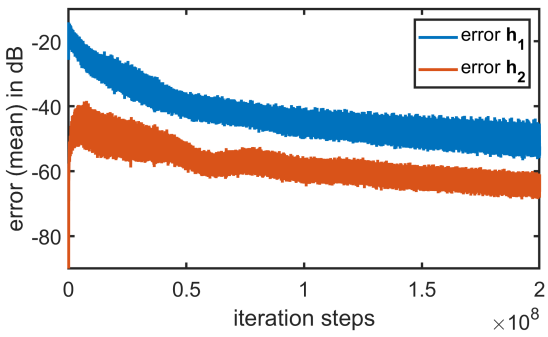

(a) Error progression over iteration steps, moving average applied.

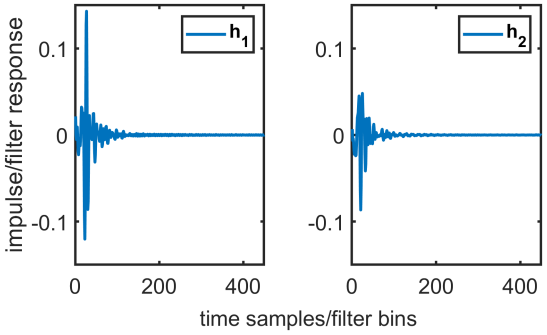

(b) Estimated FIR filters.

Figure 15: Experimental Duct Validation: Different graphs of the solution of the LMS algorithm for $\alpha_1 = 5 \cdot 10^{-7}, \alpha_2 = 7 \cdot \alpha_1$, 180 Hz - 480 Hz after $2 \cdot 10^8$ iterations.

However, when looking at the actually measured power densities in the top row of Fig. 16, a problem becomes clear. Whilst the downstream absorption of the signal works quite well with a significant average relative absorption of -25.49 dB and an AAD of 3.68 dB, the upstream signal now is amplified on average by 3.9 dB with an AAD of 2.35 dB. It is noticeable that the result is much better and closer to expectations at the microphone which position is right next to the two secondary sources. Therefore, that poor performance at the upstream position is probably best explained by the distortions introduced by the duct.

This gives two important insights, which were suspected from the beginning. First, the LMS method can deal with distortions and other disturbing effects only to a certain extent with the approach presented. Second, the simulated results show the upper limit for what is theoretically possible with a given setup and are valuable for planning an experiment, but the real performance is lower.

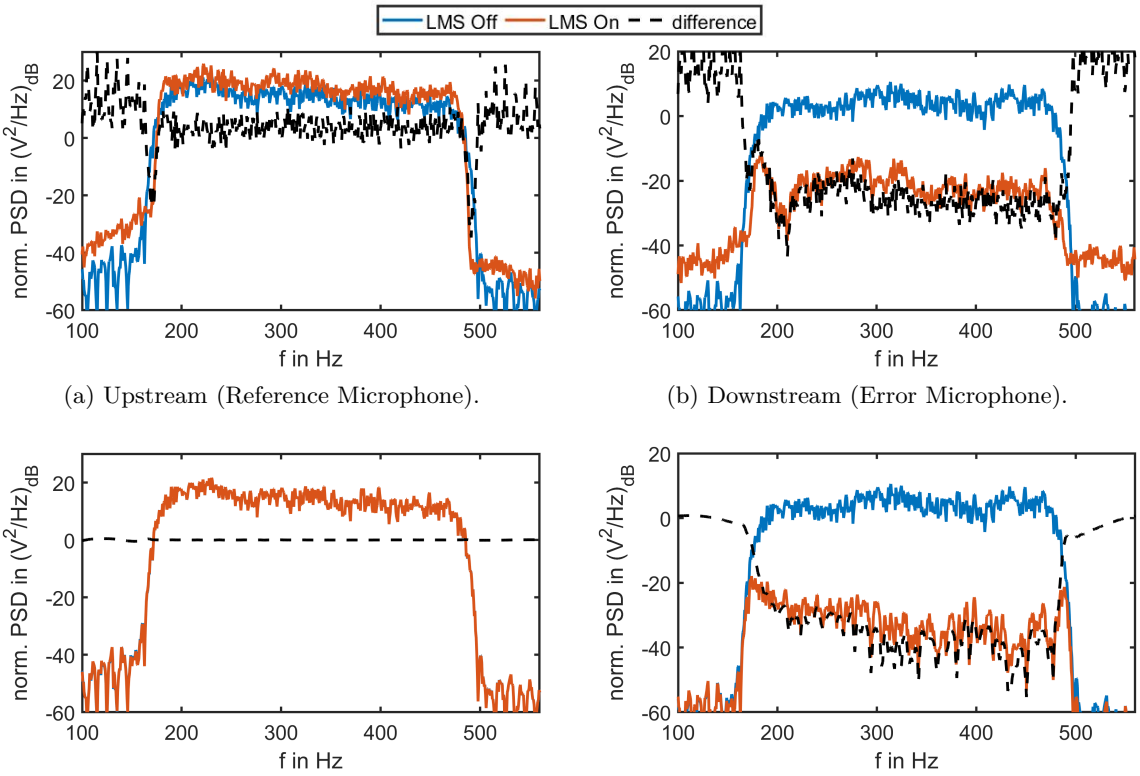

(a) Upstream (Reference Microphone).

(b) Downstream (Error Microphone).

(c) Upstream (Reference Microphone), simulated.

(d) Downstream (Error Microphone), simulated.

Figure 16: Normalised PSD at the two microphone positions, with absorption levels. Measured values at the top, expected values at the bottom.

	∅ reduction (dB)	max./min. reduction (dB)	max./min. reduction at f_{max}/f_{min} (Hz)	AAD (dB)
Ref. Mic.	3.90	-4.97 / 11.25	245 / 306	2.35
Err. Mic.	-25.49	-43.48 / -7.13	210 / 181	3.68
Ref. Mic. (simulated)	0.00	-0.04 / 0.05	283 / 206	0.01
Err. Mic. (simulated)	-36.27	-55.34 / -16.72	450 / 180	5.08

Table 2: Estimated active reduction for Reference and Error Microphone as a result of the LMS method for the duct, in comparison to the actually achieved reductions. Average reduction in dB, maximal and minimal reduction in dB with corresponding frequency and AAD in dB. Corresponding graph: Fig. 16.

2.5. Active Absorption of cylindrical waves with line arrays

Based on the already well-studied absorption of sound in a pipe (in literature and also partially in this thesis), the approach presented here is to be extended. The logical step to extend the application possibilities of active absorption is to leave the duct and plane waves behind and thus extend to higher dimensions: two and three dimensional waves in open space. This section will deal with two dimensional (cylindrical) waves and the next with three dimensional (spherical) waves. The cylindrical wave describes a solution to partial differential wave equation in two dimensions

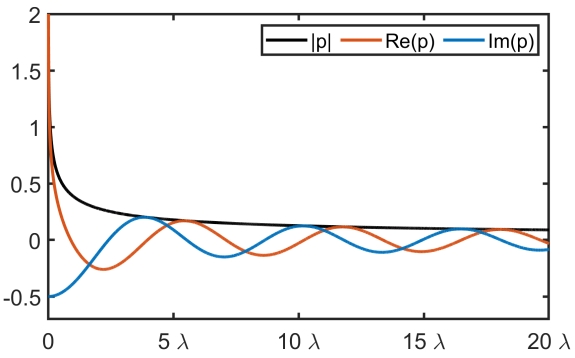

Figure 17: The pressure curve of the cylindrical wave, described by the altered (see Eq. (41), A=2) second-order Hankel function.

and it is expressed by the Hankel function of second kind

$$H_n^{(2)}(z) = J_n(z) - j\,Y_n(z)\,, \tag{40}$$

where $J_n(z)$ is the Bessel function of the first kind and $Y_n(z)$ the Bessel function of the second kind [34]. To express the pressure of the cylindrical wave this leads to

$$p(r,k) = A(-\frac{1}{4}j)\,H_0^{(2)}(k\cdot r)\,, \tag{41}$$

where r is the radial distance, k the wave number and A is again the source strength q, possibly combined with a unit conversion. As a perfectly reflecting ground underneath the source will be assumed and units are of no importance now, A is set to 2. The visualisation of the pressure curve can be seen in Fig. 17. The most obvious difference to a plane wave is that, although no energy is lost, $|p|$ decays over the distance. To be precise, $|p|$ decreases by 3 dB with every doubling of the distance. As seen in Fig. 17, Re(p) (and therefore $|p|$) approaches infinity for $k\cdot r$ approaching zero. For implementing this function, the Matlab function `besselh` is used, which is not defined for $k\cdot r = 0$.

Starting from the duct, the structure is now extended to the next dimension. First the continuous line source will be examined, but with the discrete line source already in mind, the setup will be placed in a three dimensional space. The new setup (with a top down view) can be seen in Fig. 18a (the scheme of the one dimensional scheme can be found further up in Fig. 3 for comparison). While looking at the line source it can be assumed that all physical quantities are independent of the y-coordinate. All impulse responses are defined in analogy to the duct (again, see Fig. 4) and won't be expressed again. With a wave that decays in amplitude, the exact positioning of the boundary conditions will most likely play a role, therefore the distances m_1 and m_2 were added, describing the positions of the Reference and the Error Microphone. When analysing the emerging areas inside the duct it was found that the areas can mostly be separated in the Upstream and Downstream area where a uniform pressure field forms (this was visualised in Fig. 2). It can be assumed that fore more dimensional waves, the absorption values within these areas are subject

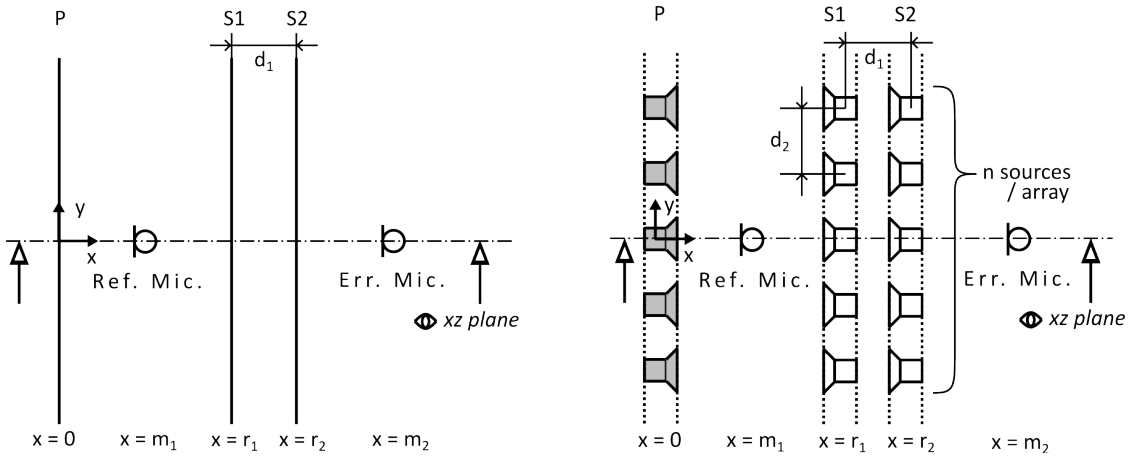

(a) Lines Sources. (b) Discrete Arrays.

Figure 18: Scheme of the infinite line sources (left) and the discrete line arrays (right).

to deviations. It will therefore not be sufficient to analyse the achieved absorption directly at the microphones alone; instead, the entire resulting pressure field must be considered.

To visualise the entire field at once is not directly possible. Either the relative reduction achieved at a fixed point can be displayed over the entire frequency range (as before) or absorption values can be displayed over a sectional area for a single frequency. To achieve the latter, the resulting pressure fields from each line source ($p_{\mathrm{P}}(f,x,z)$, $p_{\mathrm{S1}}(f,x,z)$ and $p_{\mathrm{S2}}(f,x,z)$) are calculated according to Eq. (41) for a fixed wave number k. To apply the FIR filters for a fixed frequency, $\boldsymbol{h}_1(t)$ and $\boldsymbol{h}_2(t)$ must be Fourier transformed into $\boldsymbol{H}_1(f)$ and $\boldsymbol{H}_2(f)$. Now for a fixed frequency f_0, the complex component of the FIR filters $\boldsymbol{H}_{1/2(f_0)} = H_{1/2,f_0}$ at the corresponding frequency can be multiplied with the belonging pressure field and the resulting pressure field $p'(f_0)$ containing the achieved reductions can be calculated:

$$p'_{\mathrm{S1}}(f=f_0,x,z) = p_{\mathrm{S1}}(f=f_0,x,z)\cdot H_{1,f_0}\,, \tag{42}$$

$$p'_{\mathrm{S2}}(f=f_0,x,z) = p_{\mathrm{S2}}(f=f_0,x,z)\cdot H_{2,f_0}\,, \tag{43}$$

$$p'(f=f_0,x,z) = p_{\mathrm{P}}(f=f_0,x,z) + p'_{\mathrm{S1}}(f=f_0,x,z) + p'_{\mathrm{S2}}(f_0,x,z)\,. \tag{44}$$

To compare absorption levels between different setups the relative absorption field Δp is calculated according to

$$\Delta p(f) = \frac{p'(f)}{p_{\mathrm{P}}(f)}\,. \tag{45}$$

The dependency on x and y have been dropped to increase readability. As the frequency resolution of the FIR filters depends on the length of the filter, the exact frequency f might not be defined. In this case the value for the closest match is chosen for the display. A set of some absorption fields after performing the LMS and multiplying with the corresponding complex FIR filter coefficient can be seen in Fig. 19. The figure shows twelve different plots for six different solutions in the xz-plane. Microphone positions are marked by *circles* and line source positions by *squares*, except for the primary source, which is located at zero in all cases. Each of the six solutions is displayed in two plots arranged on top of each other ((a) and (d), (b) and (e), (c) and (f), ...), one for the lower end of the frequency range (80 Hz) and one for a high frequency of the range (630 Hz).

Some dimensions are shared between all solutions: the distance d_1 between S1 and S2 (0.15 m) and the positioning of the Reference Microphone, $m_1 = 1.45$ m. Those two quantities have little

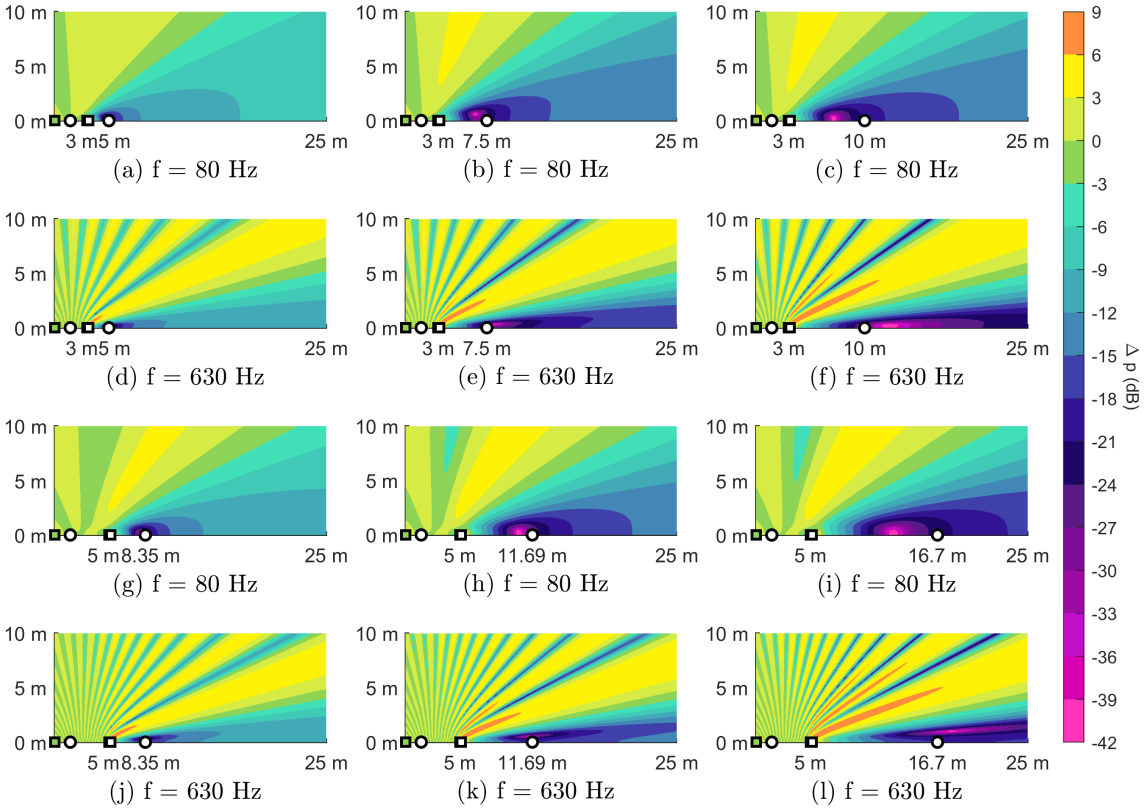

Figure 19: Comparison of relative absorption fields in the xz-plane for variations of r_1, r_2 and m_2 for a low and a high frequency. P positioned at $x = 0$ (green square), Ref. Mic. positioned at $m_1 = 1.45$ m. Position of S1 and S2 marked by a □ , Ref. and Err. Mic by a ◯.

influence on the emerging absorption pattern, except of course that d_1 determines the upper frequency limit. The other dimensions are varied to illustrate their effect on the resulting reduction.

The first and second row ((a) to (f)) share the same positioning of S1 and S2 at 3 m and 3.15 m respectively, whereas in the other two rows ((g) to (l)) S1 and S2 are positioned at 5 m and 5.15 m. The position of the Error Microphone m_2 varies over the columns, with the shortest distance on the left hand and the farthest on the right hand column. Note that the positions of the Error Microphones in graphs (a) to (f) have the same relative distance to the secondary sources and the primary source as graphs (g) to (l). Therefore, (g) is a scaled up version of (a), (h) is a scaled up version of (b) and so on.

All variations of distances create absorption patterns that share the same characteristics. The upstream area between the primary and secondary sources is mostly unaffected by reduction effects. The color scheme only reveals that those reductions are between ±3 dB, but looking at the data more closely reveals that the deviation fluctuates closely around 0 dB. In all cases a "shadow area" is created in the downstream section, ranging between a few dB of reduction to very strong, but highly localised reductions of 30 dB and more. It is quite clear that both the positioning of S1/S2 and the relative and absolute distance to the Error microphone have a role in determining the resulting absorption pattern. In general it can be said that with bigger distances the intensity and size of the absorbing "shadow" increases. However, the overall reduction values are reduced in comparison to the duct, where reductions of 40 dB and more where (at least in theory) easily

achievable. Apparently, this is not the case any more for waves of higher dimensions.

A new effect that could not manifest for plane waves can now be observed; an interference pattern forms above the shadow pattern, which becomes more visible with increasing frequencies. It seems that some of the energy is "reflected upwards" as Δp surpasses additional 6 dB and even 9 dB in some areas. Just as the resulting reduction in the shadow area intensifies with increased distances, so does the interference pattern intensify. This third area lies outside the controlled area of the LMS algorithm and is therefore not optimised by it. It is a logical side effect of geometrical interference of the emitted waves.

Evaluating those graphs (and additional simulation results not presented here), a generalisation of how the active absorption affects the sound field in the x-z plane is visualised in Fig. 20. It is *not* the goal to give more quantitative values for $\varphi_1(f)$ and $\varphi_2(f)$, but only to state in general that they seem to be frequency dependent. Now that the effect of cylindrical waves on active absorption

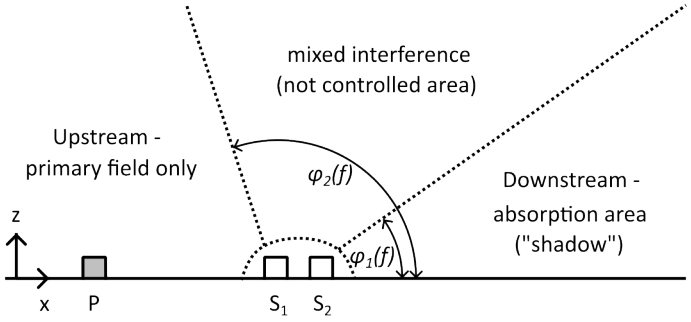

Figure 20: Qualitative categorisation of sound areas created by active absorption in the xz-plane.

has been described in general terms, it is time to move on to discrete line sources (line arrays), seen in Fig. 18b. Such a discrete line source would now be made up of point sources which emit spherical waves. Such a spherical wave can be described by

$$p(r,k) = A\,\frac{\mathrm{e}^{j(-kx)}}{r}\,r \tag{46}$$

where A is again the source strength q, possibly combined with a unit conversion, but again it is set to 2. The goal is of course to describe the cylindrical wave with sufficient superimpositions of spherical waves.

Two questions come immediately to mind: how does the number of sources n per array and the distance between sources d_2 influence the results? First the emitted field of only one line array will be looked at to judge how to set n and d_2 to imitate the behaviour of a cylindrical wave. In Fig. 21 the emitting fields for four different line arrays are depicted at a frequency of 250 Hz in the xy-plane, to emphasize the (in)dependence of the y coordinate. It is quite obvious that at least two sources per wavelength must be placed, but it was observed that increasing the density of sources per wavelength further does not improve the results significantly. Rather than varying d_2 (which is here set to $d_2 = 0.62$ m), the total number n and therefore the length of the array was increased. The shorter arrays of only 10 and 20 sources (Fig. 21a and Fig. 21b) are not able to recreate a pattern similar to that of a cylindrical wave. But once the array reaches 50 sources (Fig. 21b), the expected pattern of the Hankel wave can already be surmised. The expected pattern would show a decay of 3 dB for every doubling of the distance, which here is marked by dotted lines in all four plots. For n =500 there is virtually no difference anymore. But no matter how many sources are used: the resulting field resembles cylindrical waves best in the center of the array, with strong deviations in the far distance (x-direction) and to the edge of the array (y-direction).

It is the *dimension* of the array *in relation to the wave length* that should be as big as possible and one should stay in the center of the field to imitate cylindrical waves. Now again the LMS

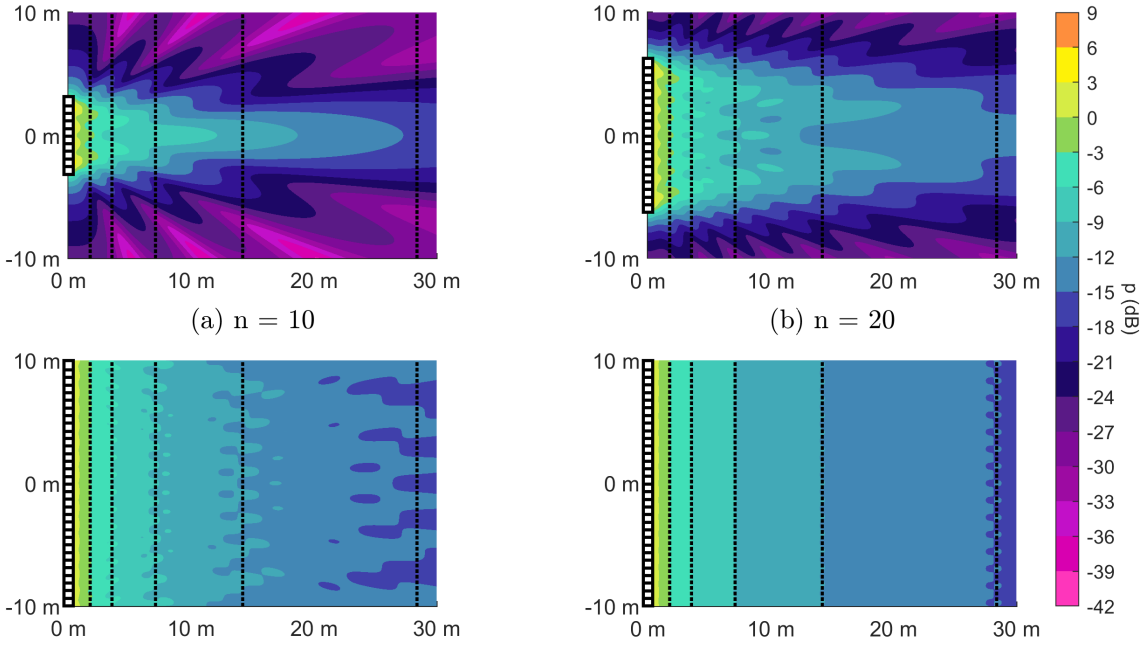

(a) n = 10 (b) n = 20 (c) n = 50 (d) n = 500

Figure 21: Comparing discrete line arrays to see if the emitted field behaves like that of a cylindrical wave. View on the xy-plane, ($z = 0$) with varying source numbers n, source marked with a □. $d_2 = 0.62$ m and $f = 250$ Hz. Dotted line indicates doubling of distance.

will be performed with $n = 50$ sources per array to compare it to that of the 2D solution. It will be compared against the solution shown in Fig. 19i and Fig. 19l. But first the impulse responses

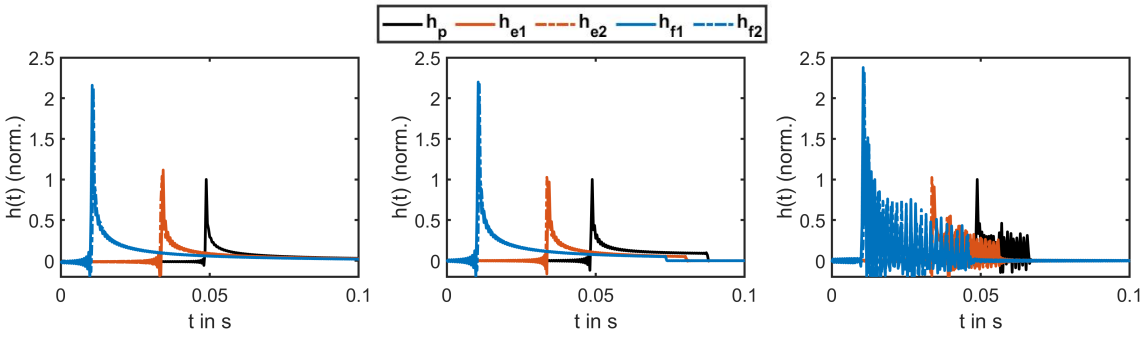

(a) Continuous line source. (b) Discrete line array, $n = 500$, $d_2 = 0.1$ m. (c) Discrete line array, $n = 50$, $d_2 = 0.62$ m.

Figure 22: Impulse responses of the line source vs. line arrays, sampled at $f_s = 2560$ Hz. All impulse responses normalised so that the peak of $\mathrm{h_p} = 1$.

of the line source and that of the discrete line arrays will quickly be compared. Fig. 22 shows the (normalised) impulse responses for the continuous line source (a), that for a discrete array with big n and small d_2 (b) and that for the discrete line array that will be used for the LMS (c) further down. If the distance d_2 between sources in comparison to the sampling frequency f_s allows for

spacial aliasing (f_s is still set at 2.56 kHz), the impulse responses stop looking like that of the continuous line source (like in (b)), but instead they look "messy", as the individual sources don't blend nicely together in the responses (like in (c)). Running the LMS method a few times for different variations of that parameters reveals that the solutions converges quicker and to a better solution with a smooth impulse response, but it will in most cases also find a (slightly worse) solution for not so smooth impulse responses as well. Fig. 23 shows the by now already familiar

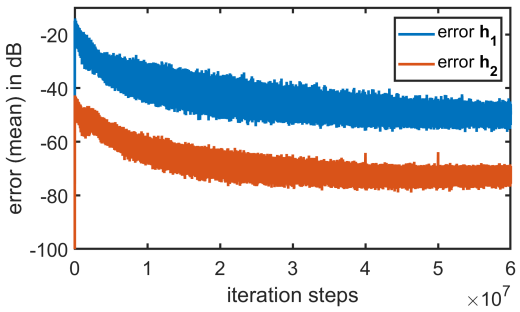

(a) Error progression over iteration steps, moving average applied.

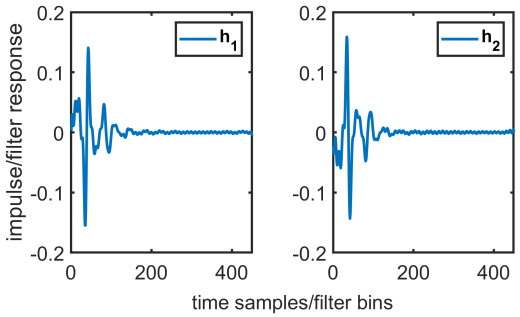

(b) Estimated FIR filters.

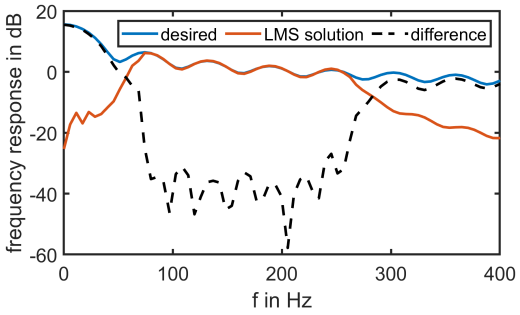

(c) Estimated frequency response of the downstream path and relative error.

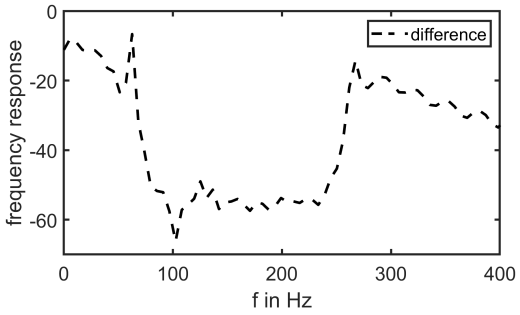

(d) Relative error of the estimated frequency response of the upstream path.

Figure 23: LMS results of the discrete line array with $n = 50$ sources and a distance $d_2 = 0.62$ m. $\alpha_1 = 1 \cdot 10^{-5}, \alpha_2 = 7 \cdot \alpha_1$, 80 Hz - 250 Hz after $6 \cdot 10^7$ iterations.

plots to illustrate the LMS results, which was applied between 80 Hz and 250 Hz. For the given setup the method is converging quite slowly and it was stopped after $6 \cdot 10^7$ iterations. When comparing this to the error plot for the system belonging to the impulse response of Fig. 22b in Fig. 56a in Apx. B, it becomes clear that the spacing of sources might greatly affect the speed of convergence. The down- and upstream path (Fig. 23c and Fig. 23d) look very comparable to the achieved reductions for the theoretical duct (see Fig. 9) and promise good results. Fig. 24 shows the spacial absorption Δp for 80 Hz and 250 Hz, now also in top down view to assess the dependency of the y coordinate. The pattern looks similar to that of the continuous line source, but the differences due to discretisation are quite clear. In the not controlled area above the "shadow" (Fig. 24a and Fig. 24c) the interference effects are more pronounced than with the line source. Also the reduction downstream is more localised and focuses mostly on the error microphone, especially for lower frequencies. This also becomes clear when looking at the top-down view (Fig. 24b and Fig. 24d). As expected, the resulting spacial absorption Δp for the line arrays with $n = 500$ sources per array, seen below in Fig. 25 lies somewhere between the observations for $n = 50$ and the continuous line source.

But even though the achieved spacial reduction is less homogeneous, the reduction values itself are

not that bad. Most areas behind the Error Microphone show reductions between -6 dB and -15 dB, but locally reductions below -20 dB up to more than -40 dB are reached. Again, the size of those highly reductive areas seems to increase with the number of sources in the array. Also the size of the shadow area would make the perception of that reduction easily possible, as it reaches far higher than two metres. A person could walk away from the secondary sources and would very quickly be completely covered in the reduction zone.

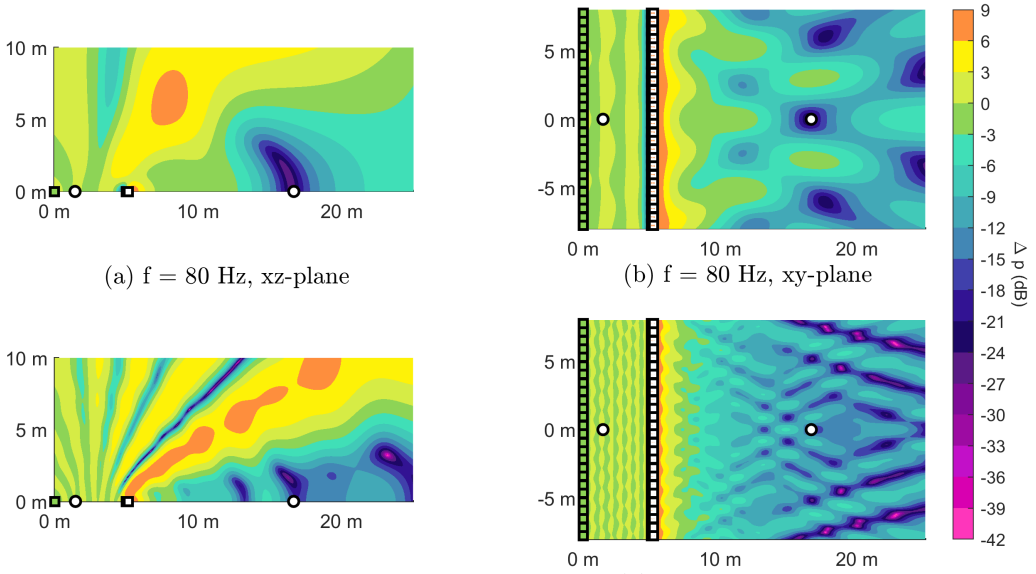

(a) f = 80 Hz, xz-plane

(b) f = 80 Hz, xy-plane

(c) f = 250 Hz, xz-plane

(d) f = 250 Hz, xy-plane

Figure 24: The spacial absorption for $n = 50$ sources per array, presented for two frequencies with side (xz-plane) and top (xy-plane) view each.

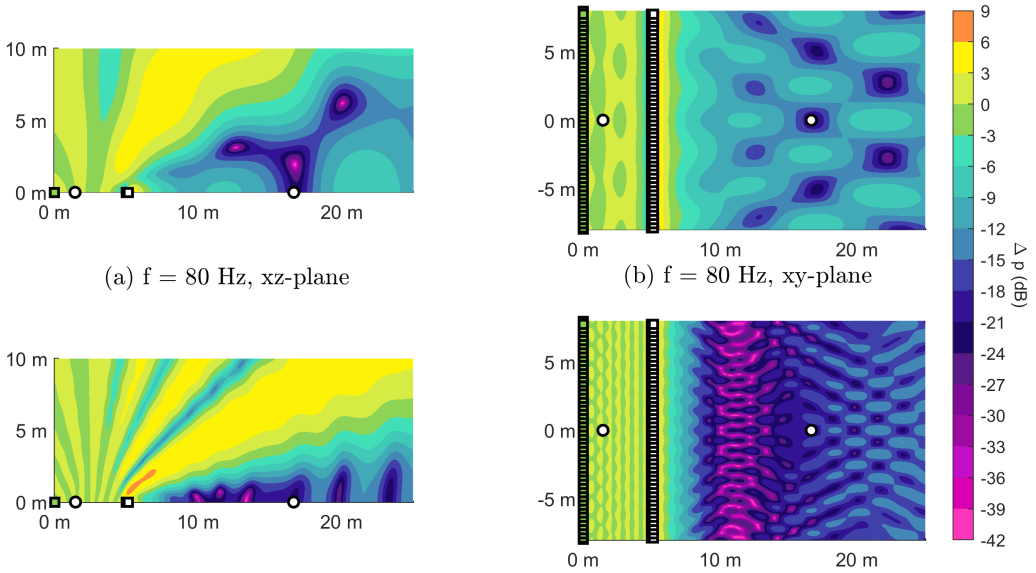

(a) f = 80 Hz, xz-plane

(b) f = 80 Hz, xy-plane

(c) f = 250 Hz, xz-plane

(d) f = 250 Hz, xy-plane

Figure 25: The spacial absorption for $n = 500$ sources per array, of solution shown in Fig. 56, presented for two frequencies with side (xz-plane) and top (xy-plane) view each.

2.6. Active Absorption of spherical waves with curved arrays

The last logical step to even further extend the application possibilities of active absorption is to deal exclusively with spherical (three dimensional) waves. The mathematical expression for a spherical wave was given in Eq. (46) in the previous section. There it is shown how to replace a continuous line source with a discrete array made up of point sources, but the goal was to (at least to a certain extent) mimic the behaviour of a line source to investigate cylindrical (2d) waves. The logical conclusion is to consider waves emanating from a point source. The form of this "3d wave", a spherical wave, gives rise to the idea to "curve" the secondary sources along (part of) the wave front, therefore the title of the section. This forms two absorbing arrays in the form of circles, or in case of only partial coverage, two semi-circular absorbing arrays. This idea is not well explored yet and it is unclear whether it will lead to usable results or not.

At first the primary point source P shall be enclosed by two rings of secondary sources, the inner ring being the array S1 and the outer array being the array S2, with n sources each. This way a radial symmetry is created, which technically reduces the problem again to two dimensions, but in relation to the polar coordinates. The scheme for this is seen in Fig. 26. The Reference and the Error Microphone are again placed in a single line, with the Reference Microphone in the upstream region (inside the arrays) and the Error Microphone in the downstream region (everything outside the arrays).

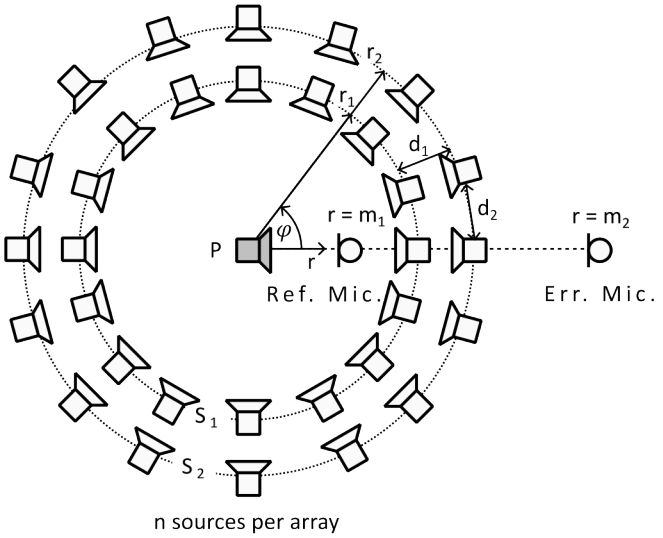

Figure 26: Scheme for the radial absorption of a point source, discrete full circle arrays.

The radius to the inner source circle is marked as r_1, the to the outer circle is marked r_2. Now the distance d_2 marks the straight connection between two sources on the outer circle (as the distances here are bigger than on the inner circle), although it can be assumed that the arc b, $b = \varphi \cdot r$ and the straight connection have approximately the same length. d_2 is again limiting the higher end of the frequency range, as two sources per wavelength should be set. But, as a consequence of the geometry, there is also a *newly imposed* limit for the higher end of the frequency range, which might be overlooked at first. Its influence, however, becomes quite clear when one starts to try to find a solution with the LMS method.

The distance d_1 is the incontrovertible factor which determines the higher end of the frequency range, as an infinite amplitude would be needed to cancel the incoming wave if the distance between the secondary sources is that half of that wavelength (this is illustrated in Fig. 2). But

since the circle is now closed, the sound emerging from the *opposite* secondary sources must also be absorbed[11]. Therefore, frequencies with a wavelength of $2 \cdot r_2/2$ and $(r_1 + r_2)/2$ would also need infinite energy to be absorbed. To give an example, if the distance r_1 is again set to 5 m and r_2 to 5.15 m, the upper frequency limit would be around 17 Hz. As this is far below the working frequency range of most loudspeakers, one could try to raise the frequency range above that, but of course every multiple of that frequency which is included in the working frequency range will cause the LMS to become unstable. This makes this geometric structure effectively useless for a practical application.

Nevertheless, an attempt was made to present a solution for the circle. To give an idea of how the absorption pattern would look like *if* a working solution was found, the LMS is stopped *before* the error is diverging to infinity[12]. With the help of the relative error of the downstream path estimation, two frequencies were identified were the spacial absorption was quite good already. The side view of the relative spacial reduction Δp is seen in Fig. 27. Here the cross-sectional area along the microphones was selected, but that decision is quite arbitrary as the solution is radially symmetric. This view of the spacial reduction gives the impression that the approach itself is quite

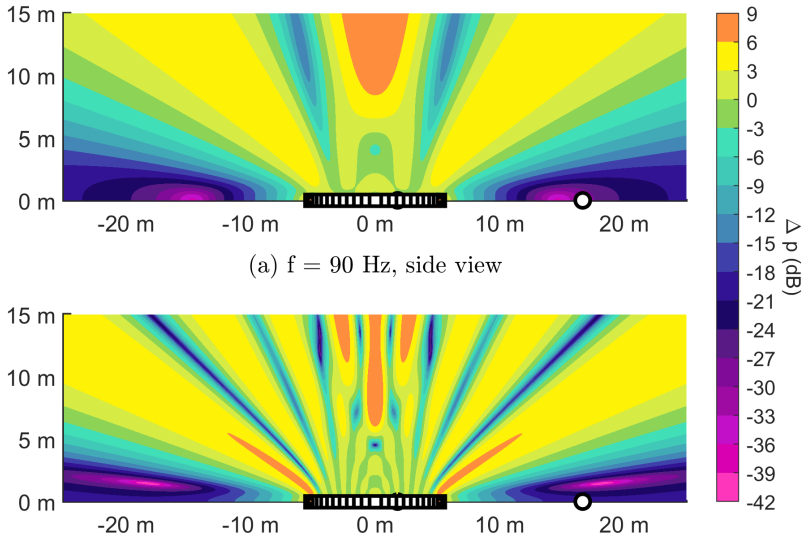

(a) f = 90 Hz, side view

(b) f =242 Hz, side view

Figure 27: The spacial relative absorption of the full circle array setup, demonstrated for a low and a high frequency inside the frequency range were good results are achieved.

promising, just the problem with the incident waves of the opposite side must be solved. The easiest way to achieve this it to modify the setup to simply not include an opposite side. This modified setup can be seen in Fig. 28.

A newly introduced dimension is the array length l, which only serves as an auxiliary parameter for estimating the resulting dimensions. The following is a brief example with similar dimensions to the example shown at the end of last section. Therefor r_1 is again set to 5 m, d_1 to 0.4 m, m_1 to 1.45 m and m_2 to 16.67 m. Each array has $n = 25$ sources with an array length l of 10 m. This

[11] This is the case as the upstream cancellation is never perfect.

[12] As was briefly mentioned in Sec. 2.3, the LMS method is a gradient based method and therefore always fixes "the strongest error" first. Technically the method can be stopped at any iteration step, but usually it only makes sense to use as many steps as are needed for the solution to converge. However, if the method is stopped *before* the gradient identifies one of the unsolvable frequencies as the "biggest problem" a solution can still be found, which is (unsurprisingly) very badly, if at all, optimised. Therefore, this approach is only used to illustrate a point.

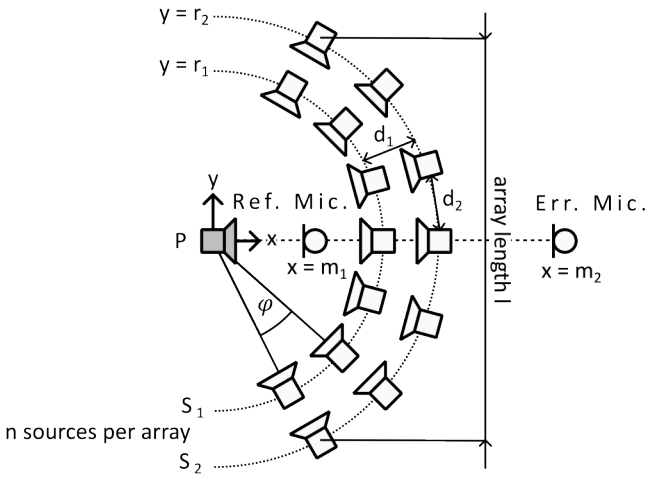

Figure 28: Scheme for the radial absorption of a point source, discrete semi-circular arrays.

sets the upper frequency end to about 300 Hz. The impulse responses for this setup are shown in Fig. 29b, with the impulse responses of the full circle for comparison in Fig. 29a.

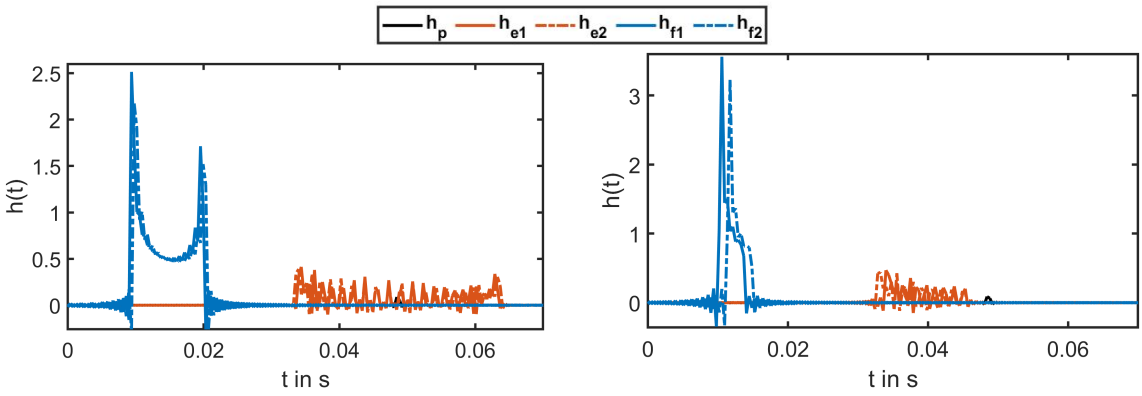

(a) Impulse responses for the full circle, $n = 52$ sources per curved array.

(b) Impulse responses for the half circle, $n = 25$ sources per curved array.

Just as predicted, without the incoming wavefronts from the other side of the array, the LMS now converges without a problem. The down- and upstream PSD graphs are depicted in Fig. 30. The presented setup is able to create up to -40 dB of active reduction, with an average of -36 dB across the frequency spectrum.

Two frequencies are picked to demonstrate the resulting pattern, one from the low end (80 Hz) and one close to the higher end (250 Hz), which are the same frequencies that were used in the examples in the previous section. The resulting active reduction pattern Δp for both the xz-plane and the xy-plane are shown in Fig. 31.

When comparing the absorption pattern with that of the (discrete) line array, many similarities become apparent. The reduction field can again be split in three regions: The Upstream area, the Downstream area and the mixed interference area. One difference that becomes apparent for the mixed interference area seemingly has more "intense" interferences even at in comparison lower frequencies. Nevertheless, the qualitative categorisation of the areas depicted in Fig. 20 can also be applied for the curved array. Interestingly, although much less sources are used than in the

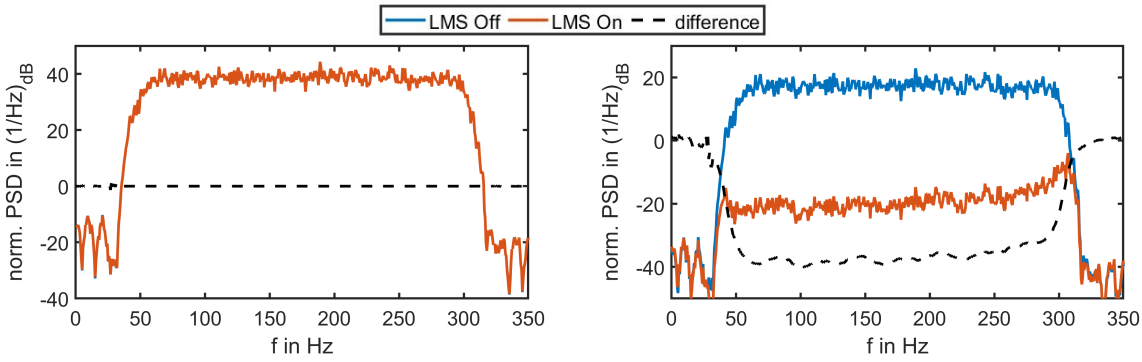

(a) Upstream.

(b) Downstream.

Figure 30: Normalised PSD graphs from the LMS results of the curved array with $n = 25$ sources and a distance $d_2 = 0.53$ m. $\alpha_1 = 1 \cdot 10^{-5}, \alpha_2 = 7 \cdot \alpha_1$, 50 Hz - 300 Hz after $3.5 \cdot 10^7$ iterations.

examples given in Fig. 24 and Fig. 25, the spacial absorption seems to be just as good, if not better. At $f = 80$ Hz, only one big "blob" of very high reduction is formed, reducing the pressure field up to astounding -51 dB. On the ground surrounding the Error Microphone (xy-plane), an area with the rough dimensions 6 m x 8 m where the absorption is always below -15 dB, when drawing a smaller square of 2 m x 2 m, it even stays below -25 dB close to the ground. That high reduction sphere is also significantly tall, at 1.8 m the absorption is still mostly below -25 dB if that 2m x 2m square is extended to a cuboid of that height. Of course the biggest shortcoming is the localisation of that high intensity reduction at that frequency, only consistently reducing by more than -9 dB behind the 12 m mark on the x-axis. At $f = 250$ Hz the reduction pattern has changed quite a lot, instead of one concentrated reduction area a lot of slim "rays" of high reduction that spread out from the center. In those areas reductions up to -49 dB are achieved. The widespread reduction is also better, reaching consistenlty at least -12 dB of reduction behind the 12 m mark on the x-axis (directly above ground). When this is compared against the solution of the discrete line array with similar dimensions and number of sources (seen in Fig. 24) it is clear that the curved array setup to absorb the incoming sound of a point wave can potentially reach much better results.

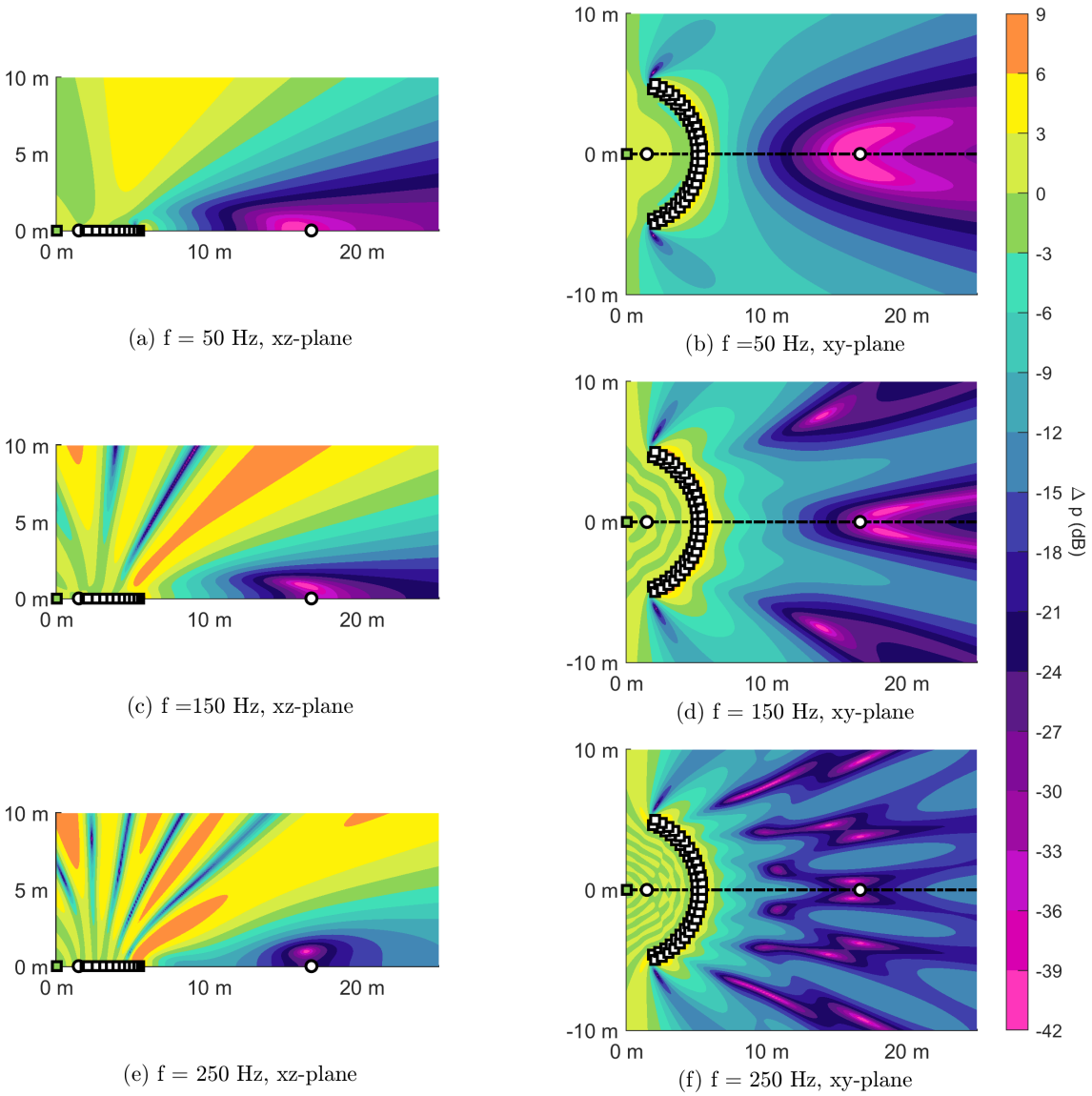

(a) f = 50 Hz, xz-plane

(b) f =50 Hz, xy-plane

(c) f =150 Hz, xz-plane

(d) f = 150 Hz, xy-plane

(e) f = 250 Hz, xz-plane

(f) f = 250 Hz, xy-plane

Figure 31: The spacial relative absorption of the curved array setup.

3. Measurement Setup

Two setups will be presented: one for the discrete line array and one for the curved array. The aim is to confirm or refute the absorption concepts presented with measurement data. After finding suitable test environments, the goal was to find optimised setups for both tests while maintaining feasibility and taking into account the individual challenges of the test environments. The experiment focusing on the discrete line array (from now on referred to as "Setup 1") was performed on the ground of the Chalmers University of Technology between two buildings with highly reflecting walls. The experiment focusing on the curved line array ("Setup 2") was performed inside a semi-anechoic Chamber of Volvo Cars, north of Gothenburg.

Both experiments follow the same procedure; first the impulse responses are obtained using the H_1 estimation, with a white noise signal with long duration as input signal. The sources in the respective arrays are all fed with the signal simultaneously, effectively treating them as one source (comp. to Fig. 32). After evaluating the impulse responses and their decay rate, the filter length for the LMS method will be set and the impulse responses are cut to length. The guidelines explained in Sec. 2.4.1 will mostly be followed to find converging solutions. With the help of the now obtained filters $\boldsymbol{h}_1$ and $\boldsymbol{h}_2$, the signals to feed into the secondary sources are created. As input signal for the active LMS a white noise signal, band-passed within the frequency range is used. The attenuation effects are recorded by the Reference Microphone, the Error Microphone and several additional verification microphones. The positions of the verification microphones will be determined with the help of simulating the setup beforehand. All measurements will again be performed at a sampling frequency of 2.56 kHz, which makes additional up- and down-sampling of the signals necessary. This time no physical low-pass filter is integrated, instead a digital low-pass filter is applied. A list of all equipment used for both Setup 1 and Setup 2 is found below in Tab. 3.

	Name	Specification
Interface	Orion Antelope 32 (Gen 1)	32-channel A/D-D/A Converter
Microphone(s)	Superlux ECM-999	Free Field Microphone, frequency range between 20 Hz - 20 kHz
Source(s)	Genelec 8020D	Frequency Response between 56 Hz - 25 kHz ("-6dB"), SPL = 100 dB

Table 3: List of equipment used for Setup 1 and Setup 2.

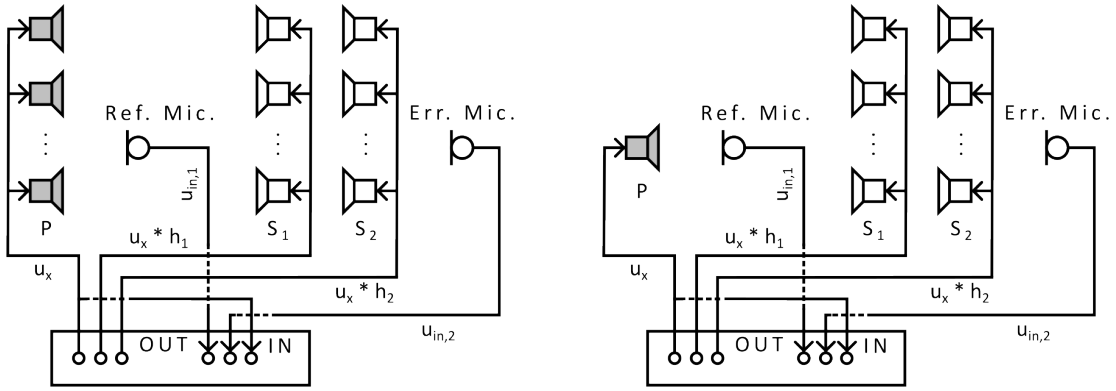

(a) Setup 1 (Line Array).

(b) Setup 2 (Curved Array).

Figure 32: Scheme of the signal flow for both setups. Convolution is performed offline, measurement microphones not depicted.

3.1. Discrete Line Array (Setup 1)

The biggest challenge for creating a setup for the discrete line array is to keep the number of sources to a feasible amount. As discussed in Sec. 2.5, the longer the array compared to the distance between individual sources, the better the behaviour of a cylindrical wave is imitated, which results in better reduction values downstream. Here the setup aims at reproducing a setup similar to that shown in Fig. 21c and Fig. 24 (around 50 sources for an array of 30 m length). But instead of using 50 or more physical sources for each array (150+ in total), a small amount of sources will be placed between two very reverberating and parallel walls (an "infinite hallway") so that the mirrored sources will add up to the length of the array. The setup including distances is drawn up in Fig. 33, the mirror sources are indicated by dotted lines. In comparison to the simulations performed in Sec. 2.5, the distance of d_1 was increased to 0.4 m, the reduce possible near field effects. The distance d_2 is determined by the width of the "hallway", which has five meters in width. A total number of 24 sources was used, which results in eight sources per array, therefore $d_2 = 0.625$ m. This results in an upper frequency limit of $f_{\text{up,theoretical}} = 274.4$ Hz. The upper limit of the LMS method was set to 95% of that, $f_{\text{up}} = 260$ Hz. It is important to place the arrays perpendicular to the walls and keep a distance of $d_2/2$ on both sides so that the mirror sources match up with the real sources. Photos of the setups can be seen in Fig. 34 and Fig. 35. As the positions of the sources have to be very precise, it was not possible to prevent some sources being covered by foliage (compare Fig. 35b), which might have a negative influence on the sound field[13].

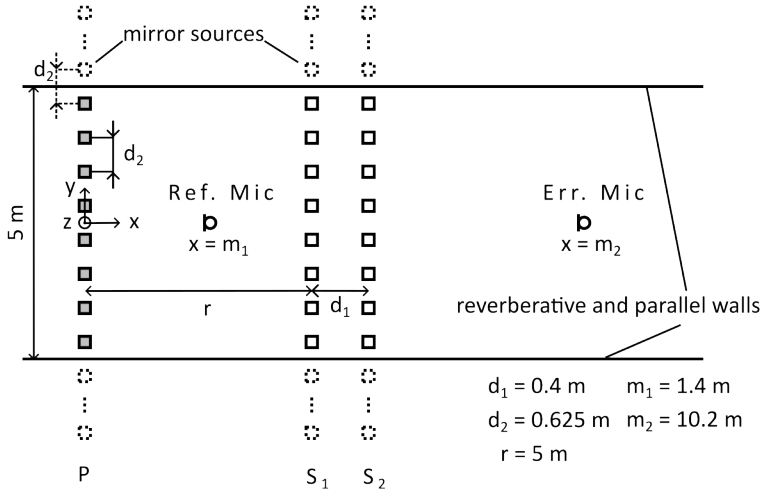

Figure 33: Setup 1 - Setup of the discrete line array. All coordinates of verification microphones listed in Tab. 4.

Indeed it was a major concern prior to the realisation that the speakers could not be positioned precisely enough to achieve the desired effect of extending the array through mirror sources. The available measuring devices and aids would be used as well as possible to achieve the most precise positioning, but the accuracy that can be achieved with just a measuring tape, duct tape and some strings cut to length is simply limited. This, in combination with the probably not perfectly reflective walls (seen in Fig. 34), led to the decision to limit the distance of the Error Microphone somewhat and place it at 10.2 metres, although the analysis in Sec. 2.5 made it clear that the results could probably be improved if it was placed closer to the 15 m mark.

[13] Also it was noticed too late that some wildlife had taken shelter in that foliage, see Fig. 59 in Apx. C

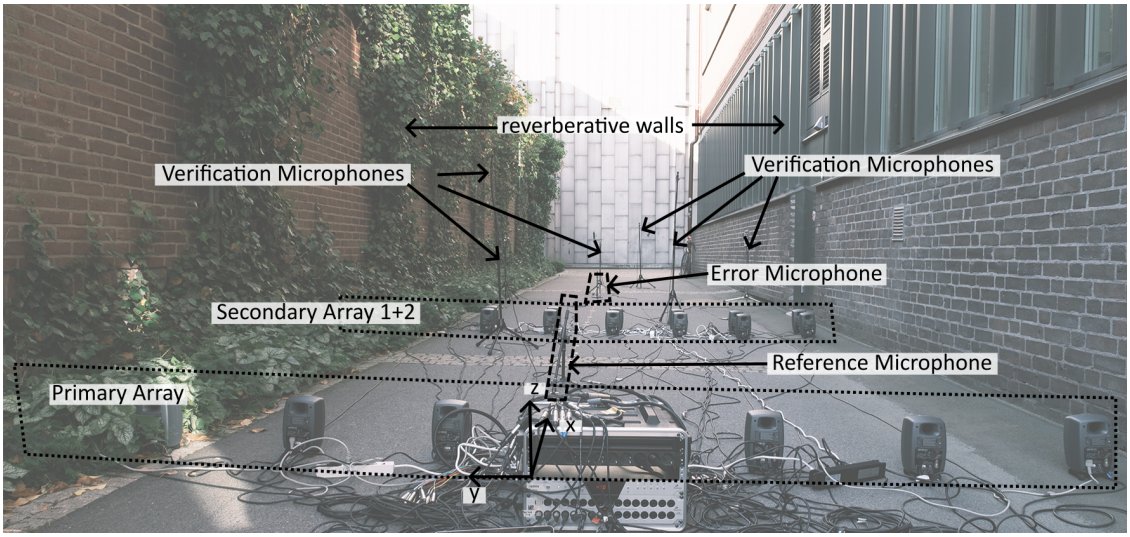

Figure 34: Setup 1 - Photo of the setup of the discrete line arrays.

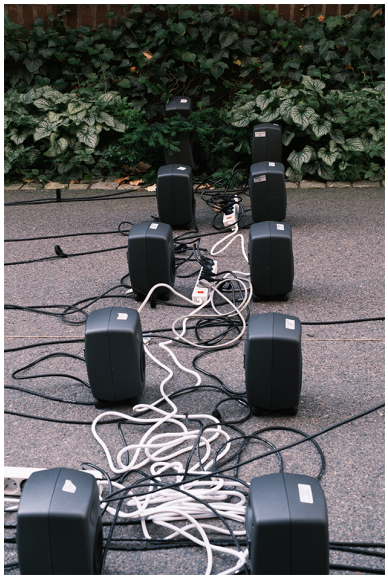

(a) Secondary Sources, close-up. The sources face the downstream direction.

(b) Foliage covering some sources.

Figure 35: Setup 1 - Additional photos of Setup 1.

A number of additional microphones was used to capture the reduction effects. They are placed across all three sound areas that are categorised above in Fig. 20. Three additional microphones are placed upstream, two are placed in the "mixed interference" area, and eleven are placed downstream. The coordinates and labels of all microphones are listed in Tab. 4. To further illustrate the verification positions, an isometric view with true scaling is given in Fig. 36. Originally more verification positions have been used, but a number of verifications had to be discarded due to application errors.

	x in m	y in m	z in m		x in m	y in m	z in m
Ref. Mic.	1.40	0.00	0.02	Mic. 1	1.24	1.95	0.03
Err. Mic.	10.20	0.00	0.02	Mic. 2	8.91	1.99	0.1
Mic A	3.50	0.60	1.60	Mic A'	2.35	1.07	0.80
Mic B	6.30	-1.00	1.70	Mic B'	5.88	0.70	1.72
Mic C	9.20	-2.30	0.40	Mic C'	9.04	-0.85	0.40
Mic D	9.70	1.40	0.75	Mic D'	8.22	0.22	0.92
Mic E	11.50	0.00	0.82	Mic E'	11.43	-1.93	1.10
Mic F	13.80	-0.80	1.30	Mic F'	13.0	-0.64	0.80

Table 4: All x, y and z coordinates of the Reference Microphone, Error Microphone and verification microphones for Setup 1. Isometric visualisation in Fig. 36.

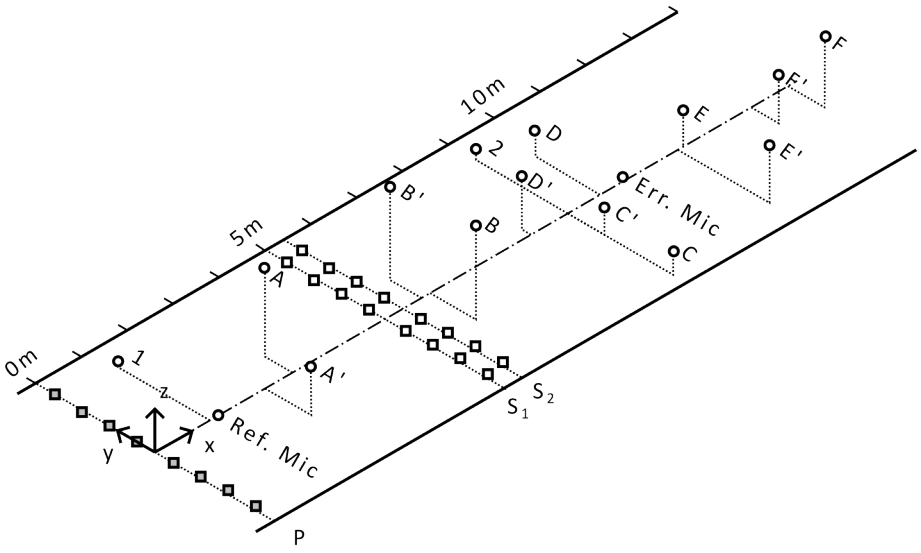

Figure 36: Setup 1 - Isometric view of the microphone positions, to scale.

To plan the microphone positions, a slightly modified simulation of the discrete line array was performed. It was assumed that the the sources would reflect at the walls at least three times, each time reflecting 90% of the incident sound. The simulation of this is shown in Fig. 37, which reveals that this approach should lead to very similar results as if exclusively physical sources were used. As mentioned further up, the Error Microphone was placed a bit closer to the Secondary Sources than in the example discussed in Sec. 2.5, due to technical limitations. The verification microphones downstream were equally distributed in front of and behind the Error Microphone at various heights to capture as much insight above the emerging reduction field as possible.

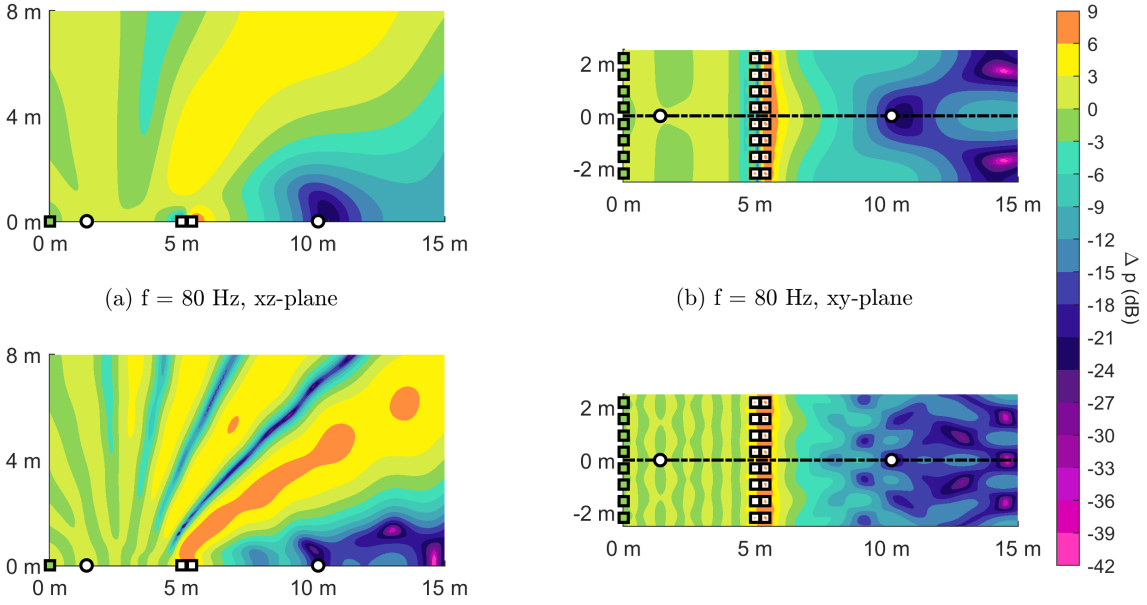

(a) f = 80 Hz, xz-plane

(b) f = 80 Hz, xy-plane

(c) f = 250 Hz, xz-plane

(d) f = 250 Hz, xy-plane

Figure 37: Simulation of Setup 1 where the wall reflects the arrays a total of three times, 90% of the amplitude gets reflected. Lowest and highest frequency of the solution displayed at the xy-plane and xz-plane.

3.2. Curved Array (Setup 2)

For testing the half circular array setup, a test environment with free field conditions needed to be found. Volvo Cars kindly offered there biggest semi-anechoic chamber that they usually use to measure the sound performance of their cars for this experiment. The setup was installed in the half of the chamber without the permanently installed wind channel, which left a space of approx. 11 m x 10 m of space. The dimensions of the setup and the positions of the Reference and Error Microphone were chosen accordingly. A total of 25 speakers was used, twelve for each array and one as the primary source. The setup is shown in Fig. 38, photos are shown in Fig. 40 and Fig. 41. The distance of the first secondary array was set to $r_1 = 4$ m, the second secondary array was set at $r_2 = 4.4$ m. The goal was to create a setup that used as much of the given space as possible, so the array length l was set to 8.5 m, resulting in an angle $\varphi = 0.238$ rad (13.64°) or an equivalent distance d_2 between the speakers of 1.05 m (d_2 is simply marked as d in the setup sketch). If this distance is considered to be the upper frequency bound, this results in $f_{\mathrm{up,theoretical}} = 164$ Hz, or if only 95% of that are used, $f_{\mathrm{up}} = 155$ Hz.

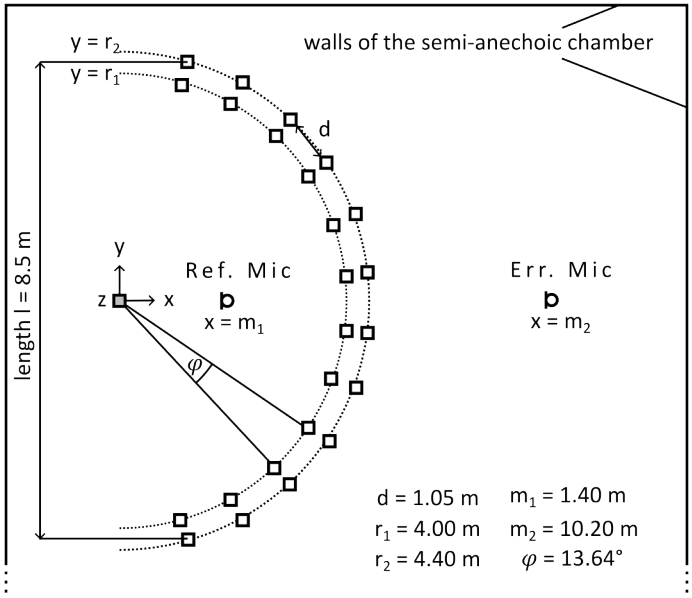

Figure 38: Setup 2 - Setup of the curved line array. All coordinates of verification microphones listed in Tab. 5.

This setup seems to leave a little more tolerance in accuracy of placement than the previous setup, as this time the sources do not have to match their mirror sources perfectly. However, this setup also places a high value on the precise positioning of all sources, as the potentially achievable reduction values are higher, as shown below.

Again a number of verification microphones was used to capture the active reduction effects. Their positioning across the three sound areas (Downstream, Upstream, Mixed Interference) is quite similar to that of the Line Array. Two additional microphone positions were placed upstream, two in the mixed interference area, and eight downstream. The coordinates of all verification microphones are given in Tab. 5 and an isometric view of their positioning in space is given in Fig. 39. The idea behind the positioning was to see if the achieved reduction was symmetric, an easily detectable property that was neglected when planning the verification positions for Setup 1. However, some microphone names and the corresponding positions are grayed out. Unfortunately, the measurement data for these positions had to be discarded due to a measurement error. Overall,

the execution of Setup 2 was characterized by execution errors, which unfortunately makes large parts of the measurement results unusable, but more on this in Sec. 4.2 and Sec. **??**.

	x in m	y in m	z in m		x in m	y in m	z in m
Ref. Mic.	1.80	0.00	0.02	-			
Err. Mic.	8.20	0.00	0.02	-			
Mic A	2.00	-1.80	1.60	Mic A'	2.00	1.80	1.60
Mic B	4.20	-2.65	1.60	Mic B'	4.20	2.65	-1.60
Mic C	6.15	2.55	0.50	Mic C'	6.15	-2.55	0.50
Mic D	8.35	4.50	1.90	Mic D'	8.35	-4.50	1.90
Mic E	8.30	1.00	0.40	Mic E'	8.30	-1.00	0.40
Mic F	8.65	-3.60	1.40	Mic F'	8.65	3.60	1.40

Table 5: All x, y and z coordinates of the Reference Microphone, Error Microphone and verification microphones for Setup 2. Greyed out positions ended up not being usable due to an application error. Isometric visualisation in Fig. 39.

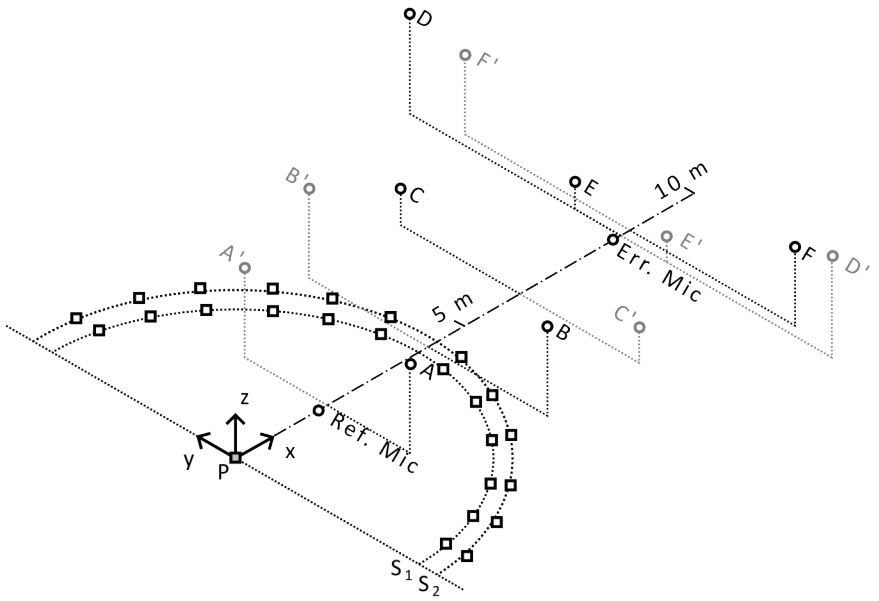

Figure 39: Setup 2 - Isometric view of the microphone positions, to scale. Greyed out positions ended up not being usable due to an application error.

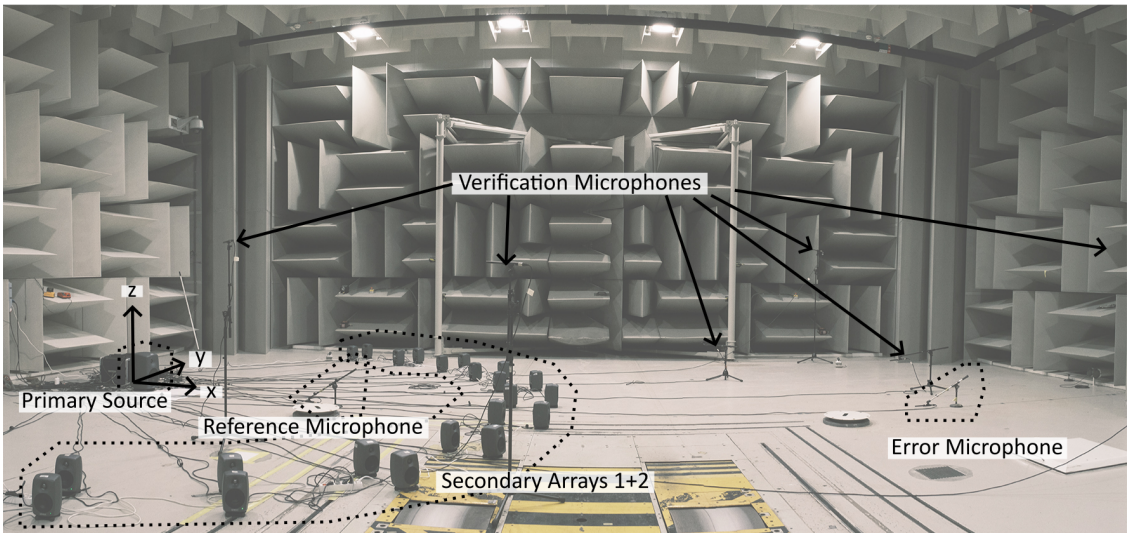

Figure 40: Setup 2 - Photo of the setup of the curved line arrays.

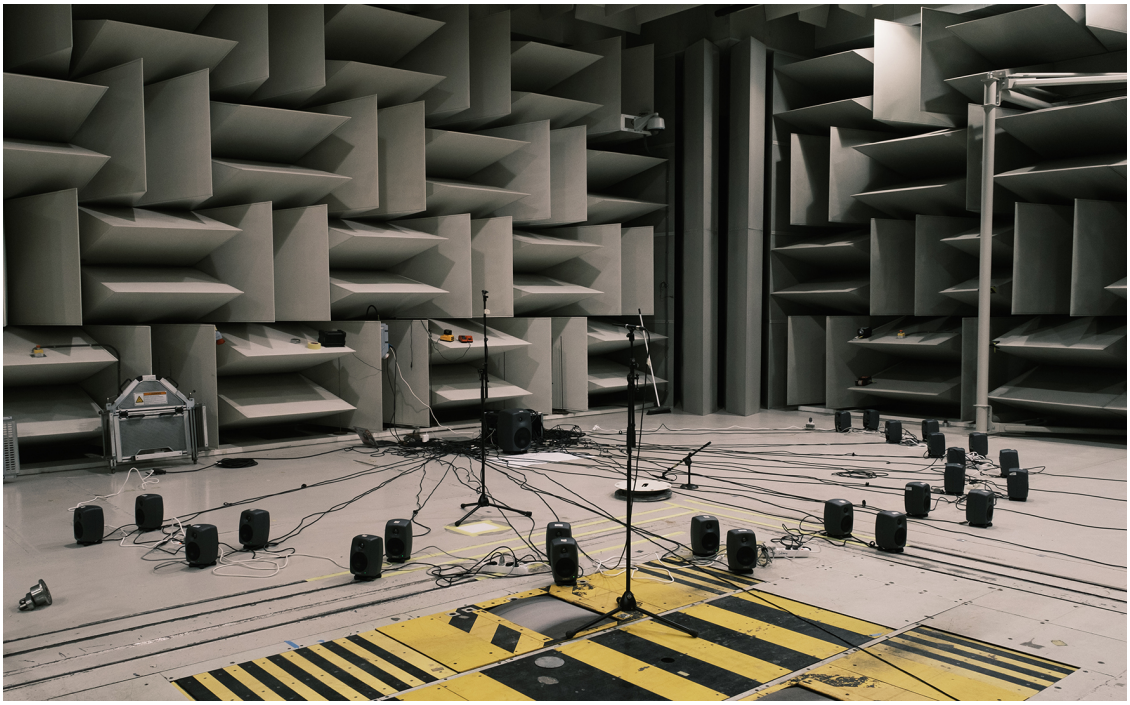

Figure 41: Setup 2 - Additional photograph of the secondary sources.

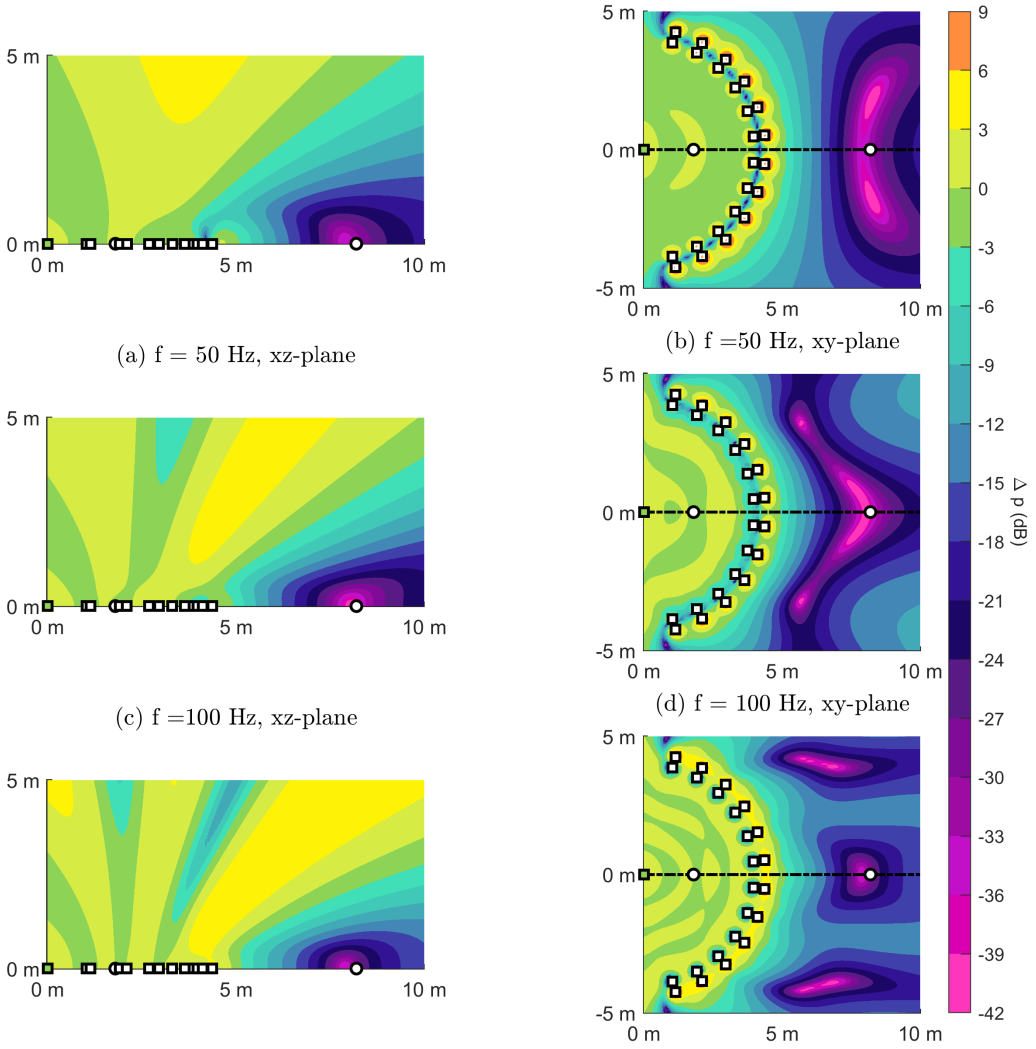

(a) f = 50 Hz, xz-plane

(b) f =50 Hz, xy-plane

(c) f =100 Hz, xz-plane

(d) f = 100 Hz, xy-plane

(e) f = 155 Hz, xz-plane

(f) f = 155 Hz, xy-plane

Figure 42: Simulation of Setup 2. Three frequencies (lowest, middle, highest) of the solution displayed, xy-plane and xz-plane.

To plan out the microphone positions, a new simulation of the semi-circular array was made. The top-down and side view surface plots for the highest and lowest frequency of the LMS range are portrayed in Fig. 42. Again, condensed spheres of very high local reduction are formed, which change form, size and position quickly with changing frequencies. For 50 Hz, local reduction values up to -57 dB are reached, for 155 Hz values up to -51 dB are reached. However, those spaces that reach those peak values only span one or two centimetres in each dimension. The indicated areas in pink (-42 dB or more) span one or two decimetres in each dimension, which might make it possible to record those, if the placement of the speakers and microphones are precise enough. [Note: add a comment about the three dimensionality of the absorption blob, maybe even in theory part]

4. Measurement Results

4.1. Results of Setup 1

Following the steps laid out in Sec. 3, the first step is to record the impulse responses, depicted in Fig. 43a to Fig. 43c. For this a white noise signal with length T =12 s was used as the input signal for the H_1 estimation (introduced in Sec. 2.1, Eq. (7)) with a windowing length of 2^{12} samples, resulting in nine blocks that are averaged over.

In Fig. 43d, which shows the decay of the impulse responses in dB, a small peak can be seen around 400 to 500 samples. Due to the setup, it was expected to see a reflection in the impulse response of a wall a few dozen meters behind the setup, which might be the cause of that slight increase. At first the impulse responses where cut shorter than this, to not include what is most likely an impurity, but the LMS algorithm has troubles converging with those given impulse responses. After some trial and error, the length of the impulse responses, and therefore the length of the FIR filters, was set to 960 samples, where all impulse responses have decayed more than 40 dB.

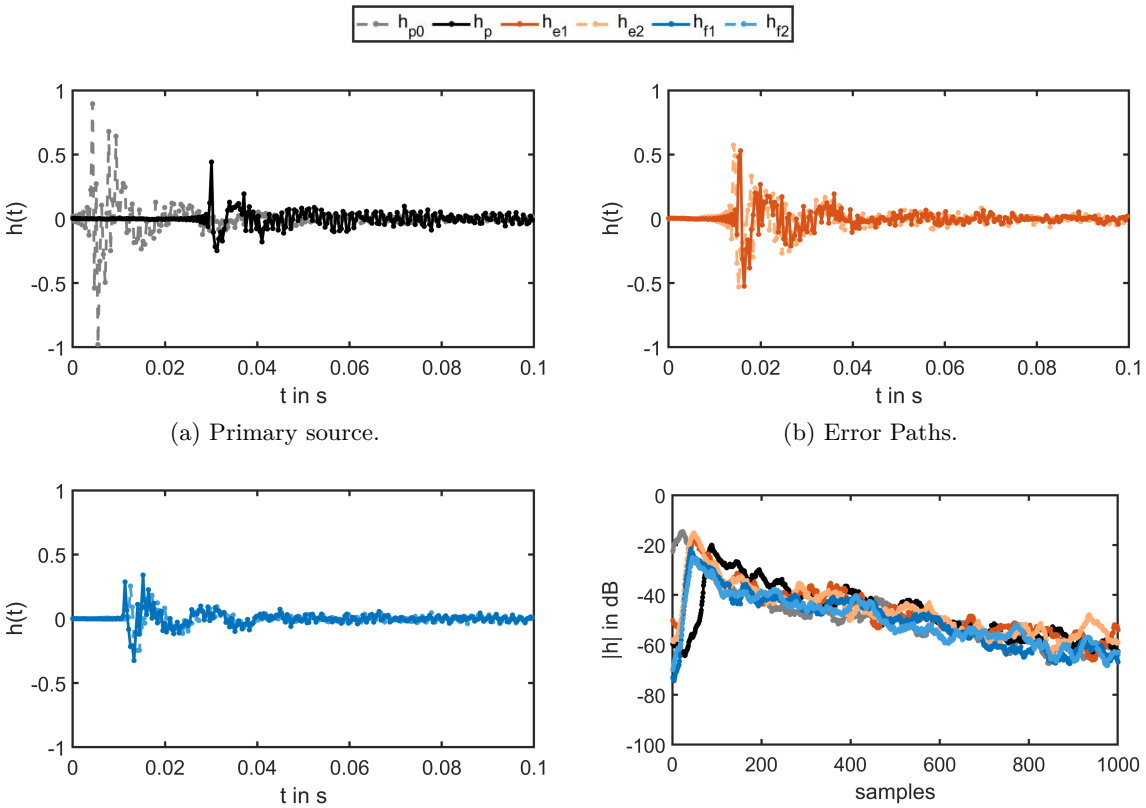

(a) Primary source.

(b) Error Paths.

(c) Feedback Paths.

(d) Decay of all IRs, moving average (25 samples) applied.

Figure 43: Measured impulse responses for Setup 1.

Despite the recommendations given in Sec. 2.4.1, the lower end of the frequency range for the FIR filters was set to 50 Hz (effectively the lower working end of the loudspeakers), therefore the FIR filters have a working range between 50 Hz - 260 Hz. This leads to the quite fluctuating but still converging error progression seen in Fig. 44a. The FIR filters seen in Fig. 44b have not quite subsided even after almost 1000 samples. As the data are now also to be analysed quantitatively,

some characteristic values for the down- and upstream PSD graphs (seen in Fig. 44c and Fig. 44d) are summarised in Tab. 6.

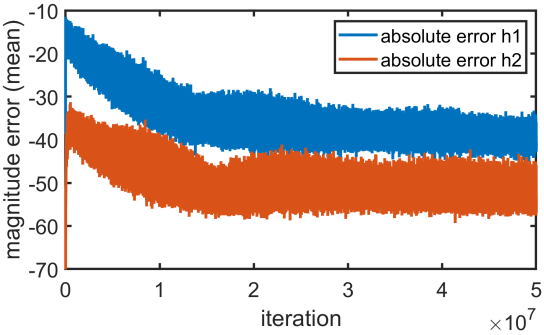

(a) Error progression over iterations, moving average applied.

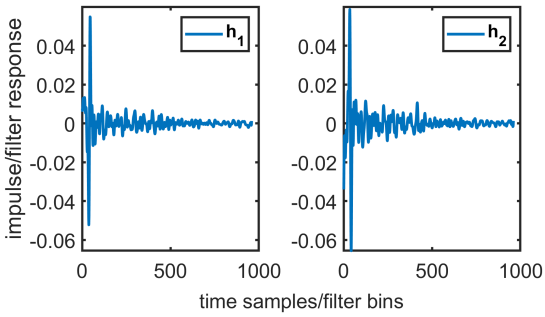

(b) FIR filters.

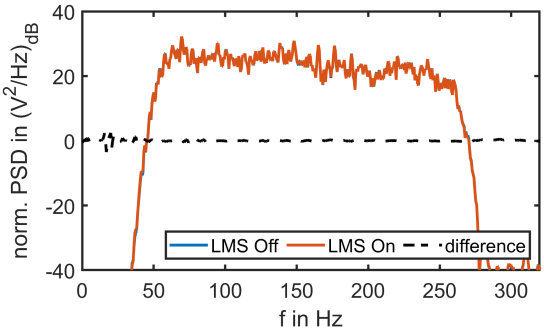

(c) Upstream estimated PSD with relative error.

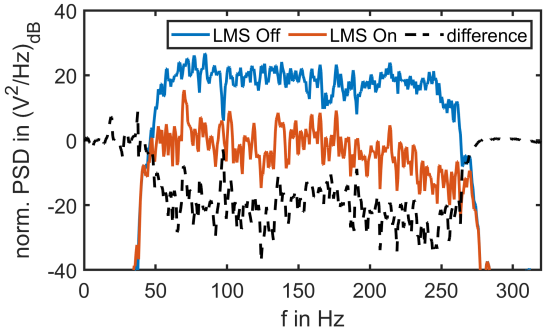

(d) Downstream estimated PSD with relative reduction.

Figure 44: Results of the LMS for $\alpha_1 = 5 \cdot 10^{-7}$, $\alpha_2 = 7 \cdot \alpha_1$, filter length $N = 960$, between 50 Hz - 260 Hz, after $5 \cdot 10^7$ iterations. Reduction values listed in Tab. 6.

	∅ reduction (dB)	max./min. reduction (dB)	max./min. reduction at f_{max}/f_{min} (Hz)	AAD (dB)
Ref. Mic.	-0.02	0.42 / -0.60	75 / 74	0.10
Err. Mic.	-20.73	-37.61 / -2.53	124 / 98	4.48

Table 6: Estimated active absorption for Reference and Error Microphone as a result of the LMS method for Setup 1. Average reduction in dB, maximal and minimal reduction in dB with corresponding frequency and AAD in dB. Corresponding graphs: Fig. 44c and Fig. 44d.

Now the found FIR filters (seen in Fig. 44b) are convolved with a white noise signal that is first band-passed within the frequency range and fed into the speakers according to the signal plan previously seen in Fig. 32a. This signal is recorded at all microphone positions and referenced to in plots as "LMS on". Additionally, a white noise signal (which for some measurements was also band-passed) is fed into the primary line array only, serving as a reference signal ("LMS off").

A good qualitative indicator if the signals are fed correctly into the system for the active reduction is the coherence (also introduced in Sec. 2.1, Eq. (8)). Those can of course be evaluated for all

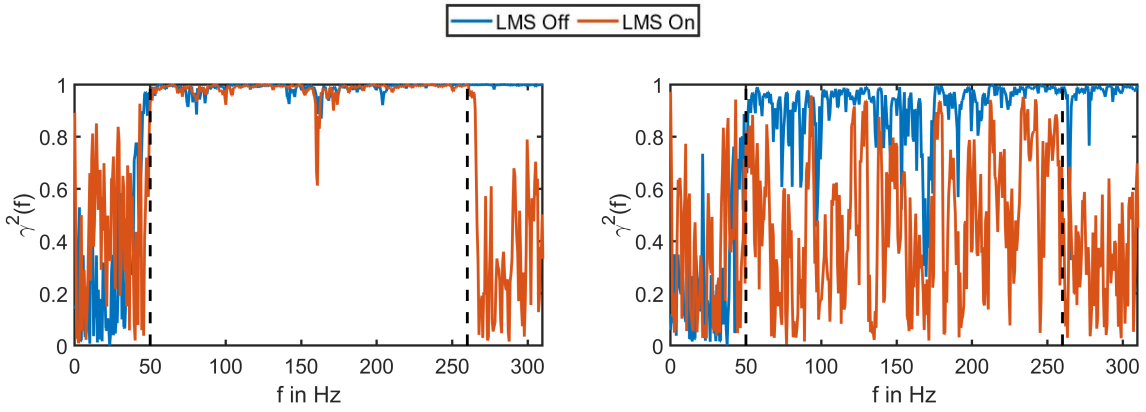

(a) Reference Microphone (Upstream).

(b) Error Microphone (Downstream).

Figure 45: Coherence over frequency with and without active reduction.

microphones, but the most interesting ones are clearly the Reference Microphone upstream and the Error Microphone downstream, which can be seen in Fig. 45. Those coherence plots already give a good indication that the active LMS works as intended, which will further be discussed in Sec. 5.1.

The resulting reduction of the active LMS was recorded at all 16 measurement positions. A comparison of the PSD plots for the active reduction ("LMS on"), the reference signals ("LMS off") and the resulting relative reduction are given for all positions, a selection is plotted here in Fig. 46 and the remaining plots are plotted in Apx. B, Fig. 57. Next to the Ref. and Err. Microphones, Fig. 46 shows one more position upstream (Mic. A), one position in the mixed interference area (Mic. B) and two positions downstream, one in front of the Err. Mic (Mic. C) and one further downstream (Mic. F). All characteristic values for all 16 positions are listed in Tab. 7. Even a quick glance at the results confirms that active absorption works. Further discussion follows in Sec. 5.1

One last important thing to be able to evaluate the quality of the achieved reduction is to look at the energy levels in the background noise. Fig. 47a plots the PSD graphs of the background noise for both the Reference and the Error Microphone. Fig. 47b shows a direct comparison between the background level for the Error Microphone from the graph to the left and the achieved reduction found in Fig. 46b.

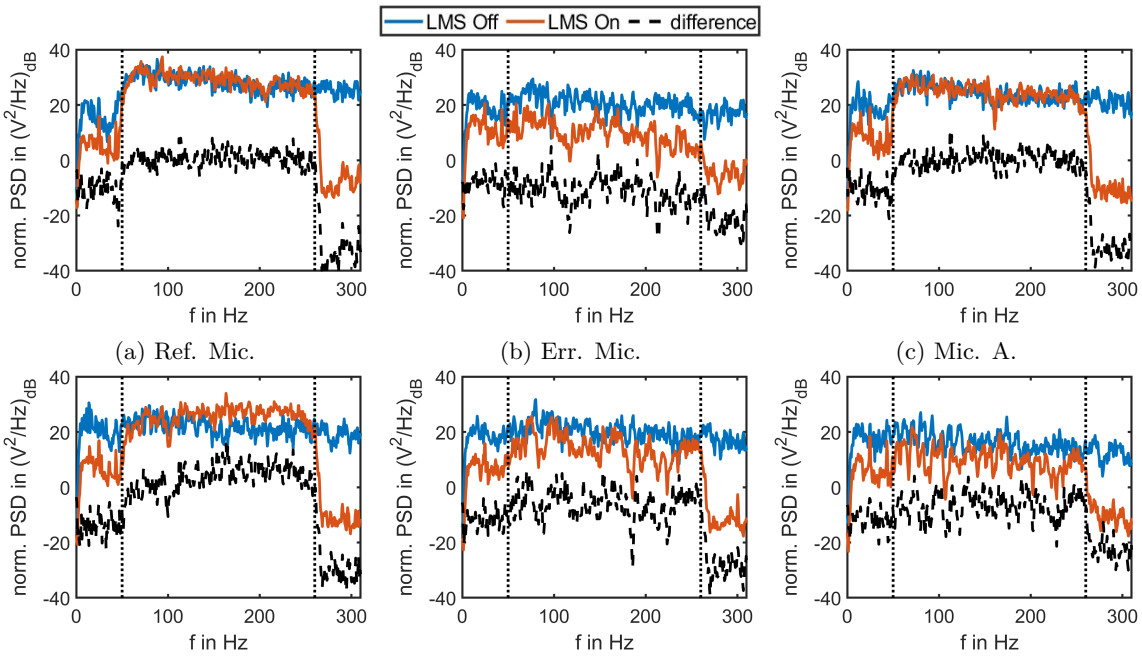

(a) Ref. Mic. (b) Err. Mic. (c) Mic. A.

(d) Mic. B. (e) Mic. C. (f) Mic. F.

Figure 46: Measurement Results of Setup1: The normalised PSD graphs for a selection of measurement microphones. All measurement results listed in Tab. 7.

	∅ reduction (dB)	max./min. reduction (dB)	max./min. reduction at f_{max}/f_{min} (Hz)	AAD (dB)	region
Ref. Mic.	0.50	-6.20 / 8.00	135 / 149	2.22	Upstream
Err. Mic.	-11.01	-26.93 / 4.98	215 / 98	3.91	Downstream
Mic. A	0.00	-7.52 / 9.23	80 / 113	2.44	Upstream
Mic. B	3.36	-15.91 / 15.64	51 / 164	4.08	Mixed Interference
Mic. C	-6.17	-29.21 / 5.75	186 / 71	4.17	Downstream
Mic. D	-7.15	-23.80 / 5.44	80 / 113	4.04	Downstream
Mic. E	-8.58	-21.62 / 10.26	125 / 103	4.09	Downstream
Mic. F	-6.63	-21.37 / 4.03	229 / 74	3.83	Downstream
Mic. 1	0.48	-9.10 / 9.17	78 / 234	2.55	Upstream
Mic. 2	2.33	-16.66 / 16.98	78 / 98	4.55	Downstream
Mic. A'	0.12	-7.64 / 9.80	230 / 144	2.40	Upstream
Mic. B'	3.82	-11.18 / 14.61	251 / 144	3.54	Mixed Interference
Mic. C'	-5.89	-22.67 / 7.93	198 / 137	4.34	Downstream
Mic. D'	-6.45	-24.01 / 10.21	107 / 258	4.68	Downstream
Mic. E'	-6.97	-22.50 / 5.61	129 / 165	3.90	Downstream
Mic. F'	-7.13	-24.04 / 8.97	219 / 103	4.57	Downstream

Table 7: Achieved active absorption for Setup 1. Average reduction in dB, maximal and minimal reduction in dB with corresponding frequency and AAD in dB. Corresponding graphs: Fig. 46 and Fig. 57 (Apx. B).

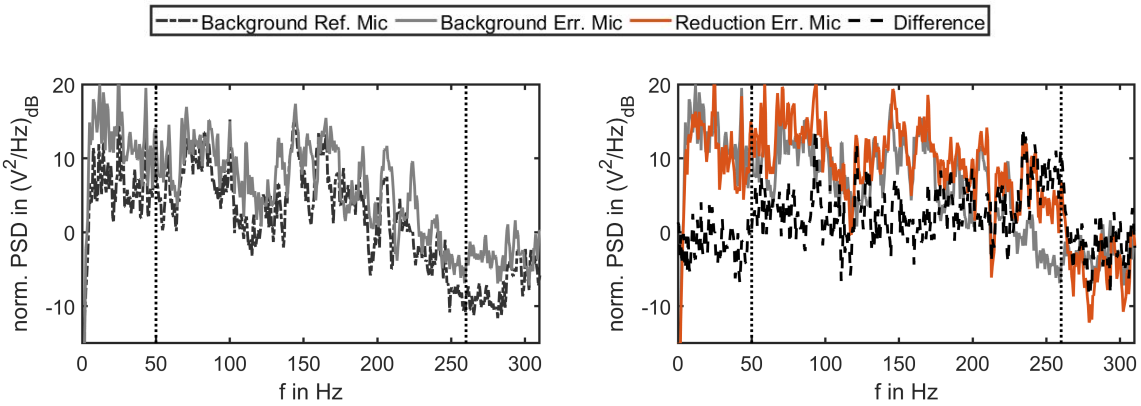

(a) Background Noise PSD, Err. + Ref. Mic.

(b) Err. Mic.: Comparison between background noise and achieved reduction.

Figure 47: Setup 1: Normalised PSD of background noise and comparison with achieved reduction.

4.2. Results of Setup 2

As already mentioned in Sec. 3.2, all recorded live data of the active LMS are not usable. However, from some recorded test signals, impulse responses to microphones A - F can be obtained to create offline measurement data, which will be shown here instead.

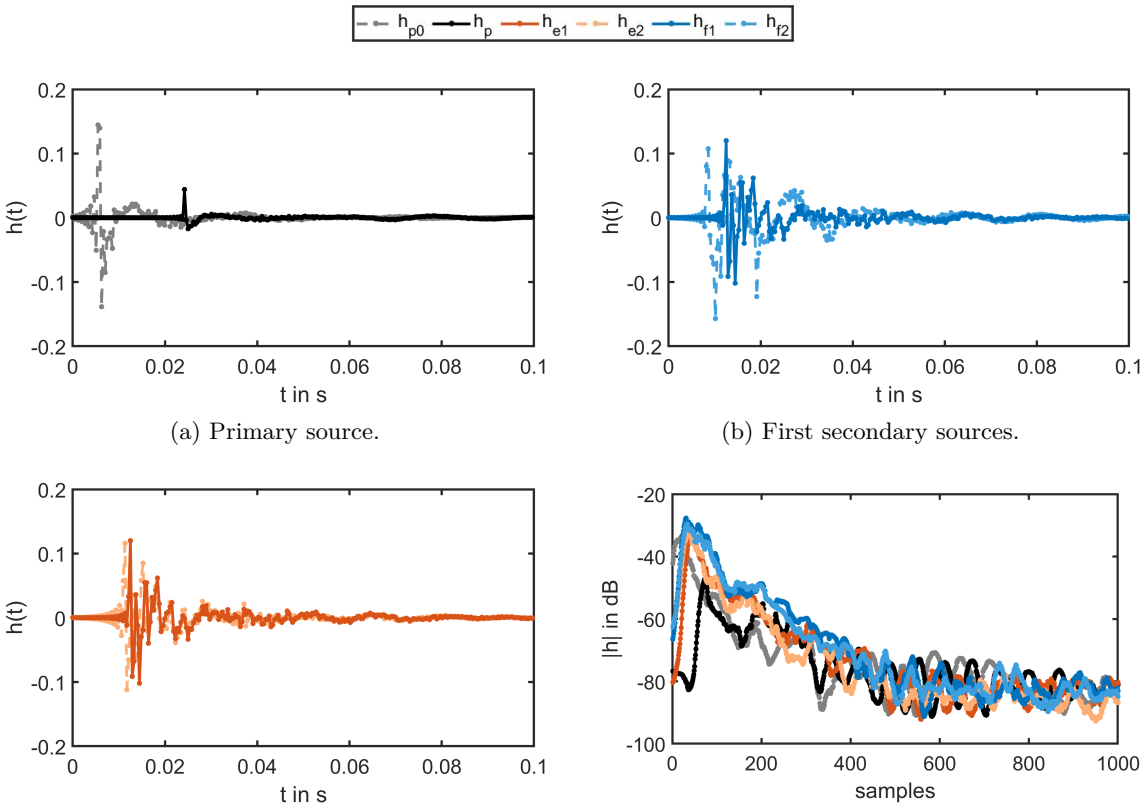

(a) Primary source.

(b) First secondary sources.

(c) Second secondary sources.

(d) Decay of all IRs, moving average (25 samples) applied.

Figure 48: Measured impulse responses for Setup 2

A white noise signal with length $T = 16$ s was used as the input signal for the H_1 estimation, resulting in 13 blocks to average over with the windowing length again set to 2^{12} samples.

The measurements of the impulse responses $\boldsymbol{h}_\mathrm{p}$ to $\boldsymbol{h}_\mathrm{f2}$ are seen in Fig. 48a to Fig. 48c. By accident, a distorted measurement of the $\boldsymbol{h}_\mathrm{e1}$ and $\boldsymbol{h}_\mathrm{e2}$ measurements were used to perform the LMS, rendering the live data unusable. Therefore, artificial measurement results based on the non-distorted impulse responses are shown here. The LMS method was redone in retrospective, which results are shown in Fig. 49. The frequency range is set between 60 Hz and 155 Hz. The lower end is raised here from 50 Hz for better results. As the FIR filters from the previous section might have benefited from more filter bins, the filters shown in Fig. 49b are given a generous length of 1000 samples, although this does not seem to impact the results significantly. Judging from the decay rates depicted in Fig. 48d, around 500 filter bins could be sufficient, as all impulse responses have decayed by 60 dB or more at this point. The characteristic values for the PSD graphs shown in Fig. 49c and Fig. 49d are again summarised in a table, see Tab. 8 below.

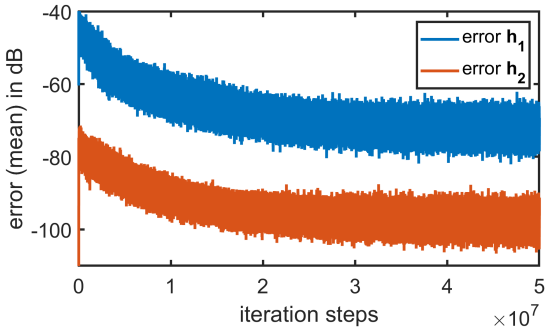

(a) Error progression over iterations, moving average applied.

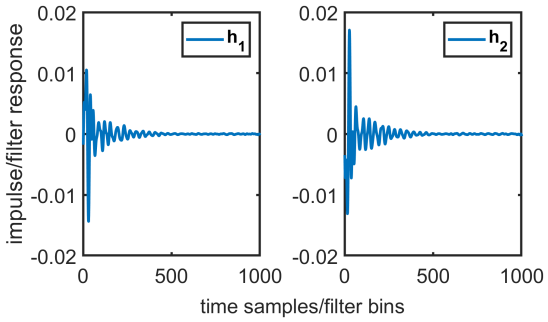

(b) FIR filters.

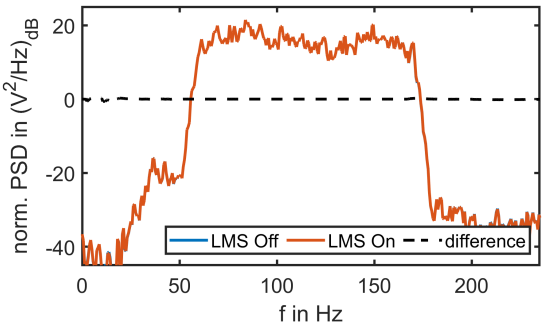

(c) Upstream estimated PSD with relative error.

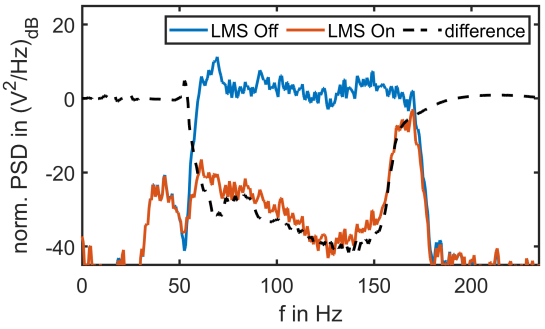

(d) Downstream estimated PSD with relative reduction.

Figure 49: Results of the LMS for $\alpha_1 = 5 \cdot 10^{-5}$, $\alpha_2 = 7 \cdot \alpha_1$, filter length $N = 1000$, between 60 Hz - 155 Hz, after $5 \cdot 10^7$ iterations. Reduction values listed in Tab. 8.

	∅ reduction (dB)	max./min. reduction (dB)	max./min. reduction at $f_{\max}/f_{\min}$ (Hz)	AAD (dB)
Ref. Mic.	$0.60 \cdot 10^{-3}$	$-8.25 \cdot 10^{-3}$ / $8.22 \cdot 10^{-3}$	72 / 78	$1.50 \cdot 10^{-3}$
Err. Mic.	-33.97	-41.60 / -21.32	138 / 61	4.30

Table 8: Estimated active absorption for Reference and Error Microphone as a result of the LMS method for Setup 2. Average reduction in dB, maximal and minimal reduction in dB with corresponding frequency and AAD in dB. Corresponding graphs: Fig. 49c and Fig. 49d.

From the measurement data, additional impulse responses from the primary source and the secondary sources to Microphones A to F can be created[14]. The reference signals for all positions were recorded with a $T = 16$ s white noise signal. The same signal is now first convolved with the recorded impulse responses between all sources and the respective microphones and then further convolved with the FIR filters obtained by the LMS method (to illustrate this, look again at the signal plan in Fig. 32b.

However, before the artificial signals of the active LMS are used further, the corresponding *background noise* recorded at the respective position is *added* to each signal. Even if the noise added in this way is of course not completely random, the same frequency dependent energy levels from

[14] Unfortunately, the paths from the secondary sources to the measurement position A' to F' have not been recorded which is why these position are discarded.

the real setup are now added to the signals. This makes the artificially generated signals much more similar to real measurement recordings.

From the data obtained in this way, the coherence can be calculated, which is plotted in Fig. 50b for the Reference and Error Microphone. This also shows how important the addition of background noise is; if the noise had not been added, the coherence for the downstream position would also be close to one, which of course would make no sense.

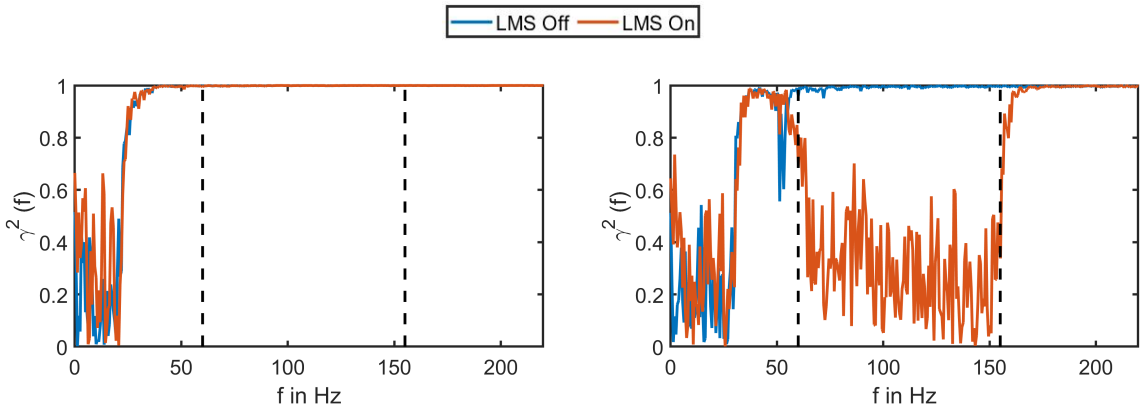

(a) Reference Microphone (Upstream). (b) Error Microphone (Downstream).

Figure 50: Coherence over frequency with and without active reduction.

Now that all measurement data of the active LMS have been created, their PSD graphs can be compared with the actually measured background levels. The comparing PSD graphs for all microphones are seen in Fig. 51, the table which summarises important characteristics is found in Tab. 9.

	∅ reduction (dB)	max./min. reduction (dB)	max./min. reduction at f_{max}/f_{min} (Hz)	AAD (dB)	region
Ref. Mic.	$0.72 \cdot 10^{-3}$	$-8.45 \cdot 10^{-3}$/ $1.60 \cdot 10^{-3}$	71 / 77	$2.15 \cdot 10^{-3}$	Upstream
Err. Mic.	-27.00	-34.14 / -15.34	136 / 86	2.95	Downstream
Mic. A	0.15	-2.03 / 3.20	121 / 68	1.23	Upstream
Mic. B	0.92	-11.12 / 7.24	62 / 72	2.54	Mixed Interference
Mic. C	-9.33	-25.13 / 0.83	89 / 72	4.29	Downstream
Mic. D	-7.05	-15.95 / 1.77	115 / 72	2.90	Downstream
Mic. E	-18.04	-32.29 / -5.23	147 / 72	4.22	Downstream
Mic. F	-7.83	-19.19 / 7.95	121 / 72	3.94	Downstream

Table 9: Achieved active absorption for Setup 2 from artifical measurement data. Average reduction in dB, maximal and minimal reduction in dB with corresponding frequency and AAD in dB. Corresponding graphs: Fig. 51.

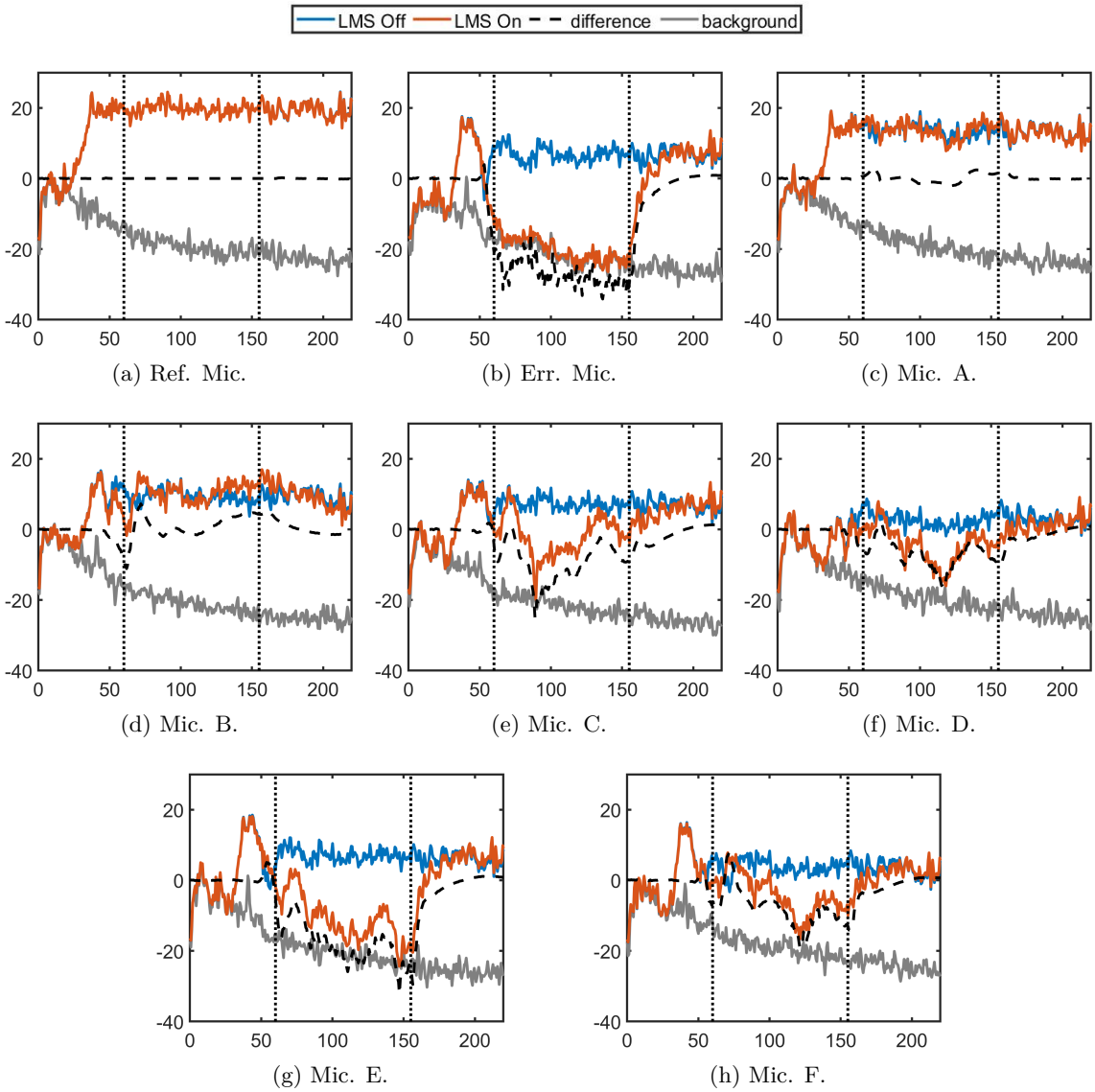

(a) Ref. Mic. (b) Err. Mic. (c) Mic. A.

(d) Mic. B. (e) Mic. C. (f) Mic. D.

(g) Mic. E. (h) Mic. F.

Figure 51: Measurement Results of Setup1: The normalised PSD graphs for a selection of measurement microphones. All measurement results listed in Tab. 9.

5. Discussion

5.1. Discrete Line Array (Setup 1)

5.1.1. Assessment of the presented LMS solution and peculiarities of Setup 1

Even at first glance, it is clear that the measurement results presented in Sec. 4.1 confirm that the method largely works as intended. As already outlined in the Setup (Sec. 3.1), a major concern beforehand was whether the speakers could be positioned accurately enough. When the impulse responses shown in Fig. 43 are looked at for their entire duration, it is noticeable that all impulse responses that describe a path which ends in the Error Microphone (h_p, h_e1 and h_e2), are a bit noisier than their counterparts, but not by a lot. Fig. 43d which shows the decay of the impulse responses confirms this, as all of them have very similar decay rates, but the mentioned impulse responses remain at a slightly higher absolute value. All impulse responses show an oscillation with a periodicity of 0.02 s ($\widehat{=}$ 50 Hz) which is most likely caused by hardware limitations. With that in mind, it becomes clear that all impulse responses resemble the analytical/simulated results (for example seen in Fig. 22a), if they were high-passed at 50 Hz.

Of course simply looking at the impulse responses is not enough to conclude that the source arrays were actually able to recreate a sound field similar to that of a true line source or a very long discrete line array. A strong indicator that this was actually not the case is the overall lesser coherence at the Error Microphone, seen in Fig. 45b. But even if the goal to represent a line source cannot be confirmed or refuted with certainty at this point, it does emphasize the robustness of the LMS method. Speaking of the LMS, the results presented in Fig. 44/Tab. 6 show the already very familiar characteristics seen many times throughout this thesis. If the Error progression over iterations (Fig. 44a) is considered in respect to the recommendations presented in section Sec. 2.4.1, it is thinkable that an even better result could have been achieved if the lower frequency range had been raised, for example to 80 Hz. Looking at the progression of $\boldsymbol{h}_1$ and $\boldsymbol{h}_2$ it is reasonable to assume that longer filters might have been beneficial, as the FIR filters have not fully declined at the end. However, in this case it would have most likely not further improved the results, as will be analyzed at the end of this section. Interestingly, the peaks of the impulse responses $\boldsymbol{h}_\mathrm{e1}$ and $\boldsymbol{h}_\mathrm{e2}$ are higher than those of $\boldsymbol{h}_\mathrm{f1}$ and $\boldsymbol{h}_\mathrm{f2}$, although the distance to the Reference Microphone is shorter than to the Error Microphone. This can best explained with the orientation of the loudspeakers; the loudspeakers are facing towards the Error Microphone, which can be seen in Fig. 34 and Fig. 35.

The given solution predicts an average deviation of 0.02 dB upstream with a very low AAD of 0.1 dB and an average reduction of -20.73 dB and an AAD of 4.48 dB downstream. The best reduction is predicted to be achieved at 124 Hz, with a reduction of ≈-37 dB and the least reduction is predicted to be realised at 98 Hz with just ≈-2.5 dB in reduction. Whereas this very low achieved reduction at 98 Hz seems to be affecting a very narrow frequency region, there is a wider region where the achieved reduction is quite low, centering around the 170 Hz mark. When looking at the Coherence plots in Fig. 45, it becomes clear that both relatively bad results are caused by inherent properties of the system. The coherence for the reference signal (h_p0 and h_p, or here labeled as "LMS Off") show a significant dip at 98 Hz/170 Hz at the downstream position and a less noticeable drop at 160 Hz at the upstream position. This indicates that the whole system has either a resonating or anti-resonating effect at those frequencies. Looking at the various PSD plots, it seems more likely that a dampening effect is at play here. 98 Hz corresponds to 3.5 m of wavelength, 160 Hz/170 Hz correspond to 2.14 m/2.02 m respectively. None of the three dimensions seem to directly be in relation to any important dimension of the setup, so it is not immediately clear what causes these dampening effects. However, this has little impact on the overall performance. A very insightful information contained in the coherence plots is that the method works, at least qualitatively. When the LMS is "turned on", the coherence within the relevant frequency range remains close to 1 at the upstream position (except for the already discussed dip around 160 Hz) and drops significantly

at the downstream position. Note that the signal for the active LMS was band-passed, so a bad coherence outside the working frequency range is to be expected.

5.1.2. Evaluation of achieved reductions (live data)

To evaluate the results quantitatively, the normalised power distribution of the reference signal is compared with that of the active reduction signal at every measurement position, together with the relative reduction deduced from that. The following analysis is structured in three parts, in the upstream, mixed-interference and downstream part, with a focus on the achieved reduction at the Error Microphone in particular at the end. All signals were recorded with a length of at least 11 s, resulting in at least six averages over the spectrum (with overlap). The signals were recorded over a time span of almost three hours with sometimes considerable time between the individual measurements. As a result, each measurement might have been impacted by slightly different background noise levels.

Four microphones were placed in the *Upstream* region: The Reference Microphone, Mic. 1, Mic. A and Mic. A' (Fig. 46a, Fig. 57c, Fig. 46c and Fig. 57e). As expected, the overall best result is achieved in the Reference Microphone, with an average increase of 0.5 dB across the whole frequency range and an AAD of just 2.22 dB, which is the lowest for all measurement positions (again, see Tab. 7). The average deviation and the AAD recorded at the Reference Microphone are both a magnitude bigger than the predicted values of ∅ 0.02 dB/AAD0.1 dB, but it was not to be expected that these values would actually be achieved. It is rather surprising how good the achieved values actually are.

The visualised simulation results of the relative absorption presented in Sec. 3.1, Fig. 37 and the previous results presented in Sec. 2.5 suggest that the (average) deviations in the upstream area should be very small at all positions. The other measurements confirm this. Mic. 1, Mic. A and Mic. A' all have very low average deviations, below 0.5 dB, and AADs close to 2.5 dB. Looking at their respective PSD graphs, it becomes clear how closely these results are to that of the Reference Microphone. Even Mic. A and Mic. A', which were not positioned close to the ground but at heights of 1.6 m and 0.8 m respectively achieve good results. The good results in Mic. 1 (which was positioned right at the edge of the foliage) also indicate that the regions close to the walls are not significantly negatively affected by scattering or diffraction, as was assumed in the first place. **It seems that the presented method can actually control the complete Upstream area with only one boundary condition inserted in the Reference Microphone.** Interestingly, all microphones but the Reference Microphone show the already discussed dip at 160 Hz in the power distribution.

Two microphones, Mic. B and Mic. B' were placed in the mixed interference region, with a bit less than 1 m distance to the second row of secondary sources and at a height of around 1.7 m each. When looking at the power distribution (Fig. 46a and Fig. 57f) it is visible that at the lower frequency range, the power density is very similar to that of the reference signal, but it increases towards the higher end of the frequency range. When looking at the predicted relative change of the pressure field in the surface plots in Fig. 37a and Fig. 37c, it can be seen that **the increase in power density at the higher frequencies occurs exactly as predicted due to geometric interferences in the not controlled area**.

Arguably the most interesting part of the measurement results are the achieved Downstream attenuations and whether or whether not these data are enough to reconstruct the emerging reduction pattern. This is also the reason why most of the verification positions were placed in the downstream area. However, as already mentioned in the Setup (Sec. 3.1), originally there had been more measurement positions but due to errors in recording the reference signal, these measurements are unusable. Many of these additional positions were mirrored across the x-axis in order to be able to

make statements on the symmetry of the resulting field, as this property is relatively easy to test.

One microphone that shows very contradicting results is Mic. 2. According to the documentation protocol of the experiment, Mic. 2 should have a reference signal that is usable, but it is more likely that it was already affected by the application error and its results should therefor be discarded. However, its results are included for the sake of completeness but not further discussed.

With the exception of Mic. 2, all measurement positions show that at least some level of active reduction is achieved when averaging of the frequency range. The best reduction is of course achieved at the Error Microphone (Fig. 46b), with an average reduction of -11.01 dB and an AAD of 3.91 dB. This achieved reduction is significantly less then what is predicted by the LMS results (-20.73 dB) but the AAD is quite similar. Within the frequency range, the highest reduction of -26.93 dB is achieved at 215 Hz and a very similar reduction of -26.19 dB is achieved at 117 Hz. The remaining microphones (with the exception of Mic. 2) measure average reduction values between -5.89 dB and -8.58 dB and AADs roughly between 4 dB and 5 dB.

But the results show that the power densities across the spectrum are not only reduced. The highest increase in power density occurs at 98 Hz, with an added 4.98 dB to the power spectrum. However, this is exactly the frequency where the LMS method is predicting the worst local result, as already mentioned above. This seems to coincide with the in comparison quite low coherence at that frequency. Also, it appears to be affecting the results at all other positions Downstream, as they all achieve particularly bad results around 98 Hz. This happens regardless of whether or not the reference signal there has a high or low energy density. Interestingly, a similar effect where all measurement positions are negatively affected can not be observed at 170 Hz, where another huge drop in the coherence occurs.

The active reduction recorded at the Error Microphone adds energy density at three isolated frequencies (+4.98 dB at 98 Hz/+3.15 dB at 148 Hz/+0.19 dB at 191 Hz). All of them have in common that the energy density of the reference signal is particularly low at that frequency and at that frequency only. Therefore, it is questionable if that deviation would even be perceivable. Overall these isolated increases in the power spectrum should not be given too much weight. However, all microphones record increases in the power density for isolated frequencies or small frequency bands (up to 10.26 dB at Mic. E), but mostly below the +5 dB mark.

What is still left unclear is whether or not the recorded reduction field resembles the inhomogeneous pattern predicted for the Downstream region. Unfortunately, not enough measurement positions were covered to create surface plots similar to those seen in the Setup (Fig. 37), but a different attempt of visualising the achieved reduction field is made in Fig. 52 below. Here, based on the isometric representation in Fig. 36, each position is assigned its average absorption value. The result from Mic. 2 (as it is most likely corrupted) is marked in orange. This illustration makes quite clear that there is a "shadow zone" were the reference field is actively reduced, but is also makes clear that the number of measurement positions is not enough to conclude anything about the absorption *pattern* itself. It is quite likely that a pattern similar to that of the simulation results emerged, as the previous results aligned quite well with the simulation results. This is further underlined by the subjective impression of participants walking through the absorption area. It is possible that with a stronger signal from the primary source, the pattern would be more obvious even with the limited amount of measurement positions, as some of these measured reductions might be very close to their theoretical achievable maximum.

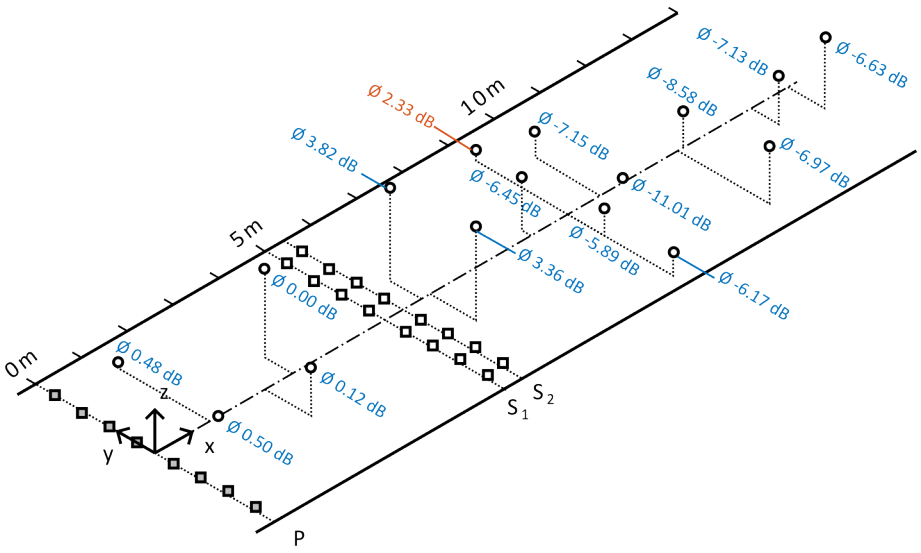

Figure 52: Setup 1, results - Isometric view of the microphone positions with average reduction values across the frequency range.

5.1.3. Comparing achieved reduction to background noise levels

But how good would the possibly best achievable reduction be for this very setup? This is the last and probably most important question that shall be answered before moving on to the evaluation of Setup 2. To answer this, the background noise levels must be given a closer look.

When looking at the energy densities of the background noise measurements of the Reference and the Error Microphone (Fig. 47a) a few things are noteworthy. First of all, both microphones recorded very similar energy levels, but the background noise levels at the Error Microphone are overall higher[15]. Secondly, the signal played through the primary speaker should probably have been raised in sound level, as the difference between the background noise level and the reference signal should have been greater to allow more room for possible attenuations.

The averaged achieved reduction at the Error Microphone (-11.01 dB) does not appear to be outstanding at first, as the expected value is almost double of that (-20.73 dB). However, this does not take into consideration the present energy density in the background noise. When directly comparing the achieved reduction at the Error Microphone and the background noise level (done in Fig. 47b, an astounding thing becomes clear: the power density curve has an average deviation to the background noise level of only 3.3 dB and when looking only up to 230 Hz, it reduces to just 2.55 dB. This means that **the LMS solution used here was able to reduce the energy density in the applied frequency range at the Error Microphone almost to the level of the background noise level**. It is therefore unlikely that the results for this setup could have been significantly improved with different settings of the LMS method.

[15] Listening to the background noise measurements reveals that the sound of a ventilation shaft was recorded, which was closer positioned to the Error Microphone.

5.2. Discrete Curved Array (Setup 2)

As already mentioned in Sec. 3.2, the recorded live data of the active LMS is not usable due to an application error. However, with the help of the impulse responses between all sources and microphones A to F, artificial measurement data was created that gives a good idea on how the live data might have looked like.

5.2.1. Assessment of the presented LMS solution and peculiarities of Setup 2

Even though Setup 2 does not require such tight tolerances as Setup 1, great care was taken to place all sources very accurately. Together with the very controlled measurement environments within the anechoic chamber, very clean measurements of the impulse responses could be made. The (non) distorted impulse responses seen in Fig. 48 all decay to an average level below -80 dB. They resemble the simulated impulse responses (best seen in Fig. 29b) to a good extent, at least if they were high-pass filtered with a cutoff frequency of approx. 50 Hz. As already mentioned in Sec. 5.1.1, this seems to stem from technical limitations of the used loudspeakers (which fits the data sheet of the used loudspeakers, see again Tab. 3). This is further supported by a drop in the coherence of the reference signal ("LMS off") at the Error Microphone (seen in Fig. 50b) at that frequency. An almost invisible drop of coherence also occurs at the Reference Microphone (Fig. 50a). This is the reason why the frequency range of the LMS was raised to 60 Hz in comparison to the simulation on which that setup is based on. As expected, the coherence at the Error Microphone in the relevant frequency range is not as good as at the Reference Microphone, but it is overall still very close to one.

The LMS results (shown in Fig. 49/Tab. 8) also show the advantages to be expected when measuring in an anechoic chamber. The error progression converges smoothly, the FIR filter decay steadily and the progression of the estimated reductions of power densities look very similar to those of simulation results (e.g. seen in Fig. 30). With the prediction of an average reduction of almost -34 dB downstream and only $0.6 \cdot 10^{-3}$ dB added on average upstream, the proposed solution is also very promising. Besides the drop in coherence around 50 Hz (which lies outside the working range of the LMS) no noteworthy resonances or anti-resonances can be detected in either coherence or the PSD plots. It is interesting to note that the achievable reduction increases with higher frequencies, possibly influenced by the course of the energy density in the background noise (seen as gray in the plots shown in Fig. 51). Just as for Setup 1, the speakers in Setup 2 face in the downstream direction, which probably explains why the FIR filter $\boldsymbol{h}_2$ has slightly higher amplitudes than $\boldsymbol{h}_1$.

5.2.2. Evaluation of achieved reductions (offline)

Just as was already done for the results of Setup 1, to evaluate the results quantitatively, the normalised power distribution of the reference signal ("LMS Off") is compared with that of the active reduction signal ("LMS On") at every measurement position, shown together with the relative reduction deduced from that. The following analysis is again structured in three parts, in the upstream, mixed-interference and downstream part. The input signal for both the reference signal and the signal of the active LMS is a white noise signal with length $T = 16$ s, resulting in 13 averages over the spectrum (with overlaps). The recorded background noise levels are added to all measurement signals. As a result, each artificial measurement is impacted by exactly the same background noise levels as its corresponding reference signal. This will improve the generated signals in comparison to actual live data, but this influence should be small due to the averaging of the spectra and the very well-controlled measurement environment of the anechoic chamber. Under this circumstances it is conceivable that live data would show very similar results.

Due to the limitations in the available measurement positions, only two microphones in the upstream region can be evaluated: the Reference Microphone and Microphone A. As expected, the Reference Microphone (see Fig. 51a) shows almost identical values to the prediction by the LMS method. All characteristic reduction values show a maximum deviation a little over $1 \cdot 10^{-3}$ dB, most of them around $1 \cdot 10^{-4}$ dB. But these are of course only the values at the Reference Microphone. Microphone A (see Fig. 51c) shows still very low, but in comparison much higher deviations with an average deviation of 0.15 dB and an AAD of 1.23 dB. As Microphone A was placed 1.8 m to the side of the Reference Microphone and 1.6 m above ground (as reference for the microphone positions, see again Tab. 5), this gives a good **indication that the entire upstream region is successfully controlled by its boundary condition and deviations are kept close to 0 dB**. However, more measurement positions would be necessary to reach this conclusion with greater certainty.

Only the results of one microphone in the mixed interference area are available, Microphone B. But **it shows exactly the expected course in the mixed interference area**, with little to no deviations at lower frequencies and an increased energy density towards 155 Hz. Although the surface plot in Fig. 42 does not exactly show the slice where Mic. B is placed, it still indicates a relative increase up to 6 dB at 155 Hz, which is confirmed by the 4.5 dB which are relatively added at 155 Hz. Contrary to expectations, the highest overall increase occurs at 72 Hz, with an added 7.24 dB. When looking at Tab. 9, it becomes clear that all generated measurements achieve their weakest reduction at 72 Hz exactly. As neither the coherence plots nor the LMS solution indicate an (anti) resonance at that frequency, it is not entirely clear what causes this effect.

Now to the downstream area, where a total of five of the eight microphones are positioned. Of course, the Error Microphone shows the overall best results. The average reduction is -27 dB, with a maximum reduction of about -34 dB at 136 Hz and a minimal reduction of about -15 dB at 86 Hz. Interestingly, the AAD of the generated measurement data is lower than that of the simulated solution (AAD = 2.95 dB vs. $\mathrm{AAD}_{\mathrm{sim}}$ = 4.3 dB), which definitely has to do with the addition of background noise. When comparing the course of reduction with the energy density present in the background noise, it becomes very clear that **the presented solution reduces the energy density of the noise field at the boundary condition of the Downstream region to background noise level**. Of course, this is hardly surprising and the results from the other measurement locations are all the more interesting.

Microphone E is the microphone closest to the Error Microphone and shows the second best overall reduction across the frequency range. The surface plots in Fig. 42 indicate that microphone E is located at the edge of the "main absorption area" surrounding the Error Microphone, which exhibits strong absorption at almost all frequencies. Still, with about -18 dB reduction on average and aa AAD of over 4 dB, the reduction here is significantly weaker, although still clearly present. Again the least best reduction is achieved at 72 Hz with only a little more than -5 dB in reduction without a clear indicator why this is the case.

Microphones C, D and F all lie outside the "main absorption area" and this is reflected in their overall lower reduction values, which achieve average absorption values between approximately -7 dB and -9 dB. All of those achieve their least bets reduction at 72 Hz, whereby all of them even show an increase in energy density. The most energy density is added at position F, where the rise in the active LMS signal coincides with a drop in the reference signal, increasing the energy density by almost 8 dB. It is unlikely that the low energy density in the reference signal at that frequency and the poor performance of the LMS are coincidental. Again looking at the surface plots in Fig. 42, it becomes clear that very high reduction values are only to be expected in short frequency sections at the microphones with a greater distance to the error microphone. This is confirmed in the corresponding PSD plots of microphones C, D and F (Fig. 51e, Fig. 51f and Fig. 51h). Microphone C shows a very localised high reduction of -25 dB at 89 Hz, similarly Microphone D shows -16 dB at 115 Hz and Microphone F shows -19 dB at 121 Hz. Microphone C shows the sharpest

increase in reduction which even reaches background noise levels, whereas D and F show a bit wider frequency range where the reduction performs especially good. The courses of Microphone D and F are overall quite similar, which is a good indication that the sound field is indeed symmetric. **Overall all these downstream microphones show the expected reduction patterns, with the exception of bad performance at a single shared frequency**.

Finally, to give a similar representation of the achieved reduction pattern as it was given for the evaluation of Setup 1, Fig. 53 shows again the isometric view of the microphone position with their corresponding average reduction values. The mirrored microphone positions are left empty to not imply that the assumed symmetry actually exists, even though the similar results of Microphones D and F are a strong indication.

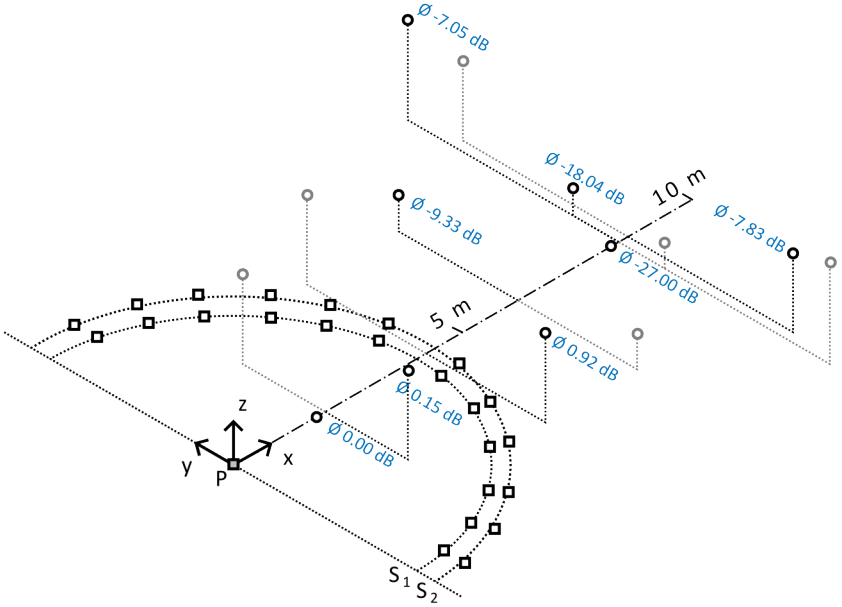

Figure 53: Setup 2, results - Isometric view of the microphone positions with average reduction values across the frequency range.

5.3. Comparison of results between Setup 1 and Setup 2

Although the experimental setups and test environments of Setup 1 and Setup 2 differ in key aspects, the results are comparable and even quite similar. The biggest difference is, of course, that Setup 1 shows live data from a test setup that has only been controlled / optimized to a limited extent, whereas the impulse responses from Setup 2 were recorded under almost perfect conditions and the measurement data was generated from this. However, similar conclusions can be drawn from both. The evaluation of the measurement data shows that both systems contain some frequency dependent non-linearities (around 160 Hz - 170 Hz for Setup 1, 72 Hz in Setup 2 and 50 Hz in both Setups) where the LMS method performs quite bad, but those non-linearities do not generally restrict the operation of the LMS, proving its robustness and therefore potential usefulness for further applications.

Since the results of Setup 1 originate from live data, an attempt can be made to infer from the results of Setup 1 how live data of Setup 2 might differ from the generated results. Of course this will be made with the special features of the test setups in mind.

The Upstream Region is controlled by the signal recorded at the Reference Signal. The LMS

method predicts an average deviation of just -0.02 dB with an AAD of $\sigma = 0.1$ dB (comp. Tab. 6). The actual measured deviation lies at $\varnothing$ 0.5 dB/AAD 2.22 dB; both values are one order of magnitude bigger than their prediction. The generated data for Setup 2 reaches the predicted values of $\varnothing 0.6 \cdot 10^{-3}$ dB/AAD $= 1.5 \cdot 10^{-3}$ dB almost perfectly, even though the background noise was added to the data already. Nevertheless, it is unlikely that a real measurement would come so close to the theoretical value. Assuming a real measurement for setup 2 would also deteriorate from the predicted results by an order of magnitude, ≈ 0.1 dB of average deviation and ≈ 0.01 dB AAD would be achieved. However, possible interactions between the sources (near field effects) if they all emit sound simultaneously are not considered here. The magnitude of such theoretically possible interactions cannot be estimated on the basis of the available data. Another indicator that the Reference Microphone would probably not reach those levels are the results of Microphone A, which measure an average deviation of 0.15 dB upstream. In Setup 1, all measurement positions upstream reached very similar results, regardless of their exact location.

A similar conclusion can be made for the Downstream reduction on the Error Microphone. The results of Setup 2 show that the energy density levels are pushed down to the background noise level almost exactly. However, the live data from Setup 1 showed that there is an average deviation of 3 dB to the background noise level[16]. The SNR at the Error Microphone in Setup 1 is a whole order of magnitude worse than that in Setup 2 (see Fig. **??**/Fig. **??**). Assuming that this could be directly translated to the result of a live measurement, average deviations in the order of 0.3 dB could be expected here.

At first glance, it seems illogical that the remaining measurement microphones show very similar AADs in both setups (on average 3.8 dB across all other positions in Setup 1 and on average 3.2 dB across all other positions in setup 2), but this is due to the different absorption patterns. In setup 1, the fluctuations are distributed over the entire frequency spectrum, whereas the high standard deviation in setup 2 is due to the fact that the average reduction achieved is not particularly high, but is significantly higher for a very small frequency range. Therefore, the downstream positions cannot be compared here. The only microphone positions that can be compared meaningfully are Microphone A and A' of Setup 1 with Microphone A of Setup 2. Microphone A of setup 2 shows roughly half the AAD of those of Setup 1 (1.23 dB vs 2.44 dB). It would be very interesting to see which reductions and AADs a setup similar to that of Setup 1 could achieve, if it was tested in conditions as favorable as that of Setup 2.

To conclude that comparison: both Setups achieve their goal of controlling both the Upstream and the Downstream region withing the limitations of their setups and test environments. With the help of the live data of Setup 1, it can be speculated how much the live data of Setup 2 would deviate from the generated data. But regardless whether or not those speculations are realistic, it is clear that the generated data is the upper (or lower) bound for what is achievable in a real test of Setup 2.

[16] Which were recorded with a considerable time difference to the live data, which makes this result less significant.

6. Conclusion

The aim of this work was to actively control the Downstream attenuation of sound propagation in free field scenarios based on the absorption inside the duct presented by Swinbanks [15] with a focus on the low frequency end. The extended LMS method based on the works of Kropp et. al. [18] proofed to be a robust method to find the needed FIR filters $\boldsymbol{h}_1$ and $\boldsymbol{h}_2$ once good convergence parameters were found. A rule of thumb how to set those parameters was introduced, namely that the coefficient which controls the error term containing the error paths (α_2) should be seven times larger than the coefficient which controls the error term containing the feedback paths (α_1, comp. to Sec. 2.4.1). This rule proofed to be reliable, but it can certainly be generalised.

First the well known active reduction inside the duct was recreated. Here it was seen that the method works as intended, but due to the present distortions of the used setup, the method was not able to control the upstream region particularly well. Initial assessments of how real measurement results would differ from simulations were made and conclusions drawn for the two subsequent experiments.

Setup 1 focuses on the active reduction of sound emitted by line arrays in real-world free field conditions. To reduce the amount of sources needed for this experiment, the arrays were virtually extended by placing them between highly reflective walls. The experiment was performed on the grounds of the Chalmers University of Technology on the alleyway between two buildings. Despite the high background noise levels, the LMS method was able to find two filters $\boldsymbol{h}_1$ and $\boldsymbol{h}_2$ to actively control the Upstream and Downstream area. All measured results lie within expectations of the simulated results. It was shown that especially the Upstream Region was controlled very effectively, showing the same quality of control found at the boundary condition for all measuring points within the Upstream Area. The average deviation from the undisturbed sound-field in the upstream area is 0.3 dB. The verification positions Downstream indicate that the predicted absorption pattern has actually materialized. At the boundary condition of the Downstream Region the energy density was on average reduced by 11 dB to only an average of 3 dB over the background noise levels. Overall the results of Setup 1 proof that the concepts presented for active reduction/active absorption actually work and are also reasonably robust against (weak) non-linear effects within the adapted frequency range.

Setup 2 further underlines these conclusions, even though the live data was unusable. However, measurement data for the second setup was generated with recorded impulse responses. In comparison with the results of Setup 1 and previous results, it was shown that the generated data probably gives a realistic, qualitative assessment of what real live data would have looked like. These results again show very good control over the Upstream Region with an average deviation of just 0.08 dB from the undisturbed Upstream sound-field. The results indicate that the expected absorption patterns in the Downstream Region is emerging, with almost perfect reduction over the entire active frequency range at the boundary condition. Here the energy density was reduced by an average -27 dB, bringing it to 1 dB above the background noise level.

The LMS method proved to be a good tool for determining the FIR filters to be used in this work. However, the method has its weaknesses, which have been discussed in detail. One problem is the setting of the convergence parameters, which remained a challenge even with the rule of thumb presented. A more systematic approach to setting the parameters would be very helpful here. The method could also possibly benefit greatly from an adaptive stepsize, which could potentially greatly reduce the necessary iteration steps. An iterative step size for SISO systems, the Normalised LMS (NLMS), was originally introduced by Slock [32], and could possibly be adapted for this MIMO system at hand. This task is probably not trivial. Another weakness of the presented LMS method is its occasionally occurring problems to converge and the overall lesser quality of these results when very low frequencies (below 80 Hz) are included, most likely caused by the filter length. Further work could investigate how to improve this issue. A further idea for

expanding the LMS method would be to include more boundary conditions. The simulation show and the measurement data proof that especially the upstream region is well controlled with just a single boundary condition inside, but the achieved reduction in the downstream area varies a lot. To introduce another linear independent boundary condition, another filter must be introduced, which would demand another set of sources or to control different part of the array with different filters.

Based on the very promising results presented of this thesis, there are a multiple of ways how this topic can be further developed in the future. To stay with the setups presented for the time being, a very obvious step would be to check whether energy was actually absorbed from the sound field, for example with the help of intensity measurements. In addition, the resulting sound fields could be measured using microphone arrays in order to measure the reduction pattern with higher spatial resolution. In order to bring the concepts closer to a practical application, other measurement signals should be tested that do not have a uniform energy density (like white noise). Everyday noises, music or speech could be tested for this purpose. For this it would also be interesting to do perception tests with participants that judge the sound field in the upstream area. An average deviation of a few dB is initially a very good result, but if the characteristics of the test signal are easily identifiable by the human ear, such as music, how much would the deviation negatively affect the experience? Would this deviation in a setting of, for example, an open air performance be tolerable or not? In order to enable the active reduction of music at live events, the method would also have to be expanded in two respects; On the one hand, the reference signal would have to be recorded live and processed latency-free. On the other hand, it might be necessary to increase the sampling frequency, which was deliberately chosen very low in this work at just 2.56 kHz, to over 40 kHz. And, of course, for the application possibilities of live events: Can the method be scaled up to control the sound field in upstream and downstream areas tens or even hundreds of meters in size?

In conclusion, the results of this thesis have shown that the active absorption of sound works under free-field conditions and that good to very good results can be achieved with reasonable effort. Based on the promising results, the topic presented also offers many opportunities to expand these concepts in the future.

Appendices

A. Further discussion on the influence of convergence coefficients

As already mentioned in Sec. 2.4.1, the convergence coefficients greatly determine the quality of the solution of the LMS method and whether the LMS converges at all. Here a small study with varying parameters is presented to draw some (non-exhaustive) conclusions from them.

As a starting point, the frequency band of the filter is set between 80 Hz and 1 kHz. The mean square value $E[x^2]$ of the sequence equals 0.2378 [17] and according to Eq. (30), the coefficient α should now be smaller than $9.3 \cdot 10^{-3}$. Both α_1 and α_2 are set to $0.15 \cdot 10^{-3}$ a whole order of magnitude smaller[18]. For the given values the error progression can be seen in Fig. 54a below. Its corresponding frequency response of the downstream path after $10 \cdot 10^5$ steps can be seen in Fig. 55a. As becomes immediately clear, the error diverges rapidly. Reducing $\alpha_{1,2}$ by another two orders of magnitude leads to a stable solution (Fig. 54b). However, both errors converge around -20 dB, which is clearly not enough for a strong absorption across the whole frequency band, as can be seen in Fig. 55b, with a relative error that for the most part does not even fall below the -6 dB limit. Note that for the dimensionless analysis here the desired solution lies at 0 dB as the reference value for the dB conversion is 1.

Applying the 7:1 ratio (comp. Eq. (38)) to a slightly increased value of α_1 leads to the results in Fig. 9, which are discussed in Sec. 2.4.2. However, the lower end of the frequency range has been set to 80 Hz quite arbitrarily, but what about even lower frequencies? In Fig. 54c, the lower end has been set to 30 Hz. Although the coefficient α_1 was lowered to $5 \cdot 10^{-6}$, the solution has problems converging even after $6 \cdot 10^7$ steps[19]. For bigger values of α_1 the error diverges quickly. The error of $\boldsymbol{h}_1$ has reached -34 dB and the error of $\boldsymbol{h}_2$ has reached -52 dB, which leads to a downstream path estimation (Fig. 55c) with a relative error of around -20 dB. Now that the ratio of the coefficients has been changed, the error progressions always show a distance of approx. 20 dB from each other, with the error of $\boldsymbol{h}_1$ always being the larger. It is also notable that the error for $\boldsymbol{h}_2$ shoots up from $-\infty$ at the beginning for all simulations. This can be explained by the initialisation of the two filters, which in the beginning are both set to contain only zeros. As $\boldsymbol{h}_2$ controls the upstream radiation, a filter which contains only zeros results in an error of zero, but as it is adapted together with $\boldsymbol{h}_1$, its error must increase at first to then converge to a solution. This behaviour demonstrates that the formation of the common gradient works as expected.

The *lower end* of the frequency end seems to have a big impact on the quality of the solution. But maybe the frequency range is just too broad; in Fig. 54d and Fig. 55d the lower end remains at 30 Hz and the upper end has been set to 300 Hz. But the solution doesn't improve, only the error variance increases. Setting the lower end to 50 Hz (Fig. 54e and Fig. 55e) improves the results, with even more improvement for setting it back to 80 Hz (Fig. 54f and Fig. 55f). Especially the jump from 50 Hz to 80 Hz as the lower limit has drastically improved the relative error. The last solution already looks quite good and it might further improve with even more steps. Even if no quantitative conclusions can be drawn, **finding a solution seems to become more difficult**

[17] Units were neglected for this analysis, but it could easily interpreted as V^2, mV^2 or something similar. The convergence coefficient is always unitless.

[18] In the following the values of $E[x^2]$ are not explicitly mentioned anymore as it is not a useful indicator in this context, but is always at least one order of magnitude bigger than the largest α value.

[19] Of course, more iterations is always a possible way to "solve" this, but at some point the computational cost outweigh the potential benefit. Furthermore, a convergence is never guaranteed. It was observed more than once that a solution diverged even after million of iteration steps, which leads back to the importance of finding good coefficients in the first place.

the lower the included frequencies of the frequency range. This is most likely caused by the filter length, but this is not investigated further here, merely noted. If the upper end of the frequency range is increased again, this leads back to the results presented in Fig. 9.

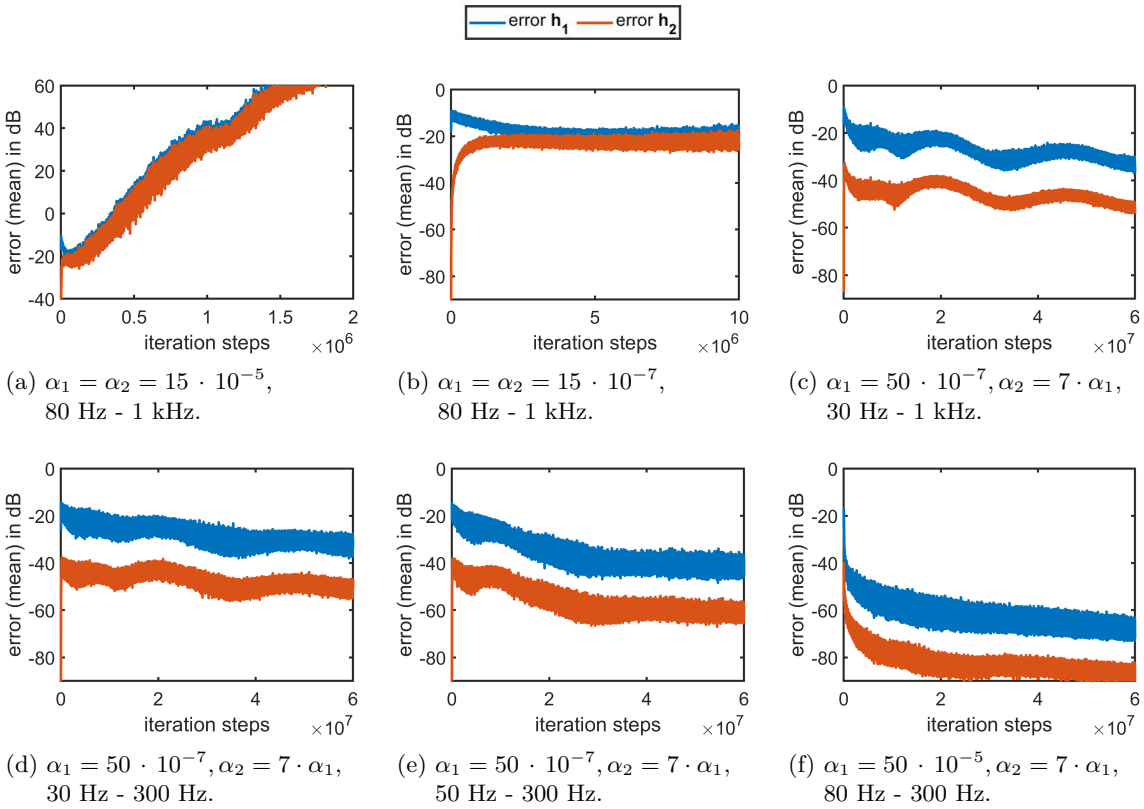

(a) $\alpha_1 = \alpha_2 = 15 \cdot 10^{-5}$, 80 Hz - 1 kHz.

(b) $\alpha_1 = \alpha_2 = 15 \cdot 10^{-7}$, 80 Hz - 1 kHz.

(c) $\alpha_1 = 50 \cdot 10^{-7}, \alpha_2 = 7 \cdot \alpha_1$, 30 Hz - 1 kHz.

(d) $\alpha_1 = 50 \cdot 10^{-7}, \alpha_2 = 7 \cdot \alpha_1$, 30 Hz - 300 Hz.

(e) $\alpha_1 = 50 \cdot 10^{-7}, \alpha_2 = 7 \cdot \alpha_1$, 50 Hz - 300 Hz.

(f) $\alpha_1 = 50 \cdot 10^{-5}, \alpha_2 = 7 \cdot \alpha_1$, 80 Hz - 300 Hz.

Figure 54: Various error graphs of the LMS method for the simulated duct, for different combinations of α and different frequency ranges. Corresponding frequency response estimation of the downstream path can be seen in Fig. 55. For better visualisation a moving average was applied to the data.

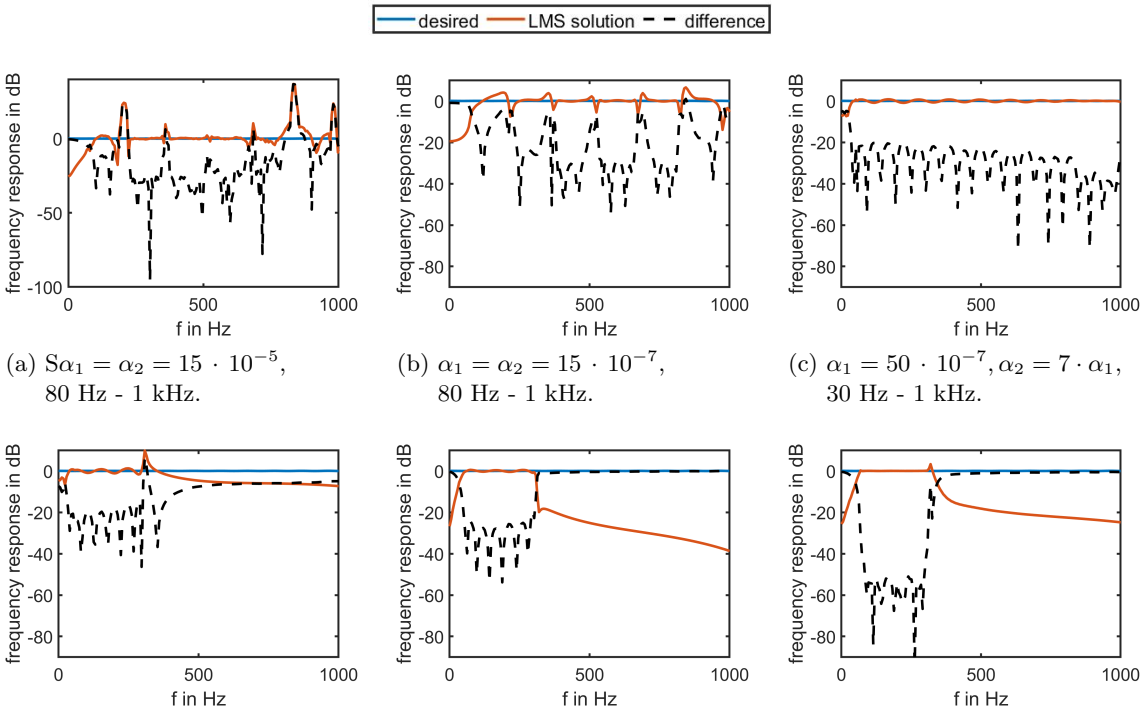

(a) S$\alpha_1 = \alpha_2 = 15 \cdot 10^{-5}$, 80 Hz - 1 kHz.

(b) $\alpha_1 = \alpha_2 = 15 \cdot 10^{-7}$, 80 Hz - 1 kHz.

(c) $\alpha_1 = 50 \cdot 10^{-7}, \alpha_2 = 7 \cdot \alpha_1$, 30 Hz - 1 kHz.

(d) $\alpha_1 = 50 \cdot 10^{-7}, \alpha_2 = 7 \cdot \alpha_1$, 30 Hz - 300 Hz.

(e) $\alpha_1 = 50 \cdot 10^{-7}, \alpha_2 = 7 \cdot \alpha_1$, 50 Hz - 300 Hz.

(f) $\alpha_1 = 50 \cdot 10^{-5}, \alpha_2 = 7 \cdot \alpha_1$, 80 Hz - 300 Hz.

Figure 55: Various frequency response estimations of the downstream path of the LMS method for the simulated duct, for different combinations of α and different frequency ranges. Corresponding error progressions can be seen in Fig. 54.

B. Additional Figures

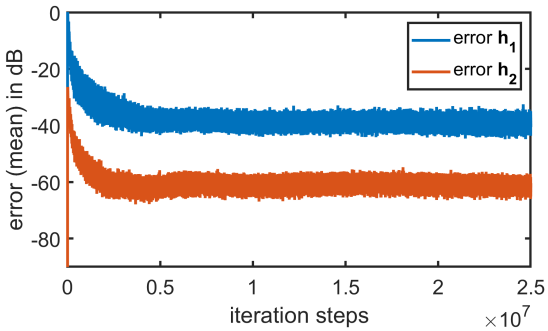

(a) Error progression over iteration steps, moving average applied.

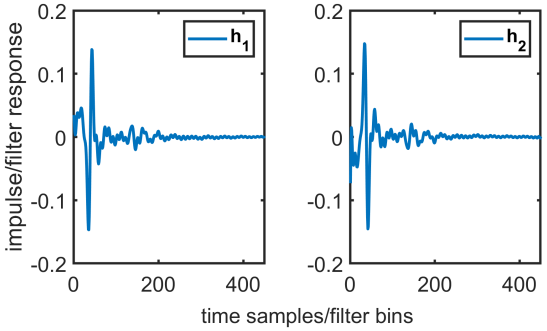

(b) Estimated FIR filters.

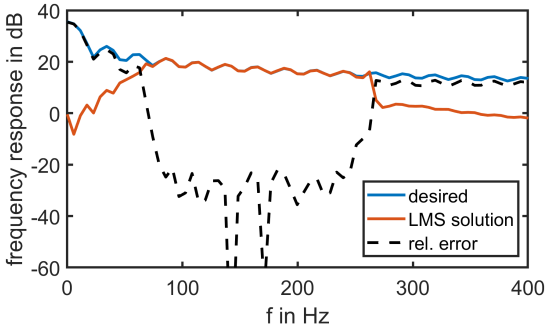

(c) Estimated frequency response of the downstream path and relative error.

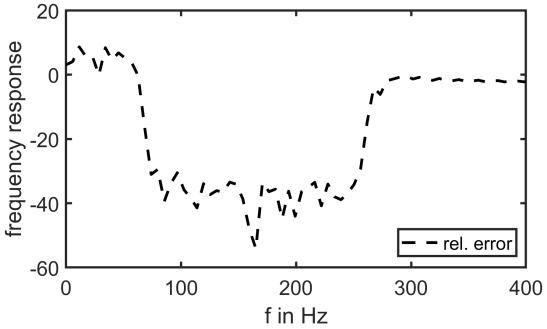

(d) Relative error of the estimated frequency response of the upstream path.

Figure 56: LMS results of the discrete line array with $n = 500$ sources and a distance $d_2 = 0.1$ m. $\alpha_1 = 5 \cdot 10^{-6}, \alpha_2 = 7 \cdot \alpha_1$, 80 Hz - 250 Hz after $2.5 \cdot 10^7$ iterations.

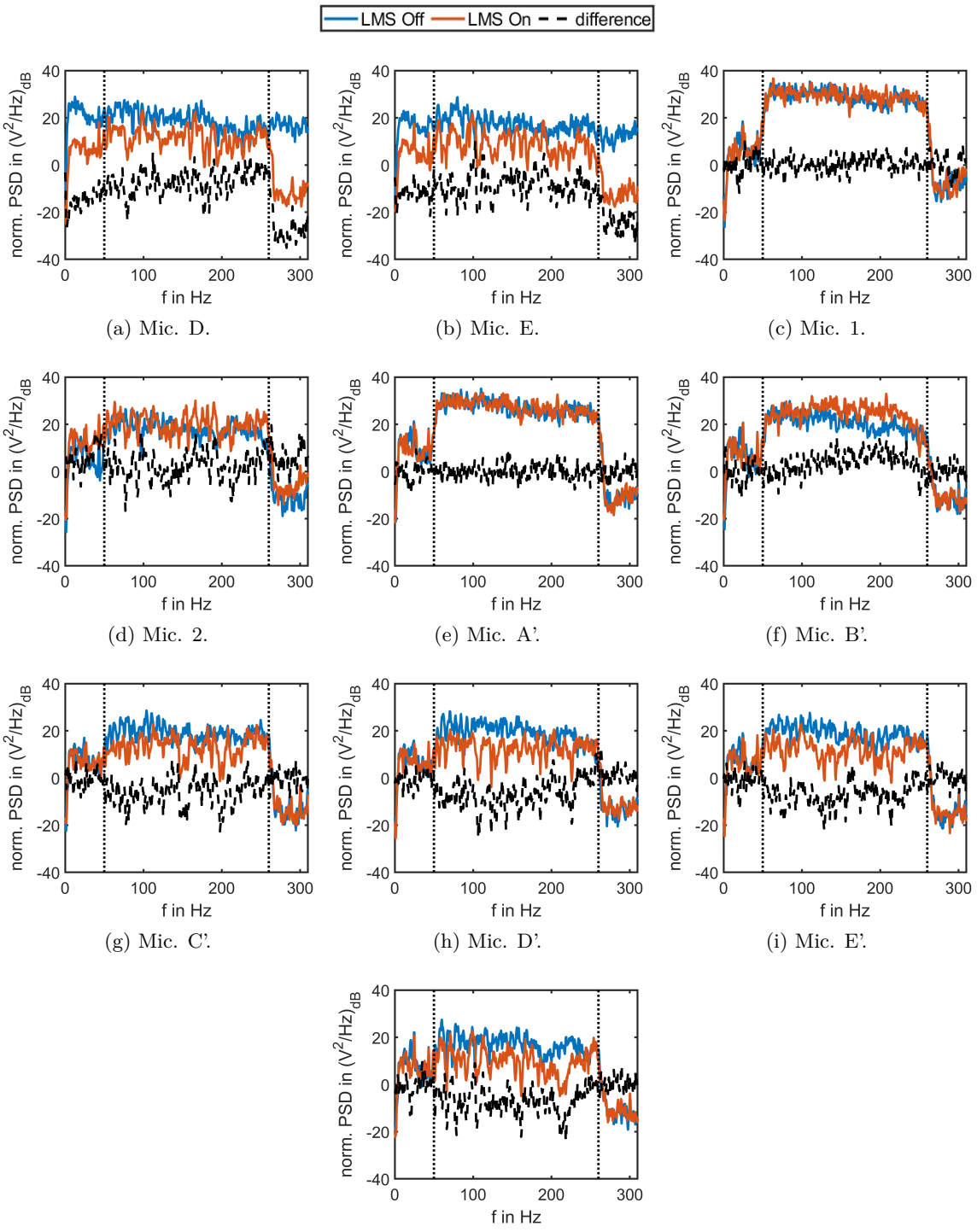

(a) Mic. D. (b) Mic. E. (c) Mic. 1.

(d) Mic. 2. (e) Mic. A'. (f) Mic. B'.

(g) Mic. C'. (h) Mic. D'. (i) Mic. E'.

(j) Mic. F'.

Figure 57: Additional normalised PSD graphs of measurement results of Setup1. All measurement results listed in Tab. 7.

C. Images

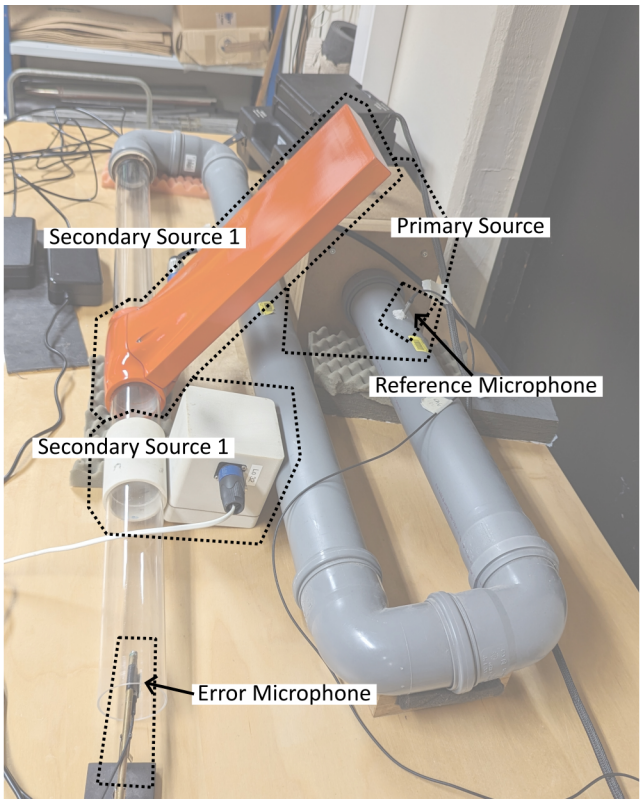

Figure 58: Side view of the duct setup.

Figure 59: Disturbed wildlife (own image capture).

Even though an attempt has been made to think of virtually everything to make the experiments run as smoothly as possible, one thing has definitely not been taken into account: that animals could possibly be disturbed in the side vegetation of Setup 1 (seen in Fig. 35a and Fig. 35b). Shortly after the first measurements began, a hedgehog (Fig. 59) was startled by the low frequencies. As hedgehogs are nocturnal, it had presumably gone into hiding to sleep. However, the hedgehog appeared to be in good condition despite the volume that had been present just a moment ago. The measurements were continued after the hedgehog had found a better place to sleep.

Bibliography

[1] Minarva J. Pandya Yogesh M. Gajera Hiral J. Jariwala, Huma S. Syed. Noise Pollution & Human Health: A Review. 2017.

[2] Andrew W. Smith. The World Health Organisation and the Prevention of Deafness and Hearing Impairment Caused by Noise. *Noise and Health*, 1(1), 1998. ISSN 1463-1741. URL https://journals.lww.com/nohe/fulltext/1998/01010/the_world_health_organisation_and_the_prevention.3.aspx.

[3] Paul Lueg. Verfahren zur Dämpfung von Schallschwingungen [Process of Silencing Sound Oscillations]. Patent 655508, DRP (German Petition), 1937.

[4] Paul Lueg. Process of Silencing Sound Oscillations. Patent 2043416, United States Patent Office, 1936.

[5] D. Guicking. On the invention of active noise control by Paul Lueg. *J. Acoust. Soc. Am.*, 87 (5):2251–2254, May 1990. URL https://doi.org/10.1121/1.399195.

[6] Kenneth Cunefare. Active noise control: Eight decades of research and applications. *J. Acoust. Soc. Am.*, 134(5):4188–4188, November 2013. ISSN 0001-4966. URL https://doi.org/10.1121/1.4831361.

[7] S.J. Elliott, I.M. Stothers, P.A. Nelson, A.M. McDonald, D.C. Quinn, and T. Saunders. The active control of engine noise inside cars. In *INTER-NOISE and NOISE-CON Congress and Conference Proceedings*. Institute of Noise Control Engineering, 1988.

[8] S. J. Elliot, P. A. Nelson, I. M. Stothers, and C. C. Boucher. In-flight experiments on the active control of propeller-induced cabin noise. *Journal of Sound and Vibration*, 140(2):219–238, 1990. ISSN 0022-460X. doi: 10.1016/0022-460X(90)90525-5. URL https://www.sciencedirect.com/science/article/pii/0022460X90905255.

[9] Nelson Philip A. Elliott Stephen J. Multiple-Point Equalization in a Room using Adaptive Digital Filters. *Journal of the Audio Engineering Society*, 37:899–907, november 1989.

[10] S.J. Elliott, C.C. Boucher, and P.A. Nelson. The behavior of a multiple channel active control system. *IEEE Transactions on Signal Processing*, 40(5):1041–1052, 1992. doi: 10.1109/78.134467.

[11] Kwon Nahyun, Park Moonseo, Lee Hyun-Soo, Ahn Joseph, and Shin Mingyu. Construction Noise Management Using Active Noise Control Techniques. *Journal of Construction Engineering and Management*, 142(7):04016014, July 2016. URL https://doi.org/10.1061/(ASCE)CO.1943-7862.0001121.

[12] P.A. Nelson and S.J. Elliott. *Active control of sound*. Academic Press, August 1991. ISBN 0-12-515425-9. URL https://eprints.soton.ac.uk/354428/.

[13] S.M. Kuo and D.R Morgan. Active Noise Control: A Tutorial Review. In *Proceedings of the IEEE*, volume 87, pages 943–973, 1999. doi: 10.1109/5.763310.

[14] Scott D. Snyder. *Active Noise Control Primer*. Modern Acoustics and Signal Processing. Springer New York, NY, 1 edition, 2000. ISBN 978-1-4612-6437-8. URL https://doi.org/10.1007/978-1-4419-8560-6.

[15] M.A. Swinbanks. The active control of sound propagation in long ducts. *Journal of Sound and Vibration*, 27(3):411–436, 1973. doi: https://doi.org/10.1016/S0022-460X(73)80355-4. URL https://www.sciencedirect.com/science/article/pii/S0022460X73803554.

[16] Marco Norambuena. *Active Control of Sound Absorption*. PhD thesis, 2012.

[17] R.A. Greiner Douglas E. Melton. Adaptive Feedforward Multiple-Input Multiple-Output Active Noise Control. In *in IEEE International Conference on Acoustics, Speech, and Signal Processing*, volume 2, pages 229–232, San Francisco, CA, USA, 1992. URL 10.1109/ICASSP.1992.226078.

[18] T. Lobato R. Sottek W. Kropp, K. Larsson. Application of the LMS algorithm to identify the surface velocity responsible for the radiated sound pressure. *Acta Acust.*, 5, 2021. URL https://doi.org/10.1051/aacus/2021023.

[19] Marcian E. Hoff Bernard Widrow. Adaptive switching circuits. In *IRE WESCON Convention Record*, pages 96–104, 1960.

[20] K. Larsson W. Kropp. Force estimation in the time domain by applying an LMS-algorithm. In *in NOVEM*, 2005.

[21] Wolfang Kropp Thomas Alber Michael Sturm, Andy Moorhouse. Robust Calculation of Simultaneous Multi-Channel Blocked Force Signatures from Measurements mane in-situ using an Adaptive Algorithm in Time Domain. *in Bangkok, Thailand*, 2013.

[22] N. Amiryarahmadi; W. Kropp; K.Larsson. Application of LMS Algorithm to MeasureLow-Frequency Transient Forces from HumanWalking. *Acta Acustica United with Acustica*, 102: 23–34, 2016. doi: 10.3813/AAA.918921.

[23] Charles A. Desoer Frank M. Callier. *Linear System Theory*. Springer Science + Business Media New York, 1991. doi: 10.1007/978-1-4612-0957-7.

[24] Ward Cheney and David R. Kincaid. *Linear Algebra: Theory and Applications*. Jones and Bartlett Publishers, Inc., USA, 2008. ISBN 0763750204.

[25] Kwai Sang Sin Goodwin Graham Clifford. *Adaptive Filtering: Prediction and Control*. Englewood Cliffs: Prentice-Hall, cop. 1984, 1984. ISBN 013004069X.

[26] David G. Messerschmitt Michael L. Honig. *Adaptive Filters: Structures, Algorithms, and Applications*. The Springer International Series in Engineering and Computer Science, Boston, 1984.

[27] Michael G. Larimore John R. Treichler, C. Richard Johnson. *Theory and design of adaptive filters*. John Wiley Sons, Inc., 1987. ISBN 0-471-83220-0. URL https://archive.org/details/theorydesignofad00trei.

[28] Augustine H. Markel, John D.; Gray. *Linear prediction of speech*. Springer Verlag Berlin, Heidelberg, 1976. ISBN 978-3-642-66288-1. doi: https://doi.org/10.1007/978-3-642-66286-7.

[29] M. Tygert P.G. Martinsson, V. Rokhlin. A Fast Algorithm for the Inversion of General Toeplitz Matrices. *Computers and Mathematics with Applications*, 50:741–752, September 2005. doi: doi:10.1016/j.camwa.2005.03.011.

[30] Simon S. Haykin. *Adaptive Filter Theory*. Englewood Cliffs, NJ : Prentice-Hall, 1986.

[31] Odile Macchi Eweda Eweda. Convergence of the RLS and LMS Adaptive Filters. volume 34, July 1987.

[32] Dirk T. M. Slock. On the Convergence Behaviour of the LMS and the Normalized LMS Algorithms. volume 41, September 1993.

[33] Micheal G. Larimore C. Richard Johnson Jr Bernard Widrow, John McCool. Stationary and Nonstationary Learning Characteristics of the LMS Adaptive Filter. In *Tacconi, G. (eds) Aspects of Signal Processing. NATO Advanced Study Institutes Series*, volume 33. Springer, Dordrecht, 1976. URL https://doi.org/10.1007/978-94-010-1223-2_23.

[34] G. Sessler R. Lerch, D. Wolf. *Technische Akustik, Grundlagen und Anwendungen [Technical Acoustics, Principles and Applications]*. Springer, 2009. ISBN 978-3-540-23430-2. doi: 10.1007/978-3-540-49833-9.